Report prepared by:
Christopher L. Alexander
Alberto A. Sagüés
Mahesh Karki
Laxmi Kandel

Development of a Nondestructive Imaging Tool to Identify Deficiencies in External Tendons Containing Flexible Fillers

Final Report (Project BED25-977-20)

Final Report to Florida Department of Transportation

Christopher L. Alexander (PI)

Adrian Steele (FDOT Project Manager)

UNIVERSITY OF SOUTH FLORIDA

Tampa, FL 33620

July 2026

Disclaimer page

The opinions, findings, and conclusions expressed in this publication are those of the authors and not necessarily those of the Florida Department of Transportation.

Universal conversion table

SI* (MODERN METRIC) CONVERSION FACTORS				
APPROXIMATE CONVERSIONS TO SI UNITS				
Symbol	**When You Know**	**Multiply By**	**To Find**	**Symbol**
		LENGTH		
in	inches	25.4	millimeters	mm
ft	feet	0.305	meters	m
yd	yards	0.914	meters	m
mi	miles	1.61	kilometers	km
		AREA		
in^2	square inches	645.2	square millimeters	mm^2
ft^2	square feet	0.093	square meters	m^2
yd^2	square yard	0.836	square meters	m^2
ac	acres	0.405	hectares	ha
mi^2	square miles	2.59	square kilometers	km^2
		VOLUME		
fl oz	fluid ounces	29.57	milliliters	mL
gal	gallons	3.785	liters	L
ft^3	cubic feet	0.028	cubic meters	m^3
yd^3	cubic yards	0.765	cubic meters	m^3
		NOTE: volumes greater than 1000 L shall be shown in m^3		
		MASS		
oz	ounces	28.35	grams	g
lb	pounds	0.454	kilograms	kg
T	short tons (2000 lb)	0.907	megagrams (or "metric ton")	Mg (or "t")
		TEMPERATURE (exact degrees)		
°F	Fahrenheit	5 (F-32)/9 or (F-32)/1.8	Celsius	°C
		ILLUMINATION		
fc	foot-candles	10.76	lux	lx
fl	foot-Lamberts	3.426	candela/m^2	cd/m^2
		FORCE and PRESSURE or STRESS		
lbf	poundforce	4.45	newtons	N
lbf/in^2	poundforce per square inch	6.89	kilopascals	kPa
APPROXIMATE CONVERSIONS FROM SI UNITS				
Symbol	**When You Know**	**Multiply By**	**To Find**	**Symbol**
		LENGTH		
mm	millimeters	0.039	inches	in
m	meters	3.28	feet	ft
m	meters	1.09	yards	yd
km	kilometers	0.621	miles	mi
		AREA		
mm^2	square millimeters	0.0016	square inches	in^2
m^2	square meters	10.764	square feet	ft^2
m^2	square meters	1.195	square yards	yd^2
ha	hectares	2.47	acres	ac
km^2	square kilometers	0.386	square miles	mi^2
		VOLUME		
mL	milliliters	0.034	fluid ounces	fl oz
L	liters	0.264	gallons	gal
m^3	cubic meters	35.314	cubic feet	ft^3
m^3	cubic meters	1.307	cubic yards	yd^3
		MASS		
g	grams	0.035	ounces	oz
kg	kilograms	2.202	pounds	lb
Mg (or "t")	megagrams (or "metric ton")	1.103	short tons (2000 lb)	T
		TEMPERATURE (exact degrees)		
°C	Celsius	1.8C+32	Fahrenheit	°F
		ILLUMINATION		
lx	lux	0.0929	foot-candles	fc
cd/m^2	candela/m^2	0.2919	foot-Lamberts	fl
		FORCE and PRESSURE or STRESS		
N	newtons	0.225	poundforce	lbf
kPa	kilopascals	0.145	poundforce per square inch	lbf/in^2

*SI is the symbol for the International System of Units. Appropriate rounding should be made to comply with Section 4 of ASTM E380.

Technical report documentation page

<table>
<tr><td>1. Report No.</td><td>2. Government Accession No.</td><td>3. Recipient's Catalog No.</td></tr>
<tr><td colspan="2" rowspan="2">4. Title and Subtitle
Development of a Non-destructive Imaging Tool to Identify Deficiencies in External Tendons Containing Flexible Fillers</td><td>5. Report Date</td></tr>
<tr><td>6. Performing Organization Code</td></tr>
<tr><td colspan="2">7. Author(s) Christopher L. Alexander, Alberto A. Sagüés, Mahesh Karki, Laxmi Kandel</td><td>8. Performing Organization Report No.</td></tr>
<tr><td colspan="2" rowspan="2">9. Performing Organization Name and Address
4202 E. Fowler Avenue, ENG 030
Department of Civil and Environmental Engineering
University of South Florida (USF)
Tampa, FL 33620</td><td>10. Work Unit No. (TRAIS)</td></tr>
<tr><td>11. Contract or Grant No.
BED25-977-20</td></tr>
<tr><td colspan="2" rowspan="2">12. Sponsoring Agency Name and Address
Florida Department of Transportation
605 Suwannee St. MS 30 Tallahassee, Florida 32399
(850)414-4615</td><td>13. Type of Report and Period Covered

Draft Final Report
03/15/2024-07/31/2026</td></tr>
<tr><td>14. Sponsoring Agency Code</td></tr>
<tr><td colspan="3">15. Supplementary Notes</td></tr>
</table>

16. Abstract
The University of South Florida’s Corrosion Research Laboratory previously developed a tendon imaging unit (TIU) capable of providing representative cross-section images of external tendons that show strand envelope position and the likelihood of grouting deficiencies. The objective of this work was to adapt the grout-based TIU for application to wax-filled external tendons. After characterization of the electrical properties of FDOT approved waxes, it became apparent that adaptation to wax-filled tendons would require sophisticated signal analysis to account for the limited difference between the dielectric constant for wax and air. An analysis approach was developed in which the magnetic signal is converted to a representative impedance signal considering a flaw-free, completely wax-filled condition. Comparison between the magnetic-signal recovered impedance and the measured impedance facilitates deficiency detection. Air void and water pocket deficiency detection with cross-section image recovery was demonstrated for a series of strand configurations and fill conditions. In a parallel thrust, an initial design for a rotation-free TIU was developed, and preliminary testing confirmed the capability of recovering strand position. This is a particularly promising advancement that with further development could result in increased ability to rapidly scan external tendons to facilitate bridge-scale testing or monitoring systems.

<table>
<tr><td colspan="2">17. Key Words: Image reconstruction, magnetic sensor, impedance, convolution</td><td colspan="2">18. Distribution Statement</td></tr>
<tr><td>19. Security Classif. (of this report)</td><td>20. Security Classif. (of this page)</td><td>21. No. of Pages
93</td><td>22. Price</td></tr>
</table>

Form DOT F 1700.7 (8-72) Reproduction of completed page authorized

Acknowledgements

The authors gratefully acknowledge Cesar Aranda, Ethan Zylman, and Hari Patel for their efforts in unit reconstruction and software development.

Executive summary

The research and development of a tendon imaging unit (TIU) applicable to wax-filled external post-tensioned tendons presented in this report demonstrates the feasibility of deficiency detection considering both voided regions of wax and water intrusion. The product of this research was a laboratory testing methodology for deficiency detection in wax-filled external post-tensioned tendons that incorporates an analysis procedure that predicts the impedance profile response of a deficiency-free tendon from the measured magnetic response. The software developed in this work was designed to instantly compare the measured impedance response to the magnetic-recovered response, to flag large deviations as possible deficiency locations. When the measured impedance response is significantly less than the magnetic-recovered response, a blue region is displayed in the cross-section image to suggest the presence of water within the tendon. If the measured response is substantially larger than the recovered impedance, a red color signals the potential presence of an air void. Due to the limited difference between the dielectric properties of wax and air compared to that of wax and water, the method is much more sensitive to the presence of water than air and thus, there is more confidence in the ability to detect water.

The development and adoption of the TIU to wax-filled tendons required an understanding of the electrical properties of the specific waxes approved by FDOT. An initial concern was that the electrical properties may vary between different wax manufacturers and be dependent on measurement frequency and temperature. Fortunately, detailed characterization of the electrical properties for each wax product revealed minimal dependence on temperature and frequency, considering typical measurement conditions, and very little variance between manufacturers. Therefore, the measurement analysis procedure could be formulated to only consider geometric parameters of the tendon and would not require wax manufacturer and measurement temperature inputs.

With the inherent reduced sensitivity to air void detection in wax-filled tendons, a new approach to recover the cross-section image from the measured magnetic and impedance signals was necessary. In the TIU developed for grout-filled tendons, due to the large difference between the impedance of grout and air, a simple impedance threshold approach could be invoked to signal the presence of an air void. This approach was not suitable for wax-filled tendons, and instead, the magnetic signal was used to recover a flaw-free impedance representation that could be directly compared to the measured impedance profile. The method used a Fourier transform that relies on a deconvolution kernel to relate the magnetic and impedance signals. The kernel was somewhat dependent on how the strands are distributed in the cross-section, but this work established that a geometry-averaged kernel could be reliably used for a given tendon arrangement. Thus, the geometric inputs required for kernel determination included duct outer diameter and wall thickness and the number and size of strands, but not the precise strand distribution. Further work is required to create a pre-calculated practical library of kernels for the range of tendon configurations used on Florida bridges.

One of the limitations to widespread utilization of the TIU for deficiency detection in external tendons is the requirement for manual rotation of the unit. As a parallel thrust, a next generation TIU prototype which eliminates the need for manual rotation was developed. The prototype incorporates an array of impedance plate sensors and potential-controlled magnetic coil sensors in which measurement between the sensors may be performed rapidly with multiplexing functionality to provide circumferential data that would otherwise require manual rotation. The rotation-free TIU prototype was shown to be able to recover the strand bundle envelope with both the magnetic and impedance data.

Table of contents

List of figures

List of tables

List of acronyms

AC	Alternating Current
ACI	American Concrete Institute
ANS	Arduino Nano-style
APL	Approved Product List
ASCE	American Society of Civil Engineers
CW	Conductive Water
DC	Direct Current
DI	Deionized
EMF	Electromotive Force
FAU	Florida Atlantic University
FDOT	Florida Department of Transportation
FEM	Finite Element Modelling
FT	Fourier Transform
IFT	Inverse Fourier Transform
LCR meter	Inductance-Capacitance-Resistance meter
MT	Mock Tendon
MTA	Mock Tendon A
MTB	Mock Tendon B
MTC	Mock Tendon C
MTD	Mock Tendon D
MV	Mock Void
PEEK	Polyether Ether Ketone
PT	Post-Tensioned
PVC	Polyvinyl Chloride
SRR	Split Ring Resonator
TIU	Tendon Imaging Unit
USF	University of South Florida
VDTD	Void Down TIU Down
VDTU	Void Down TIU Up
VT	Void Threshold
VUTD	Void Up TIU Down
VUTU	Void Up TIU Up
WT	Water Threshold

1 Introduction

1.1 Background statement

Modern bridges rely on encased steel strands (tendons) for fast and economical construction. Premature external tendon failures needing costly repairs and bridge closures have occurred because of deficiencies in tendon fill material intended to prevent corrosion. With over 400 segmental bridges in the U.S. and large bridges with upwards of 1,000 tendons, strong demand exists for fast, inexpensive, and nondestructive methods to diagnose external tendon fill quality for timely preventive action. Researchers at the USF Corrosion Engineering Laboratory created a promising electromagnetic low-cost tendon imaging unit (TIU) concept, which was granted U.S. patent 11,448,610 B2. The TIU produces in a few seconds a cross-section image in which grout fill voids can be identified with minimal need for expensive operator training. The initial work (FDOT BDV25-977-24) [2] established basic science, and created a prototype successfully tested in Florida bridges. The technology potential was further proven by tests comparing favorably with state-of-the-art much costlier (and slower) technologies, like gamma ray tomography. In its present form, the TIU reliably detects large grout voids and provides partial indication of other deficiencies like defective grout fill or water spaces. For enhanced detection sensitivity, it is important to expand the TIU capability to detect smaller voids and positively identify other types of fill deficiencies, including flexible wax-filled tendons, which are now adopted by Florida and other states instead of cementitious grout for which the TIU was originally aimed. Initial modeling efforts revealed that the sensitivity to smaller deficiencies in grout and detection of deficiencies in wax-filled tendons could be substantially enhanced using a broader frequency range of sensing signals.

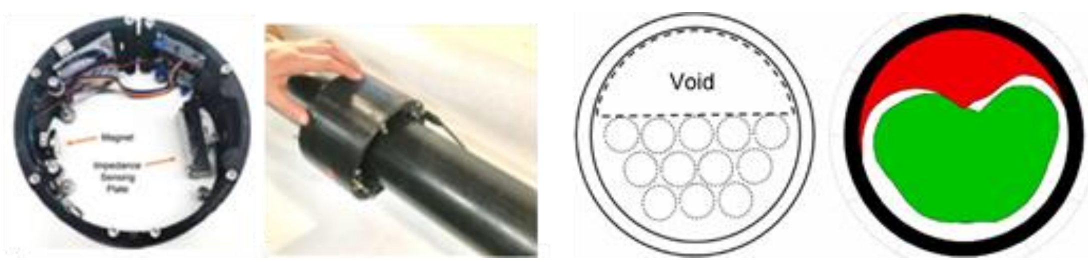

Figure 1-1. Tendon Imaging unit (TIU) developed at USF Corrosion Engineering Laboratory for grout-filled tendons and the image generated by TIU [1].

Current alternative tendon deficiency detection methods do not reliably identify the location of the fill deficiency within the cross-section of the tendon, unless using slow and expensive penetrating radiation (X-or gamma rays). Other technologies based on electrical signals are presently available, but with little or no imaging capability. A cost-benefit analysis relating projected rates of tendon failures and the implementation of the TIU (FDOT BDV25-977-24) estimated that as much as hundreds of millions of dollars could be saved just in Florida over the next half century by implementing regular tendon inspections. These estimates are included in Deliverable 6 of FDOT BDV25-977-24 and are based on a single inspection of all the external PT bridges in the FDOT inventory because the method discovers unchanging grout deficiencies that cause corrosion, not the corrosion itself.

1.2 Project objectives

The technical goal of this work was to modify the design of unit hardware and software for application to detect voids in wax-filled external post-tensioned tendons. The modification was informed through modeling and experimental efforts to identify optimal operating parameters (frequency range, amplitude, sensor type and size, etc.) that maximize the sensitivity of TIU for detection of fill deficiencies within wax-filled external tendons.

2 Literature review (Task 1)

Flexible fillers of which can include thixotropic gels, greases, waxes, and polymer-based products are expected to change shape according to minor movements of the tendons without cracking, unlike cementitious fillers. Flexible fillers were first specified by FDOT in the Structures Design Bulletin in April 2014 and subsequently in the January 2016 specifications [3]. Since then, updates to the structure design guidelines have included the requirement of multiple tendon paths for redundancy, minimum clearance required for replacing the tendons, and re-adoption of diabolo forms. There are now several projects completed and under construction using flexible filler, including the Wildwood I-75 Turnpike Interchange and the I-295 Expressway in Jacksonville [4].

However, the placement of flexible fillers in tendons can still result in defects. The presence of water in the ducts can result in emulsification of the filler, as noted in the ACI/ASCE 423.4R report [5]. Flexible fillers may also leak through cracks, anchors, or joints due to poor application quality, changes in filler composition, or instability at higher temperatures, causing void formation and allowing for water infiltration [6-9]. Laboratory and field experiments identified voids and cracks in wax-filled tendons due to entrapped air, thermal changes, and improper venting during the injection process [10, 11] [4]. Such defects can harbor moisture or contaminants, creating corrosion-inducing environments. FDOT specifications mandate the identification and filling of voids within 24-48 hours post-injection to mitigate risks [12-14].

The tendon imaging unit (TIU), designed and tested for void detection in grout-filled tendons may be suitable for the detection of moisture-laden zones and voids in wax-filled tendons as well. However, to interpret the measurements and ensure accurate identification of deficiencies in wax, the electrical properties must be known as a function of both signal frequency and material temperature. The objectives of this review are to identify the electrical properties (relative permittivity and conductivity) of waxes and to identify the optimal frequency range for maximum defect sensitivity. Additionally, the impact of impurities on the electrical properties of wax will be explored to examine whether impurities may be strategically introduced to enhance defect detection sensitivity, if necessary.

2.1 FDOT-approved waxes and placement procedures

Of the various types of flexible fillers, waxes are the most applicable to tendon construction and can come in both macrocrystalline (paraffin wax with relatively large crystals) and microcrystalline (smaller, compact and round grain crystals) forms. Paraffin is the macrocrystalline wax derived specifically from the refinement of low-boiling wax distillate fractions obtained from crude oil. It is primarily composed of straight-chain hydrocarbons (methylene [15]) or fatty-acid esters [16]. The molecular weight of paraffin wax generally ranges from 350 to 600 atomic mass units. The linear molecular structure results in crystallization in the form of large needles and plate-like crystals [17], or a network of large tubular crystals similar in shape to rice grains [18]. The crystallinity of paraffin wax gives a relatively low and distinct melting point range, typically between 46°C and 68°C (115°F and 154°F).

On the other hand, microcrystalline wax is derived from heavy petroleum distillates or residues comprising highly branched-chain paraffins, cyclo-paraffins, naphthene, and alkylated aromatics. These compositions tend to form solids with lower degree of crystallinity or structural order, and crystals more amorphous in nature remain small. Although they contain predominantly larger molecules than that of paraffin wax (300 to 2500 amu [19]), the crystals formed are more round and compact grains [18] smaller than macrocrystalline wax [20]. The structure of microcrystalline waxes results in a highly flexible material with a smooth texture that does not bleed or separate over time [21, 22].

There are several attractive properties of microcrystalline waxes for the application of a tendon fill material, including:

a) Oil Retention Capacity: Microcrystalline wax has a higher capacity to retain oil (the amount of oil that can be absorbed and retained within its structure/per unit weight or volume) compared to paraffin wax. This property makes it suitable for formulations requiring lubrication, moisture retention, or a soft, pliable consistency.
b) Flexibility: The highly branched-chain paraffins and cyclo-paraffins present in microcrystalline wax impart greater ability to bend, adapt and change without losing functionality compared to paraffin wax. This flexibility makes it ideal for applications where the wax needs to conform to different shapes or undergo repeated bending without cracking or breaking.
c) Adhesion: Microcrystalline wax exhibits excellent adhesion properties, allowing it to adhere well to various substrates, including paper, cardboard, plastics, and metals. This property makes it suitable for coatings, adhesives, and laminates in packaging, printing, and other industrial processes.
d) Resistance to moisture and chemicals: Microcrystalline wax is typically more hydrophobic and resistant to chemicals compared to some other types of waxes. This property makes it suitable for applications where protection against environmental factors or chemical exposure is essential, such as in coatings, sealants, and corrosion protection.

For these reasons, microcrystalline wax is the preferred flexible filler for post-tensioned tendons. The FDOT-approved microcrystalline waxes are shown in Table 2-1. The basic physical and thermal properties of the waxes as well of the strands and duct used as tendon system components are given in Table 2-2.

Table 2-1. FDOT approved flexible filler used for post-tensioned structures

SN	Name of the product	Supplier	APL Number	Specification	Product type
1	CIRINJECT CP	CIVETEA	938-003-001	Duct filler for post-tensioned structures	Flexible filler - microcrystalline wax
2	Fill-Flex 100	The Trenton Corporation	938-003-002	Duct filler for post-tensioned structures	Flexible filler - microcrystalline wax
3	Fill-Flex 200	The Trenton Corporation	938-003-003	Duct filler for post-tensioned structures	Flexible filler - microcrystalline wax
4	Renolin CL 4 RO	Fuchs Lubricants Co.	938-003-004	Duct filler for post-tensioned structures	Flexible filler - microcrystalline wax

Table 2-2. Physical and thermal properties of flexible fillers (properties for RENOLIN CL 4 RO extracted from product information provided by FUCHS), duct, and strands adapted from [23, 24]

Properties	Flexible filler			Duct	Strands
	Trenton	CIRINJECT CP	RENOLIN CL 4 RO		
Physical properties					
Density (kg/m^3)	-	880	-	970	8050
Specific gravity @60°F (15°C)	0.83-0.9	-	0.934 (7.8 lbs/gal)	-	-
Drop melting point °F (°C)	100(37.7)-120(48.8)	149(65)-167(75)	180	-	-
Congealing point °F (°C)	-	-	155-165	-	-
Flash point °F (°C)	>400(205)	>392(200)	425	-	-
Viscosity @210°F (98°C), mm^2/s	-	17-22	16.2-19.4 (75-90 SUS)	-	-
Thermal properties					
Thermal conductivity (W/m/°C)	0.25	0.25	0.25	0.5	52
Specific heat capacity (J/Kg/°C)	2700	2700	2700	2250	420

The standard procedure for the placement of the wax is specified in Section 462 of the FDOT Standard Specifications Manual [13]. According to the manual, a wax injection operation plan should be prepared beforehand in cooperation with the PT system vendor and the PT wax manufacturer and approved by the Engineer for the injection process. Mockup tests should be conducted and approved before the actual injection process.

The wax placement procedure in the field involves several critical steps. Any excess water present in the polymer duct shall be drained completely prior to wax injection. To do so, oil-free compressed air is blown inside the duct to remove any entrapped moisture. Effective removal of water and moisture is confirmed by humidity measurements taken at the inlets and outlets after 15 minutes of air blowing, with values below 40%. The waxes are usually delivered in 55-gallon barrels. The wax-filled barrels are heated to a temperature between 212°F-240°F and the liquefied wax is injected into the duct using vacuum assisted pumps. Upon completion of injection, inlets, outlets, drains, and ports are sealed using threaded plastic plugs and epoxy compounds. The plugs physically block openings, while epoxy compounds fill recesses to prevent leakage.

2.2 Electric properties of wax

Waxes are dielectric materials, also called insulators. These materials possess an electric dipole established or reoriented either temporarily or permanently in response to an applied electric field. This results in an increase in the capacitance between electrodes immersed in or having intervening space filled with the material, with respect to conditions where a vacuum exists instead of the material. The electric properties of dielectric substances like wax are usually described in terms of the dielectric constant and conductivity, which can vary with the measurement frequency and temperature. In this section, the results of a literature review are presented, synthesizing the available data on the electrical properties of waxes according to their dependence on measurement frequency and material temperature. Also included is a background section that describes the electrical properties of interest and physical indicators of frequency and temperature dependence.

2.2.1 Background

Figure 2-1 shows a parallel plate capacitor where two plates of area A are separated by a dielectric material of permittivity ε* with a depth d. In a parallel plate capacitor with a DC voltage source, more charge is stored when a dielectric material is present between the plates compared to when there is a vacuum. The added charge storage of a capacitor is directly related to the dielectric constant.

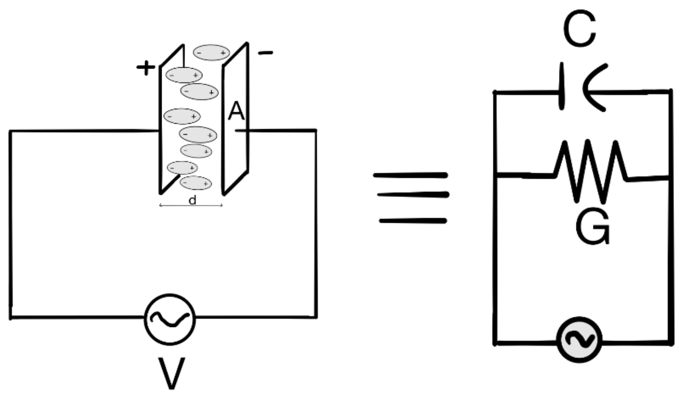

Figure 2-1. Parallel plate capacitor connected with an AC source and the equivalent circuit.

When an AC voltage source (V) is applied to the capacitor, the resulting current (I) comprises two components: the charging current (I_c) and the loss current (I_L). The loss current is a complex quantity related to the complex character of the dielectric constant. The losses can be represented by a parallel combination of resistors having conductance (G) with a capacitor (C)

$$I = I_c + I_L = V \times (j\omega C_o \varepsilon' + \omega C_o \varepsilon'') = V \times j\omega C_o \times (\varepsilon^*) \qquad \text{Equation 2-1}$$

where, $G = \omega C_o \varepsilon''$; C_o= Capacitance without dielectric medium(A/d); $\omega = 2\pi f$ (frequency of applied field).

There are different dielectric mechanisms at work within the material when an electric field is applied, which contribute to the capacitance. These mechanisms describe how materials respond to electric fields by displacing their internal electric charge carriers. Dipolar polarization and ionic conduction mechanisms described in the subsequent section are dominant in microwave frequency region. The common dielectric mechanisms at microscopic level are described as follows [25, 26]:

Orientation (dipolar) polarization: Dipoles are molecules with positive and negative charges distributed in opposite direction. When there is an imbalance in electron distribution within the molecules, permanent dipole moments are formed. These dipoles are randomly oriented within the medium. If an electric field is applied, the dipoles rotate to align with the applied field. Typically, occurring in the microwave range of frequency, this alignment process involves friction within the molecules, causing dielectric losses.

Ionic conduction: If free ions are present in the material, they respond to the applied electric field as well. In the presence of the electric field at frequencies typical of the microwave range, the motion of free ions within the material contributes to conductivity of the material. There is collision and friction during the movement of these ions within the material, causing energy dissipation and loss. This loss is ionic conductivity loss. This loss is more significant at low frequencies.

Electronic and atomic polarization: Electronic and Atomic polarization occur at higher frequencies than microwave frequency for semi-solid materials like wax. When an electric field displaces the nucleus of a neutral atom relative to its surrounding electrons, electronic polarization occurs, whereas atomic polarization takes place when an electric field stretches neighboring positive and negative ions.

The dielectric property of a material is defined by the relative permittivity. In an alternating electric field, the complex relative permittivity (ε^*) has a real (ε') and imaginary part (ε''). Mathematically, the complex permittivity of material relative to that of free space is expressed as:

$$\varepsilon^* = \varepsilon' - j\varepsilon'' \qquad \text{Equation 2-2}$$

ε' is the dielectric constant, which measures the ability of the dielectric medium to store electrical energy, while ε'' is called the dielectric loss factor and is a measure of how dissipative or lossy a material is to an external electric field, and $j = \sqrt{-1}$. Similarly, another important parameter is the tangent of loss angle given by:

$$\tan(\delta) = \frac{\varepsilon''}{\varepsilon'} = \frac{\text{Imaginary part of Dielectric Constant}}{\text{Real part of Dielectric Constant}} \qquad \text{Equation 2-3}$$

Both the real and imaginary parts are independently reported in the literature. For a pure liquid, dielectric properties are explained by the Debye model using the following equations:

$$\varepsilon' = \varepsilon_\infty + \frac{\varepsilon_s - \varepsilon_\infty}{1 + \omega^2\tau^2} \qquad \text{Equation 2-4}$$

$$\varepsilon'' = \frac{(\varepsilon_s - \varepsilon_\infty)\omega_*\tau}{1 + \omega^2\tau^2} \qquad \text{Equation 2-5}$$

Here, ε_s is the static permittivity at zero frequency, ε_∞ is the permittivity at infinite frequency, ω is the angular frequency of the applied electric field, and τ is the characteristic relaxation time in seconds. Relaxation time (τ) indicates how easily molecules in a material can orient under an applied electric field. It is the time required for molecules, after displaced of their normal state by an electric field, to get back to about 37% of their random equilibrium state. In liquids and solids, molecules cannot move freely because of constant collisions, causing friction. This makes them slowly align with the electric field over time, described by the relaxation time (τ). When the electric field is disconnected, the molecules go back to their random positions within the same amount of time.

The Equation 2-3 and Equation 2-4 above show explicit dependency of dielectric constant on frequency (ω), and dependency on temperature is shown implicitly by τ (Equation 2-5). For a spherical molecule, the Debye-related relaxation time is expressed as:

$$\tau = \frac{3\nu}{kT}V \qquad \text{Equation 2-6}$$

Here, ν is the viscosity, T is the absolute temperature, k is the Boltzmann constant, and V is the volume of the molecule.

In the following sections, the results of a literature review of measured electric properties of waxes considering frequency ranging from kHz to GHz and temperature varying from 0˚C to ~100˚C is presented. The dependence of the dielectric properties on temperature is important because the placement of the wax requires that it be heated above its melting temperature. If measurements are to be made immediately or shortly after placement of the wax, it will be important to account for temperature dependence in the analysis.

2.2.2 Frequency dependence of electrical properties

The dielectric loss mechanisms relating to their chemical composition and structure were more established for liquid dielectrics than solid dielectrics up to the early 1930s. To establish such a mechanism of dielectric loss in solid dielectrics and in an attempt to find a material which is devoid of dielectric loss and could hold known impurities, a highly refined paraffin wax became an ideal choice of material. Since then, there have been studies of paraffin's dielectric properties. Jackson [27], Sillars and Phil [28], and Pelmore [29] were the pioneers who worked on the electrical properties of paraffin wax. Jackson [27] plots a graph showing a change in capacitance with temperature for three different samples of paraffin wax and only provides a value at a frequency of 10 MHz, the residual (base or minimum capacitance, which is almost constant value for all samples at lower temperatures) capacitance is 26.50 pF, which corresponds to a dielectric constant of 2.18. However, these papers do not explicitly give the values of dielectric constant and conductivity.

Callinan and Parks [30, 31], Hassan et al. [32, 33], and Prava [34] have studied the electrical properties of different types of wax in Hz-MHz frequency range. Callinan and Parks [31] studied the dielectric constant of coal-based montan wax (a brown-black solid obtained from California lignite, with a specific gravity of 1.02 at 25°C, melting at 77°C, composed of 53% wax acid esters including hydroxy acids), and plant-based carnauba and ouricuri waxes at different temperatures. They found that the dielectric constant of montan wax at 24°C decreases from 2.90 at 0.1 kHz to 2.79 at 0.1 MHz. Hassan et al. [32] prepared a basic grease from a mixture of ~30% by weight microcrystalline wax, ~46% base lube oil, ~23% transformer oil, and other constituents and calculated dielectric constant from 1 kHz to 1MHz and temperature of 35^{o}C.

A direct comparison between the dielectric values of microcrystalline wax by different researchers could not be established. Notably, the dielectric constant value of paraffin wax at 10 kHz reported by Callinan and Parks [30] is 2.50 at 20°C, whereas Prava [34] reports a value of 5.575 at room temperature. This suggests that the paraffin waxes used might have different compositions. A summary of all the data found in the literature is shown in Figure 2-2. There is a wide range of values reported for the dielectric constant from 2 to 7, but the results indicated limited dependence on the measurement frequency. Alternatively, the dielectric loss data seem to converge to similar values at higher measurement frequencies approaching 1 MHz.

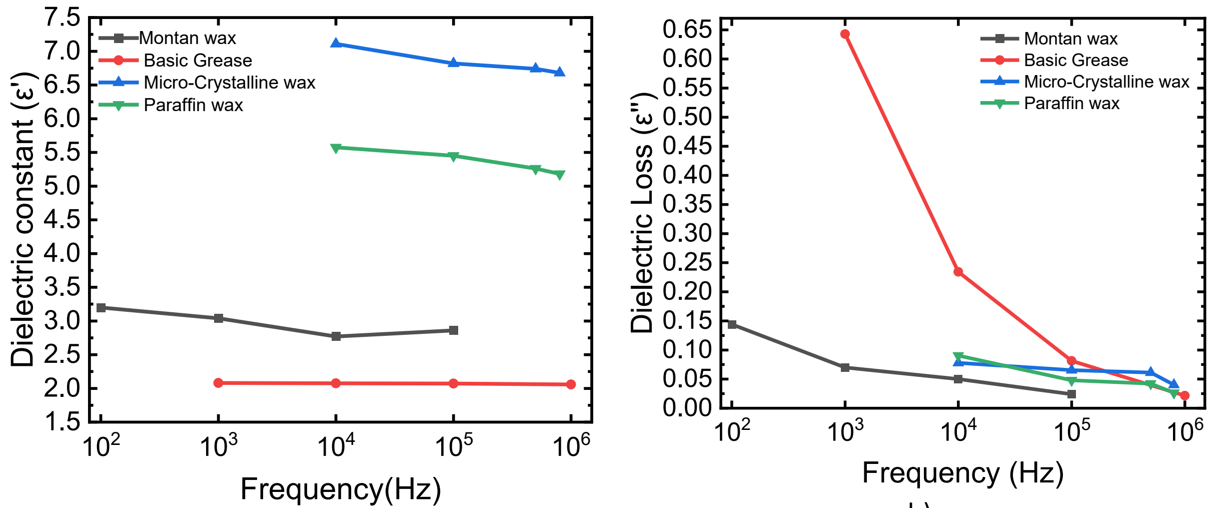

a) b)

Figure 2-2. Dielectric properties of montan wax [31], basic grease [32], and paraffin and microcrystalline wax [34]: (a) Dielectric constant (ε' real part) variation of waxes with frequency; (b) Dielectric loss (ε'' imaginary part variation of various waxes with frequency.

Although conductivity is another indispensable parameter to describe the electrical properties of wax, there is insufficient data available in the Hz-MHz range. Only Hassan et al. measured the volume resistivity of the basic grease. Since grease and wax exhibit similar electrical properties, and one of the constituents was microcrystalline wax, the presented values in Figure 2-3 provides an idea of the expected order of conductivity in the given frequency range for microcrystalline wax.

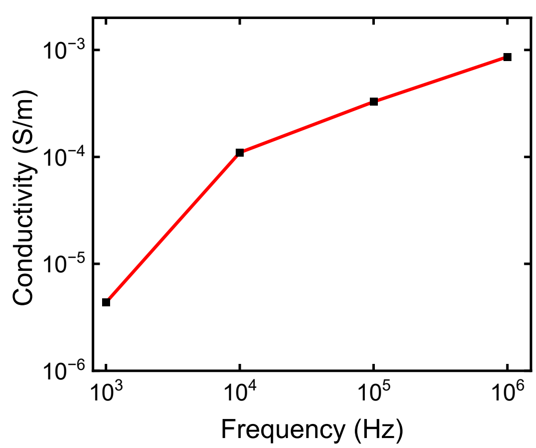

Figure 2-3. Conductivity of basic grease as a function of frequency at temperature of 35°C (both in log scale) [32].

As previous work has shown, the sensitivity of the TIU may be improved by increasing the measurement frequency beyond 1 MHz. Therefore the electrical properties of the waxes at frequencies greater than 1 MHz are important. Unfortunately, only frequencies within the GHz range were found in the literature.

Chakyar et al. [35] and Prava [34] have studied the values of dielectric constant of different waxes in GHz region of frequency, the values of which are shown in Figure 2-4. Particularly, as frequency increases, there is a consistent decrease in dielectric constant, while the behavior of dielectric loss varied.

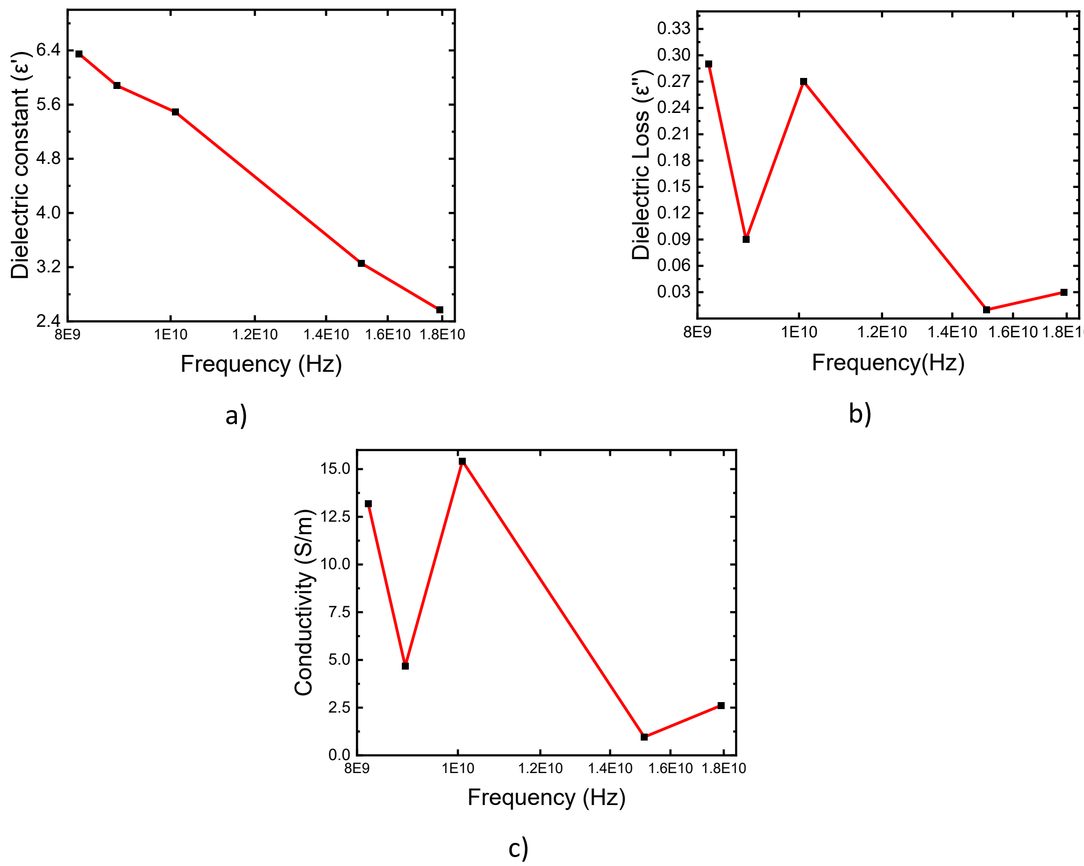

Figure 2-4. Dielectric properties of microcrystalline wax in GHz range [34]: (a) Dielectric constant as a function of frequency (log scale) of microcrystalline wax; (b) Dielectric loss as a function of frequency in log scale of microcrystalline wax; (c) Conductivity of microcrystalline wax as a function of frequency in log scale.

Table 2-3. Summary of electrical properties of microcrystalline wax

Frequency	Relative permittivity (ε)	Conductivity(σ) (S/m)	Remarks
0 (DC)	-	8.03×10^{-11}	Prava
10 kHz	7.34	0.00011	σ from Hassan et al.
100 kHz	7.15	0.000328	σ from Hassan et al.
800 kHz (1 MHz)	6.94	0.000862	σ from Hassan et al. of 1 MHz
8.2 GHz	6.35	15.039	σ is same from Prava
10.1 GHz	5.49	2.625	σ is same from Prava
15.1 GHz	3.26	1.25	σ is same from Prava
17.9 GHz	2.57	5.1	σ is same from Prava

Table 2-3 shows a summary of the available dielectric constant and conductivity obtained from the literature review in the frequency range of 10 kHz to 1 GHz. The electrical properties of microcrystalline wax are scarce in literature. But the term ''grease'' for the flexible filler material has been constantly used in the earlier PT tendon system. The grease referred to in this review is also a mixture of microcrystalline wax and other constituents (constituents have been addressed above) (Hasan et al. [32]). A trend of the decrease in the dielectric constant with frequency (7.34 at 10 kHz and 2.57 at 17.9 kHz), and an increase in the conductivity (in the range of 10^{-13} at 0 Hz to 5.1 at 17.9 GHz) has been observed. A direct comparison on dielectric constant values as a function of frequency from different sources could only be established for the paraffin wax. The contrast in values shows that a different composition of waxes had been used. This leads to doubt in the use of the available dielectric values for further study.

2.2.3 Temperature dependence of electrical properties

The PT system undergoes temperature variation as the wax is injected into the tendon ducts, ranging from as high as 240˚F to eventually decaying to thermal equilibrium with the ambient temperature. The proposed imaging unit will be used to detect deficiencies after the injection process. Thus, one of the theoretical possibilities is to generate a cross-section image during the filling of the duct. This objective leads to the motivation of determining the decay of the temperature of the PT system (most importantly, the flexible filler) with the elapse of time. Rice et al. [23] have developed a basic thermal analysis model that accounts for the temperature changes in the system from injection to the complete filling of the duct. The model provides the temperature variation of the system for around 6 minutes from the time of injection and focuses on the temperature difference of wax at the inlet and different points along the length till the outlet.

Waxes can be roughly categorized into crystalline, amorphous or something in between. In amorphous materials, the dielectric constant increases slowly with temperature due to decreased viscosity and easier molecular orientation, but decreases when fully liquid because of lower polarizable molecule density and increased thermal motion [30]. However, crystalline material shows a sudden increase in dielectric constant at the melting point.

Microcrystalline wax is also the intermediate between crystalline and amorphous with more inclination towards amorphous. The literature shows the variation of dielectric properties of different waxes such as, carnauba, ouricuri, montan, paraffin, bees wax and bran wax. Callinan and Parks categorize the carnauba, ouricuri, and montan wax as intermediate class, which is crystalline but also has amorphous structures. Their study shows a high dependence of dielectric constant on temperature. While studying the temperature range of -60˚C to +95˚C, a typical pattern of relatively constant value at lower temperatures, increase in value with temperature up to melting point and decrease in value beyond melting point is observed. Chakyar et al. [35] studied the dependence of dielectric constant of bees wax, bran wax and paraffin wax in the temperature range of 30˚C to 60˚C. Increasing the temperature of the wax medium resulted in changes in resonant frequency. This change in resonant frequency is due to the change in dielectric properties of wax medium on heating. They concluded that the dielectric constant varies linearly with an increase in temperature. Figure 2-5 shows the dependence of dielectric constant of different waxes on temperature.

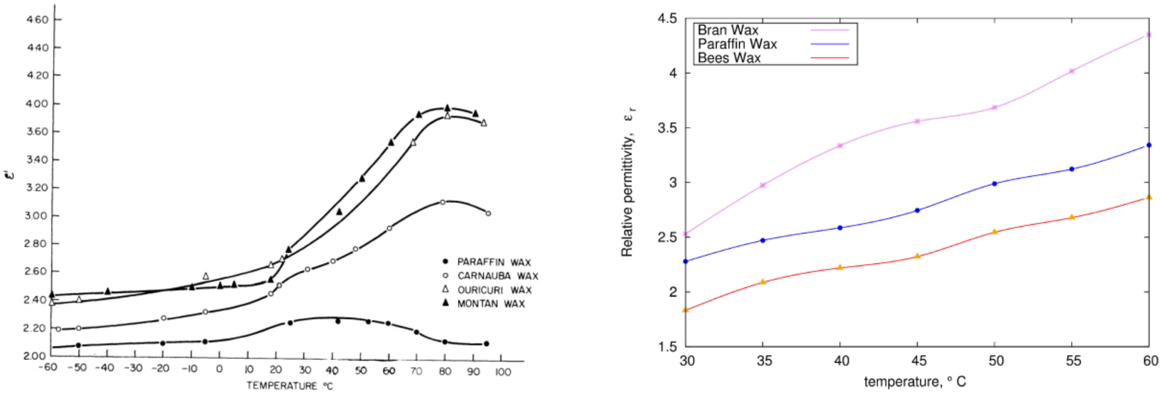

a) b)

Figure 2-5. (a) Variation of dielectric constant of waxes with temperature at 10 kHz adopted from Callinan and Parks [30, 31]; (b) Dielectric constant variation of different wax samples with temperature at respective resonant frequency (the resonant frequency of SRR depends on capacitance and inductance, the introduction of dielectric medium changes the capacitance resulting in changes in resonant frequency. Moreover, the changes in temperature of the wax medium also result in changing dielectric value and thus the resonant frequency) adopted from Chakyar et al. [35].

The review underscores the changes in dielectric properties of waxes with temperature. However, there is limited data on the dielectric properties for microcrystalline wax specifically. Thus, an assessment of the electrical properties of the approved microcrystalline wax with frequency range of interest and as a function of temperature is necessary.

2.2.4 Effects of impurities on electrical properties

If the sensitivity of the TIU to deficiencies within wax is not sufficient, it has been proposed that impurities may be added to modify the electrical properties of the wax for enhanced defect detection sensitivity. To examine which types of impurities could be added to increase the sensitivity of defect detection, a review on the influence of impurities on dielectric properties was conducted.

Initial experiments to understand the mechanism of dielectric properties variation of waxes with frequency and temperature by adding impurities goes back to the key studies of Jackson [27], Sillars and Phil [28], and Pelmore [29]. Jackson [27] observed the variations of dielectric loss in paraffin wax solutions where refined paraffin wax was considered as a base case (assumed non-polar and free of ions) and polar ester, cetyl palmitate, as an impurity by varying temperature and frequency. The author attempted to control the structural constituent of the sample to attribute the mechanism of dielectric loss in solid dielectrics. While trying to understand the effect of concentration of cetyl palmitate (0-12.85% by weight), the author observed that maximum dielectric loss at a given temperature became less predictable or less influential as concentration increased. Moreover, on studying the changes in dielectric constant with concentration of cetyl palmitate, it was observed that there was an insignificant amount of increase in dielectric constant with concentration. Subsequent works of Sillars and Phil [28] on the behavior of solid samples of paraffin wax with small concentrations (around 5%) of various long-chain esters, polar molecules, like Ethyl stearate, Butyl palmitate, Butyl stearate, Octyl palmitate, Dodecyl palmitate, Dodecyl stearate and cetyl palmitate confirmed that the observed losses are due to dipole moment provided by impurities. Also, the time constant for dielectric relaxation showed a non-linear relationship with total ester chain length.

Subsequently, in contrast to Sillars' work, where the length of esters was varied keeping the length of wax fixed, Pelmore [29] worked on examining how the relaxation time is impacted by modifying the chain length of the wax in which a given ester is dissolved, and concluded that the relaxation time depends mainly on the carbon chain lengths of the shorter component and that variations in the chain length of the wax component significantly impact the system's dielectric properties.

Hassan et al. [32, 33] in their two experiments prepared a basic lubricating grease and added different polymers to improve its physicochemical and dielectric properties, such as dielectric constant, dielectric loss, and volume resistivity, to make it a better electrical insulator by studying the dielectric properties using the computerized LRC (Hioki model 3531 Z Hi Tester) over the frequency range of 1 to 1000 kHz at 35^0C. Their experiments concluded that the greases containing atactic polypropylene and polyethylene due to their high-volume resistivity and non-polarity showed reduced dielectric properties. Grease produced from plasticized PVC showed lower dielectric properties when compared to grease made from unplasticized PVC.

Brito-Pereira et al. developed a composite polymer by combining paraffin wax, dielectric constant of 9.18, with different wt% proportion of high dielectric constant ceramic nano-filler (barium titanate), dielectric constant of 150, to get an enhanced polymer having dielectric value of 18 at 50 wt% of nanofiller barium titanate. Typically, with high filler concentrations often exceeding 50%, research indicates that paraffin wax can be enhanced with various fillers, such as barium titanate (BT), carbon microspheres, graphene, and carbon nanotubes, to significantly improve its dielectric properties. The dielectric constant of pure paraffin wax, which is around 2, can be increased to approximately 6.5 when combined with carbon microspheres [36], around 17 with graphene [37], about 18 with carbon nanotubes [38], 18 with BT coated with $BaFe_{12}O_{19}$ [39], and up to 35 with BT coated with polyaniline [40].

The works of Jackson confer that there is an insignificant increase(ΔC=0.32pf-0.79pf) in the dielectric constant and dielectric loss with addition of cetyl palmitate, a polar ester. In contrast to these, the experiments conducted by Hassan et al. concluded that the addition of impurities like atactic polypropylene and polyethylene, and grease produced from plasticized PVC led to inferior dielectric properties than the base grease. The work from other researchers showed that the dielectric value can be increased using different high dielectric constant ceramic nano fillers.

Thus, based on these works, it can be inferred that the dielectric properties of waxes can be altered by adding impurities containing dipoles or free ions. However, the greater dielectric value will make it easier to detect the voids, but it would be detrimental if the target is to detect the moisture and water-laden zones. The dielectric value of water is higher (~80 at room temperature) compared to the filler materials. The higher relative contrast in the dielectric values between the targeted defect and the sound filler material is ideal for detection. Also, the use of ionic compounds may pose a threat to the fundamental idea behind the use of flexible fillers. Thus, the interaction and effects of the additives to the steel strands and desired filler properties should be studied first before taking any further steps.

2.3 Summary

The literature review indicates that electrical properties of wax depend on both temperature and frequency. A research gap in electrical properties of microcrystalline wax in frequency range (between the MHz and GHz) of our interest is present. The dielectric constant shows a decreasing trend with increases in frequency, whereas the conductivity increases. Moreover, the values available for microcrystalline wax are at room temperature. Since the flexible filler-filled PT system undergoes a temperature variation ranging from as high as 240°F to ambient temperature, a thorough study of the electrical properties of the specific microcrystalline waxes approved by FDOT is necessary.

The dielectric values show a linear relationship with an increase in temperature up to the melting point, followed by a decrease after the melting point [30, 35]. Thus, the dependence of the electrical properties of microcrystalline wax with varying temperatures within frequency range of interest needs to be determined to be able to generate a representative cross-section image of the tendons immediately or shortly after placement of the wax. Additionally, the electrical properties of wax are subject to change with its composition and source, as it became evident from the variability in reported dielectric constant of Paraffin wax at the same frequency in the literature. Microcrystalline waxes used in FDOT projects are most likely to have a range of chemical compositions. Therefore, the electrical properties while varying both temperature and frequency need to be individually determined.

The review confirmed that potential defects like voids, leakages, and water-laden zones exist in wax-filled tendons, risking corrosion of steel strands. These defects will be incorporated into the modeling for TIU design using COMSOL Multiphysics Software. From the available results, comprehensive modeling and analysis will be performed to find the optimal frequency range where the TIU will have increased sensitivity to the possible defects. Moreover, the available physical and thermal properties of microcrystalline wax will be used to develop a thermal model, and if possible, will be validated against the experimental model.

Similarly, the potential advantage of using impurities in the filler materials to enhance the sensitivity of the TIU remained inconclusive from the review. The microcrystalline wax reviewed behaves more like an ideal dielectric medium, having insignificant dielectric loss values. The use of polar or ionic impurities to increase dielectric values may pose detrimental effects on the steel strands. Thus, the interaction and effects of the additives to the steel strands and desired filler properties should be studied in more detail before taking any further steps.

3 Unit design optimization (Task 1 continued)

The findings from the literature review could not provide well-defined values of the electrical properties of microcrystalline wax in the frequency range of interest (MHz range) with varying temperature from 100°C to around 0°C. Also, the composition of microcrystalline wax is not unique. The values of electrical properties differ with sources or if any additives are added to the composition of wax. Thus, an experimental setup explained in the following section was established to measure the electrical properties of different microcrystalline waxes approved by FDOT. Several sets of experiments have been conducted for each wax to establish the degree of reproducibility of results.

3.1 Measurement of wax electrical properties

The instruments used to characterize the electrical properties of materials are Network analyzers, Impedance Analyzers and LCR meters. The basic components of a network analyzer are signal source, receiver, and display. It provides detailed information on relative permittivity by measuring the magnitude and phase of reflected and transmitted signals in frequency range of 300 kHz to 325 GHz. While Impedance analyzers and LCR meters, on the other hand, are used for lower frequency measurements. They apply an AC source to the material and monitor the voltage response. By knowing the material's dimensions and measuring capacitance and dissipation factor, these devices determine key electrical properties.

3.1.1 Experimental setup

One common technique to measure dielectric properties includes the open-ended coaxial probe method [25, 26]. The coaxial probe method is a versatile technique for measuring material properties for liquids, semi-solids, and solids. It is efficient in high temperature measurement up to 1200°C. The measurement system typically consists of a network or impedance analyzer, a coaxial probe, and software. In this method, the probe is immersed in the liquid or semi-solid material. The electromagnetic waves are passed through the probe and allowed to penetrate the material. The waves undergo changes as they interact with the material. By measuring the reflected signal, the probe can determine the material's complex permittivity (ε*). This method assumes the material is semi-infinite, non-magnetic, isotropic, homogeneous, and free of air gaps.

A method similar to an open-ended co-axial probe, where the probe (inner part of a cell) immersed in the heated microcrystalline wax, was developed to measure the electrical properties of the investigated waxes. The instrument used was the HP 4192A LF impedance analyzer, which measures the electrical properties in frequency range of 5 Hz-13 MHz. An AC source to the material was applied using the probe and the responses were monitored. The capacitance was measured for four different frequencies. The dielectric constant of the material was measured using the following equation:

$$\varepsilon = \frac{C_m}{C_o} \quad \text{Equation 3-1}$$

where, ε= Dielectric constant of the used material; C_m= capacitance of the cell with the dielectric material; C_o=capacitance of the empty Cell (without dielectric material).

The conductivity of the material was calculated using the following equation:

$$\sigma = \frac{1}{\rho} = \frac{1}{R * C_L} \quad \text{Equation 3-2}$$

where, σ= Conductivity of the dielectric material; ρ = Resistivity of the dielectric material; C_L=Area/Length, characteristics length of the cell.

A system of components, shown in Figure 3-1, was used as the coaxial cell. Included is an outer 250-cc stainless steel beaker with a stainless-steel ground-connection screw on its rim and an inner cylindrical aluminum component of 1.5 inches diameter. The inner vessel is placed symmetrically within the outer portion. The positive terminal from impedance analyzer was connected to the inner vessel, and the negative terminal was connected to the outer part. The inner part is supported with a Teflon screw connected to the levelling disk. The PEEK screw electrically disconnects the inner and outer cell components. The levelling disk has three stainless steel fasteners embedded on the sides and the other three connecting (levelling) screws going normally through it. The screws on the side limit the movement sideways. These screws also help to center the inner vessel in the middle of outer vessel. The other three are the levelling screws going normally through the disk and resting on the bottom of the outer beaker. This connection makes the levelling disk the same terminal as the outer part. A temperature probe is inserted between the inner cylinder and outer beaker to record the temperature of cooling wax with elapse of time. The molten and heated microcrystalline wax is poured into the space between the inner part and outer beaker up to the lower rim of the mark in outer cylindrical beaker. The volume of this fill is around 200 cc with +\- 2 cc precision.

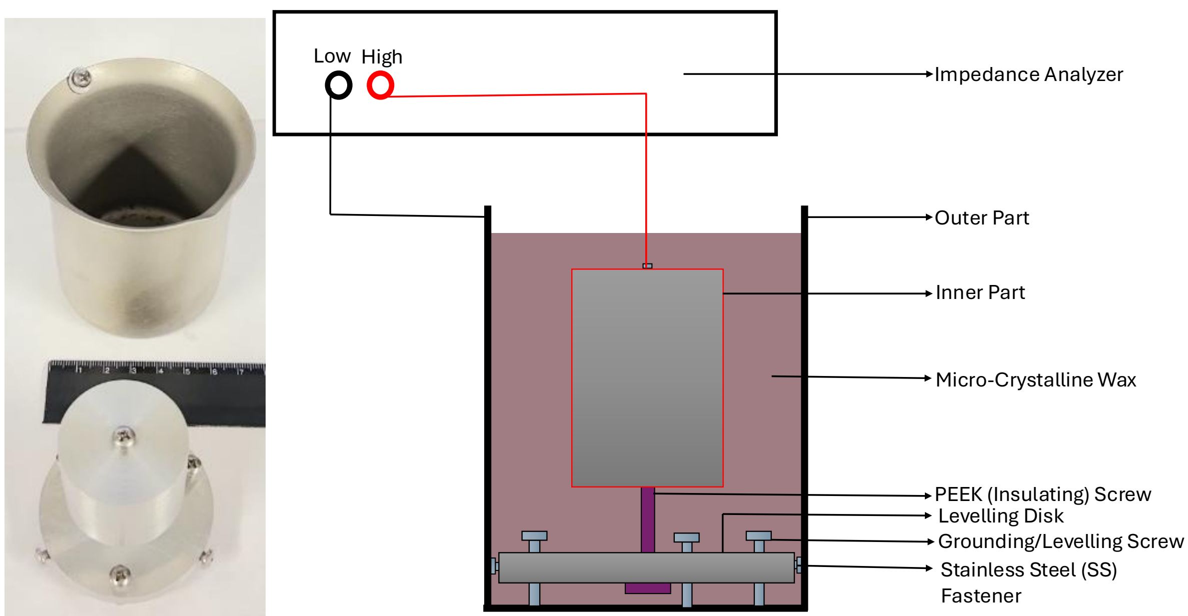

Figure 3-1. Image showing the components of cell apparatus: outer and inner vessels with levelling disk and screws. Figure showing the schematic drawing for experimental setup to measure electrical properties of microcrystalline wax.

In this experimental procedure, samples of each filler, approximately two gallons each, were procured. Each sample was thoroughly stirred to ensure uniformity. Subsequently, a portion of each sample was scooped and preheated in a 250 mL cylindrical beaker and transferred to the CELL apparatus. The CELL apparatus filled with microcrystalline wax was heated to a temperature of around 100°C using a water bath arrangement. Measurements of capacitance, impedance, and phase angles were taken at frequencies of 100 kHz, 1 MHz, 5 MHz, and 10 MHz and temperatures of 5°C intervals until the thermometer readings were within 1°C of the ambient temperature.

3.1.2 Modelling for determination of cell constant

A 2D- axisymmetric model geometry, as shown in the Figure 3-2, was developed in COMSOL Multiphysics® 6.0. The material properties of Domain 1 were specified based on the properties of the microcrystalline wax. Domain 2 represents the PEEK plastic screw of dielectric value 3. Domain 3 represents the air surrounding the measurement apparatus. The electrostatics interface within the AC/DC module was selected as the physics interface. The governing equations of this interface are used to calculate the capacitance of the cell provided the dielectric constant and conductivity of each material domain. A 1 V potential was assigned to the inner component surface boundary (red boundary), and a ground potential was assigned to the inner surface of the outer component (blue boundary). As shown, the model geometry was discretized according to a free triangular mesh with the smallest element size assigned to the wax and PEEK domains. The capacitance of the cell and the characteristic length were calculated by performing a parametric sweep of dielectric values of domain 1 (wax), ranging from 1 to 10.

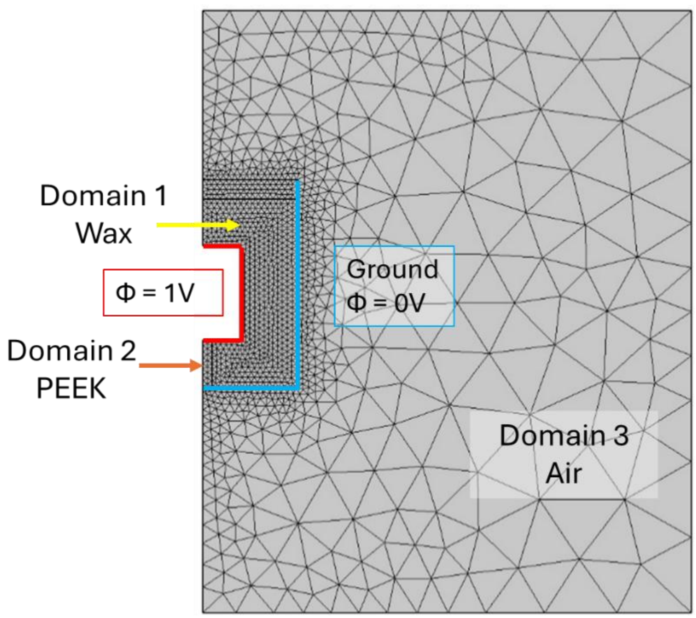

Figure 3-2. Finite element model geometry reflective of the experimental apparatus.

The model was used to relate the simulated values of cell capacitance to the dielectric constant of the material, as shown in Figure 3-3 (a). Notice that the relationship is reasonably linear, as expected. The corresponding characteristic length is shown as a function of dielectric constant in Figure 3-3 (b) and only varies slightly with the dielectric constant. Based on the simulation results, the characteristic length of the cell was estimated to be 60.7 cm.

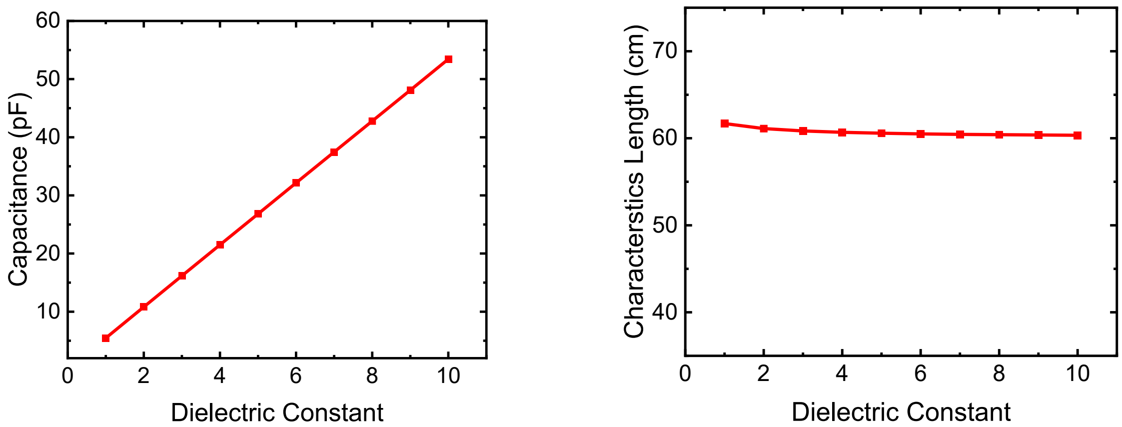

(a) (b)

Figure 3-3. Simulated values of (a) capacitance and (b) characteristic length, both as a function of dielectric constant.

3.1.3 Experimental results

The measured dielectric constant of each wax is expressed as a function of temperature with measurement frequency as a parameter in Figure 3-4. Each microcrystalline wax shows a unique curve with variation in temperature, having the maximum value around the melting point. Notably, all three waxes evaluated showed ε values quite close to 2, with only minor temperature and test temperature dependence in the tested ranges of interest. The result is encouraging in that it simplifies the requirements for development of a TIU, since calibration procedures for environmental changes may not involve large adjustments, and there would be wide latitude for the choice of a convenient operating frequency.

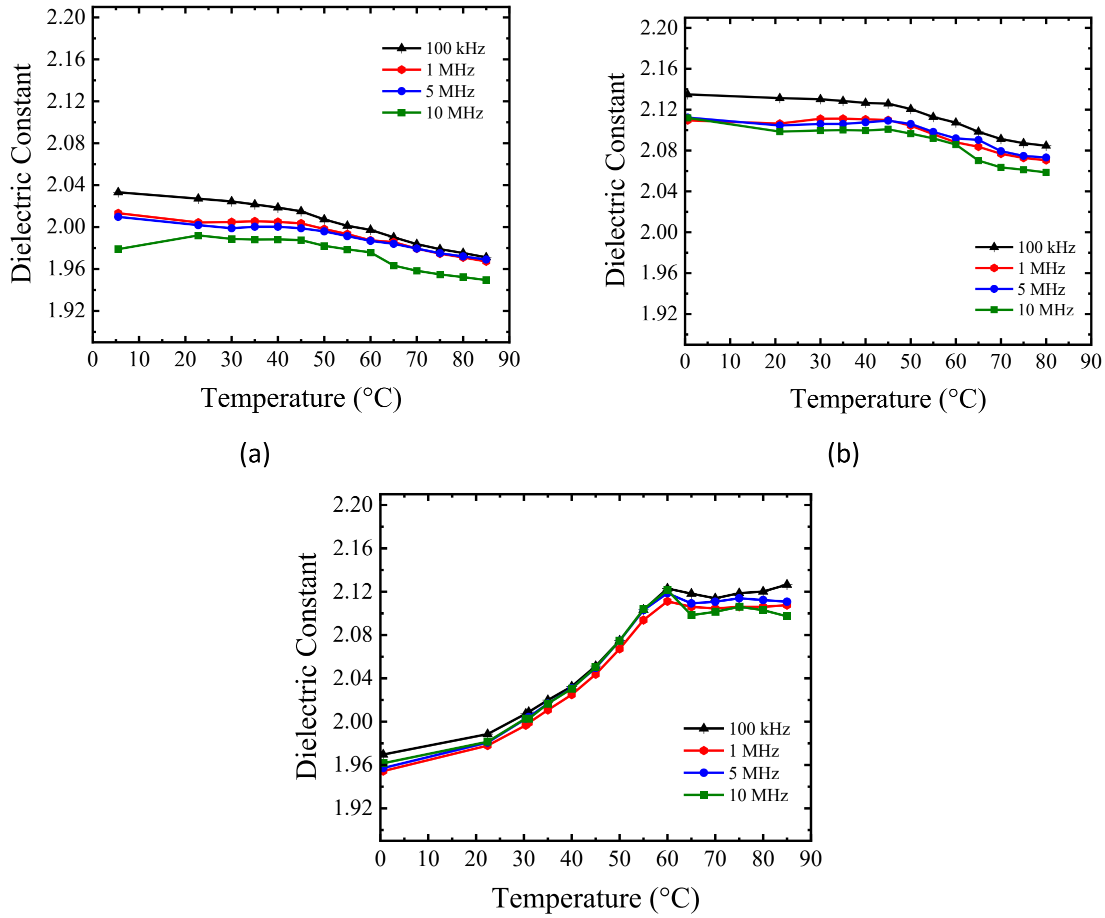

(c)

Figure 3-4. Dielectric properties of different flexible fillers at different frequencies as a function of temperature: (a) Dielectric properties of Fill Flex 100; (b) Dielectric properties of Cirinject CP; (c) Dielectric properties of Renolin CL 4 RO.

The measured impedance approached that of ideally capacitive behavior, with only a small (in the order of 1%) series real component. Expressing that component as a parallel conductance and using the cell characteristic length constant, an equivalent conductivity was calculated. The results are shown in Figure 3-5. The conductivity is expressed in log-scale and as shown, there is little dependence on the temperature at which the measurement is performed. At the lower frequencies, the conductivity increased approximately linearly with frequency, consistent with a frequency-independent loss factor. There was some deviation at the highest frequencies. The implications of this deviation to the sensitivity in defect detection of the TIU, if found to be relevant, will be assessed in further modeling work.

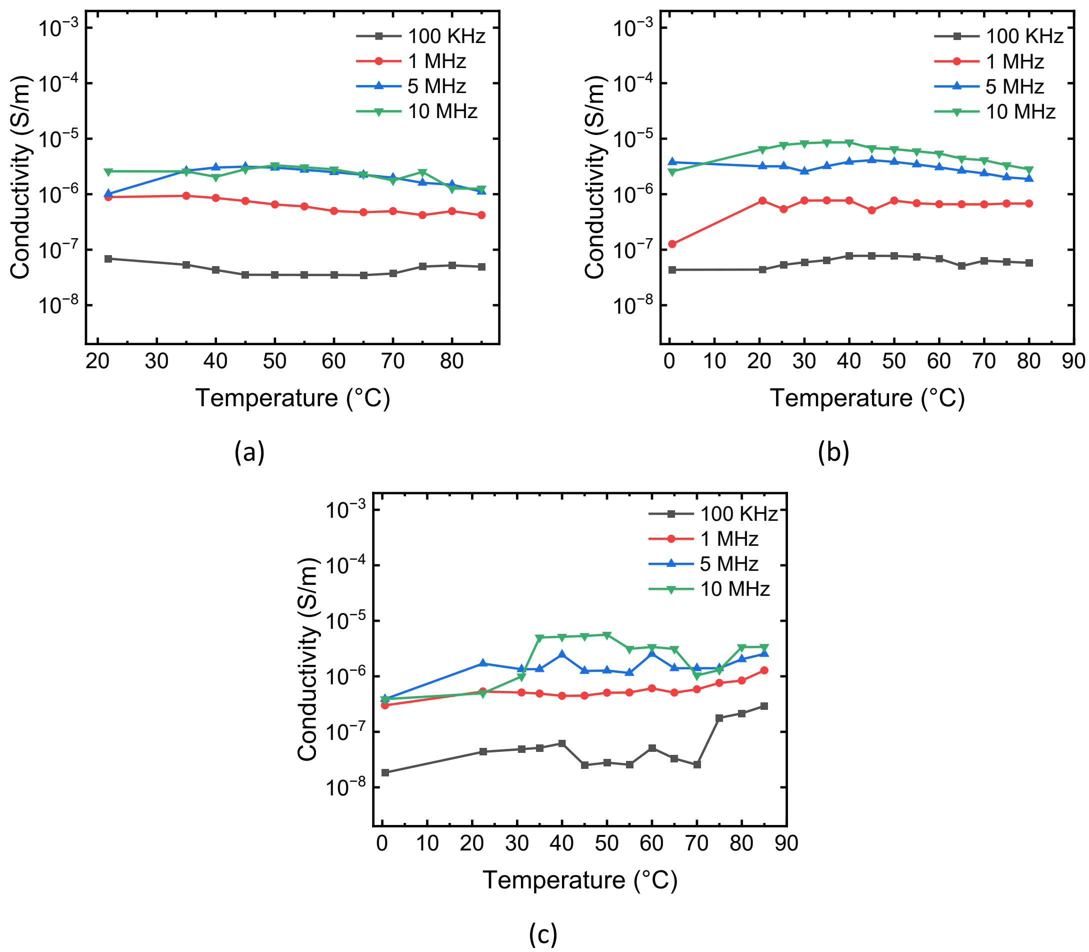

Figure 3-5. Conductivity of different flexible fillers at different frequencies as a function of temperature: (a) Conductivity of Fill Flex 100 ; (b) Conductivity of Cirinject CP (Log scale) versus temperature in degree Celsius; (c) Conductivity of Renolin CL 4 RO (Log scale) versus temperature in degree Celsius.

3.2 Impedance simulations

With knowledge of the strand positions within the tendon duct, high frequency (e.g., 1 MHz) impedance measurements between the strands and a sensing plate placed on the outer duct surface are expected to serve as an indication of tendon fill deficiencies. Figure 3-6 shows a schematic description of the impedance measurement and its individual contributions.

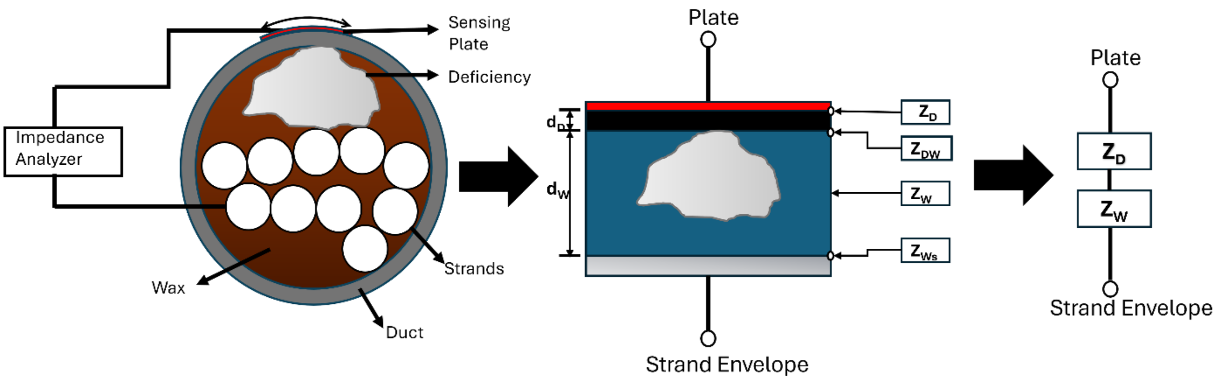

Figure 3-6. Impedance measurement configuration for wax-filled external tendons adapted from [41].

In the existing format of the TIU, an angular impedance profile is obtained by rotating the sensing plate hugging the outer surface of the polymer duct. The impedance, Z, measured between the sensing plate and the strands is dependent on the angle of rotation due to the varying characteristics of wax fill (thickness of wax and defects) between the plate and strands. The overall impedance is the combined effect of impedances of polymer duct (Z_D), duct-wax interface (Z_{DW}), the wax fill space between the inner surface of duct and the strands bundles (Z_W) and wax-strand interface (Z_{WS}).

Electrically interconnected bundles of steel strands at the anchor points are assumed to be continuous and act as a single conductor having boundary of strand bundle envelope. Considering only simple 1-D current flow scheme and ignoring the curvature and unevenness of sensing plate, tendon cross-section and surface of bundles of steel strands, the complex arrangement can be simplified as a parallel plate capacitor with layered dielectric fill (Figure 15 Center). Since the system is operated under high frequency, the relative impedances of interfaces are insignificant [42] compared to other terms. Thus, only the duct and wax impedances are taken into full account, leading to further simplification of the system (Fig 15 right):

$$Z = Z_D + Z_w \qquad \text{Equation 3-3}$$

Moreover, the composition and thickness of the HDPE duct are normally constant at each angle of rotation. Now, the impedance component Z_D in the above equation can be considered constant throughout and discounted from the equation. Thus, only the impedance of wax Z_w fill acts as the controlling factor. The Z_w depends upon the local wax space thickness dw and characteristics of wax composite condition. Since the Electromagnetic system gives us the local position of the strand envelope at each point of measurement, the thickness of the wax is no longer an unknown and can be compensated accordingly in the equation. Hence, the impedance value is a measure of the wax-fill condition. Thus, the impedance value increases or decreases with the presence of defects, deficiencies, or substituents within the wax fills.

The impedance of the overall system is the function of expected impedance behavior of Z_D and Z_W. The HDPE duct material is a known dielectric insulator with dielectric value (ε) estimated to be ~2.2 [43], pending confirmatory measurements to be performed during the next reporting period. The duct is assumed to act as a purely capacitive system. The approximation of Z_D as capacitive behavior is:

$$Z_D = 1/(j \times \omega \times C_D) \qquad \text{Equation 3-4}$$

where, $j = \sqrt{-1}$, $\omega = 2 \times \pi \times f$, f=frequency of the alternating field, $C_D = (\varepsilon_o \times \varepsilon \times A)/d$, capacitance of HDPE duct of thickness d, covering area A same as that of sensing plate in farads, Z_D is the impedance in ohms (Ω).

The wax composite thickness may include air voids or voids filled with water as defects. In this case, the medium can have a generalized dielectric constant (ε_W) and electrical conductivity (σ_W) for impedance calculations. The system will act as purely capacitive if the void is filled with air, and a combination of conductor and capacitor when filled with water. This key difference will be used to establish sensitivity of the device to the type of defect. The impedance behavior of wax Z_W at a given frequency can be expressed as a parallel combination of a conductor with a resistance value of R_W and a capacitor with capacitance value of C_W (unlike capacitance of the polymer duct, the thickness taken will be that of wax, d_W). Mathematically, impedance Z_w:

$$Z_w = \left[R_w + \frac{1}{j \times \omega \times C_w} \right] \qquad \text{Equation 3-5}$$

In the earlier version of TIU with cement grout as fill, grout has relatively higher dielectric value compared to wax fill. Thus, this difference in properties may impact sensitivity of the device to deficiencies in the wax fill material. Therefore, an impedance model described in the subsequent sections will be used to calculate impedances in different wax composite conditions to identify the optimal frequency that will maximize deficiency detection.

3.2.1 Model description

A finite element model was developed in COMSOL Multiphysics® V 6.0 to simulate impedance measurements on a finite cylindrical tendon segment between a plate hugging the external surface of the tendon and the steel strand bundle. For simulations, the strand bundle was modeled as a simple axially placed conductive cylinder. The length of the segment was much greater than the length or width of the plate. To approximate stray electric field coupling around the tendon segment, a finite cylindrical air domain was used, which was about twice as wide and long as the tendon segment. The dimensions for the different cases are listed in Table 3-1. The modeled domains included the surrounding air, the polymer duct, the sound flexible filler, and deficiencies, each with specific electrical properties. The plate and the strand bundle were considered ideal conductors and were represented according to the boundary conditions assigned to their interfaces with the other domains. The frequency dependency study simulations were performed using the 3D, AC/DC Electric Currents Module in COMSOL Multiphysics, focusing on capacitive and conductive effects while ignoring inductive effects for simplicity.

Each domain was assigned electric properties of conductivity (σ) and relative permittivity (ε_r). These properties were frequency-dependent in the flexible filler domain but constant in the other domains. An alternating potential difference was applied between the sensing plate and the strand assembly, resulting in a local alternating potential value (V) at each point in the domains under steady-state conditions. The corresponding local alternating electric field and displacement vectors were defined as:

$$\mathrm{E} = -\nabla \mathrm{V} \quad \text{Equation 3-6}$$

$$\mathrm{D} = \varepsilon_0 \varepsilon_r \mathrm{E} \quad \text{Equation 3-7}$$

where ε_0 is the permittivity of free space (8.854 × 10^{-14} F/cm) and ε_r is the relative permittivity of the medium. The total current density vector [44] is defined as:

$$i_T = \sigma \mathrm{E} + \frac{d\mathrm{D}}{dt} \quad \text{Equation 3-8}$$

According to Maxwell's equations, in the absence of finite charge density in the polymer, air, water, and flexible filler domains, the following condition holds:

$$\nabla . i_T = 0 \quad \text{Equation 3-9}$$

This equation was implemented in phasor terms, leading to the expressions:

$$i_T = \mathrm{Re}\left(\tilde{I}_T e^{j\omega t}\right) \quad \text{Equation 3-10}$$

and

$$\mathrm{V} = \mathrm{Re}\left(\tilde{\mathrm{V}} e^{j\omega t}\right) \quad \text{Equation 3-11}$$

This resulted in the time-independent expression [45-47], where i_T and V depend only on frequency and spatial position.

$$\nabla \cdot i_t = -(\sigma + j\omega \varepsilon_0 \varepsilon_r) \nabla^2 \tilde{\mathrm{V}} = 0 \quad \text{Equation 3-12}$$

The boundary conditions included fixed AC potential values at the metallic surfaces, with 0V (ground condition) at the strand bundle envelope side and end surfaces, an applied electric potential $\tilde{\mathrm{V}} = 1\ \mathrm{V}$ at the plate surface, and zero normal current density at the external air space surface. In the usual Alternating Current treatment, the impedance, Z, is defined as the complex ratio of change in potential ΔV to alternating Current I. Mathematically,

$$\mathrm{Z} = \frac{\tilde{\mathrm{V}}}{\tilde{\mathrm{I}}} \quad \text{Equation 3-13}$$

$V = V_o \times e^{j\omega t+\theta 1}$ and $I = I_o \times e^{j\omega t+\theta 2}$ are complex quantities with both real and imaginary parts varying with time whereas, Z is a constant which also has real and imaginary components, both having Ohms as unit. In a parallel plate system, if the medium is purely conductive, then Z is a real number, independent of the frequency, and with a value equal to the resistance of the space filled by the medium between the plates.

This is a function of the conductivity (σ) and the geometric dimensions [48]. However, if on the other extreme the medium is a pure dielectric, the impedance is a complex number with a zero real component and a value that depends on the frequency, permittivity(ε), and geometric dimensions [48]. The dependence of Z on geometric dimensions and intervening medium properties is used to detect anomalies in the medium.

The calculations addressed tendon sizes and duct thicknesses typical of segmental bridges. The electrical properties for the filler were experimentally determined values taken from Figure 3-4 and Figure 3-5. The general geometry and different geometrical defect configurations for the various computational cases are shown schematically in Figure 3-7 and Figure 3-8 respectively.

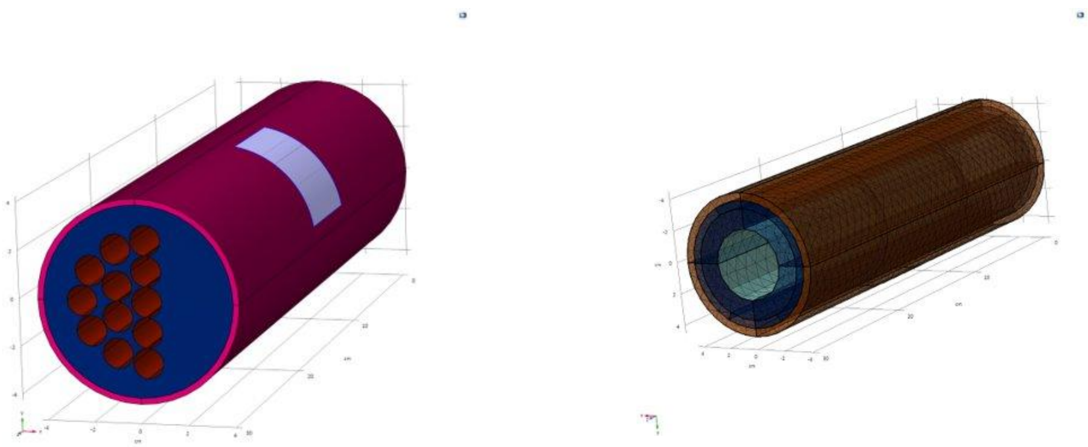

(a) (b)

Figure 3-7. (a) Image showing a tendon geometry modeled in COMSOL with strands and a sensing plate; (b) Modeled geometry of tendon showing the mesh configuration and strands simplified as an axial conductive cylinder.

Various possible deficiency shapes and dimensions have been modeled in COMSOL to determine the resulting impedance values. A general representation of possible deficiencies is shown in the Figure 3-8. In case of Figure 3-8 (c), the material properties, dielectric values and conductivity values were modified to represent an air void, dilute water and conductive water and evaluated independently. The major deficiency cases under analysis are possible inner voids, outer voids, full voids, full voids filled with dilute water, and full voids filled with conductive water.

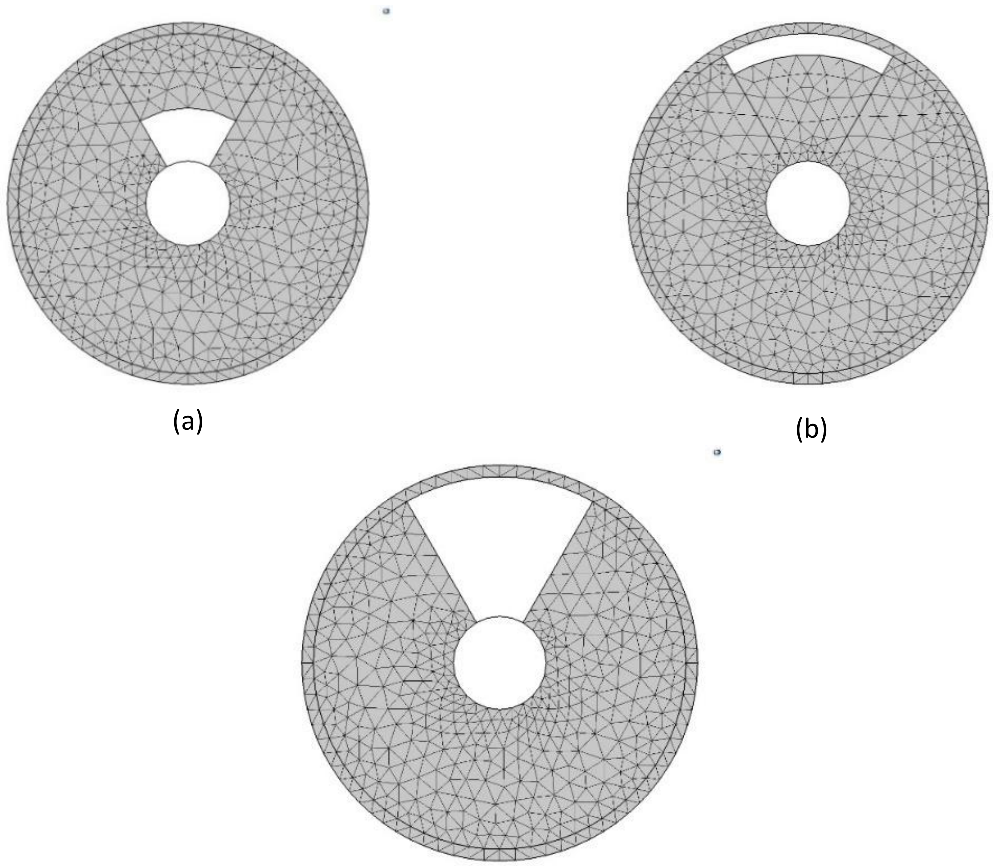

(a) (b) (c)

Figure 3-8. Representative cross-section of the geometry of tendons showing (a) inner air void; (b) Outer air Void; (c) full Void.

The model inputs included the geometric configuration of the system, the conductive and dielectric properties of the materials, the values of AC potential and frequency applied to the plate and strand bundle surfaces, and the boundary conditions for the domain interfaces. Table 3-1 consists of the input parameters for geometry construction and material properties. The physics-controlled FEM mesh configuration used tetrahedral elements, with default sizes of extremely fine, extra fine, fine and normal depending upon the sizes of the domain. Care was taken to make the elements size smaller than the domain thickness in each case to avoid any errors in meshing.

Table 3-1. Input parameters for the impedance model developed for different geometric and wax composite configurations

Parameter	Symbol	Value	Units	Remarks
Diameter of air space	D_A	18	cm	
Length of air space	L_A	50	cm	
Diameter of grout domain	D_W	7.99	cm	

Table 3-1 (Continued)

Length of tendon segment	L_T	30	cm	
Diameter of steel strand bundle	D_S	4.5	cm	
Boundary radius of inner and outer void	R_B	3.495	cm	
Angular spread of defects	θ_V	58	degree	
Thickness of duct	t_H	0.505	cm	
Sensing plate	W_P	5	cm	Width of plate
	L_P	5	cm	Length of plate
Length of void	L_v	10.2	cm	
Dielectric constant of HDPE	ε_H	2.2	-	
Dielectric constant of microcrystalline wax	ε_{Wx}	2.022	-	At 100 kHz
	ε_{Wx}	2.0055		At 1 MHz
	ε_{Wx}	1.999	-	At 5 MHz
	ε_{Wx}	1.985	-	At 10 MHz
Conductivity of microcrystalline wax	σ_{Wx}	4.24×10^{-5}	S/m	At 100 kHz
	σ_{Wx}	5.28×10^{-4}	S/m	At 1 MHz
	σ_{Wx}	1.57×10^{-3}	S/m	At 5 MHz
	σ_{Wx}	3.14×10^{-3}	S/m	At 10 MHz
Dielectric constant of water	ε_W	80	-	
Conductivity of DI water	σ_W	5.50×10^{-6}	S/m	
Conductive Aggressive Water (CW) Conductivity	σ_W	5	S/m	For NaOH water

The study was conducted for frequencies of 100 kHz, 1 MHz, 5 MHz, and 10 MHz. For each set of input variables, the plate was first centered at 0° on the perimeter. This process was repeated with the plate centered at 10° increments, completing a full 360° revolution. For each angle, the value of the complex normal current density i_T was calculated over the plate surface and integrated to obtain the total normal complex current $\tilde{I}$. The impedance Z was then calculated at each angle by dividing the applied electrical potential $\widetilde{V}$ at the plate by the integrated complex current density given in Equation 3-13.

3.2.2 Impedance model results

Figure 3-9 shows the results, modulus of impedance plotted against the rotation of sensing plate relative to fixed position of tendon, obtained from simulation of different geometric and wax composite conditions. The different colors have been used to represent the conditions of full void, inner void, outer void, distilled water and conductive water. Comparing the simulated impedance values with those in which grout is considered as the fill material, the impedance is much higher, as expected. Since the simplified impedance measurement system configuration suggests that full void condition should comparatively act more capacitive and less conductive, whereas CW condition should act more conductive and less capacitive. This was confirmed by the highest impedance values for the full void condition and the lowest for the conductive water from the results. As expected, peak and valley impedance values were observed at an angle of 60°, which corresponds to the position of the plate directly on top of the defects. At higher frequencies, the comparative impedance of inner void increased than outer void.

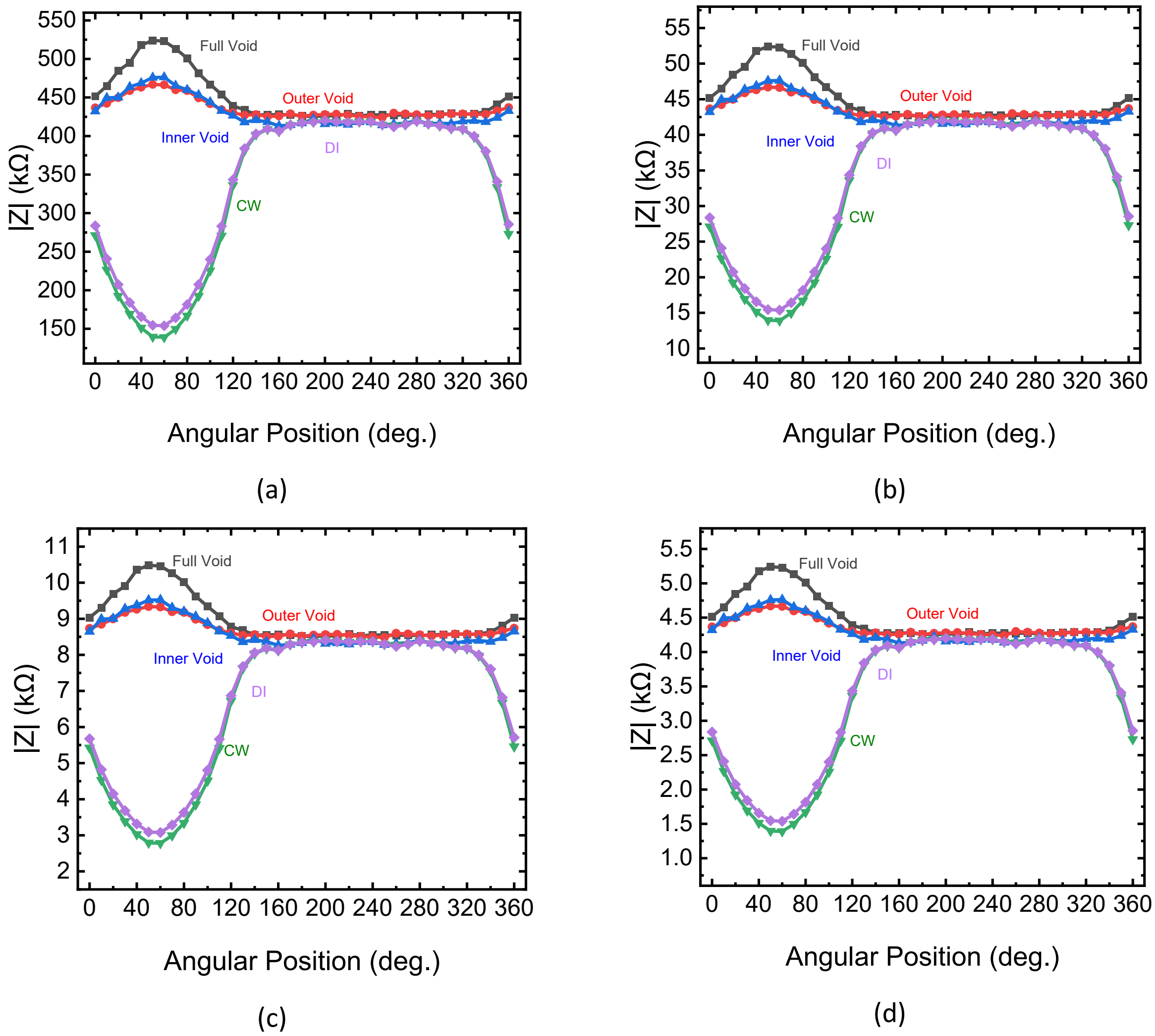

Figure 3-9. Modulus of impedance values calculated from simulations at frequencies as a function of angular position (degrees) of (a)100 kHz; (b)1 MHz; (c)5 MHz and (d) 10 MHz.

3.2.3 Selection of optimal operating frequency:

A deficiency detection figure of merit is a parameter expressed in log scale to better visualize the relative changes. It evaluates the sensitivity towards overall performance of model case outputs. Zr is a sign-independent indicator of proportional differentiation, suitable for the modeled simple circular strand bundle configuration. Mathematically, it is expressed as:

$$z_r = \left| \log_{10}\left(\frac{z_{Ex}}{z_{Bw}}\right) \right| \qquad \text{Equation 3-14}$$

where Z_{EX} is the extremal (peak or dip, depending on the nature of the deficiency) value in a graph plotting impedance modulus as a function of angular position (i.e. at 60° in Figure 3-9), and Z_{Bw} is the modulus of impedance at an angular position diametrically opposed to that of the center of the deficiency position (i.e. at 240° in Figure 3-9), where a normal wax condition exists. Higher values of Zr are better for detection.

The results presented in Figure 3-10 illustrate the modelling sensitivity under different wax-related conditions. The Zr values indicate that variations in air-void conditions are scarcely detected across the tested frequency range. Overall, voids filled with water are detected more effectively, whereas empty void conditions show lower detectability. The analysis further demonstrates that Zr sensitivity is largely independent of the frequencies examined.

The Zr results also indicate that the void-detection sensitivity of the TIU is lower for wax-filled tendons compared to grout-filled tendons. The percentage change in impedance values is approximately 23% for full voids and about 10% for small outer voids, while water-filled cases exhibit a percentage change exceeding 60%. A minimum impedance change of 10% relative to the background response can be considered sufficient for reliable detection using impedance-based technology.

Furthermore, the existing TIU operates at a frequency of 1 MHz without significant instrumentation complexity. Modelling results suggest that the current version of the TIU is also expected to perform effectively in wax-filled tendons.

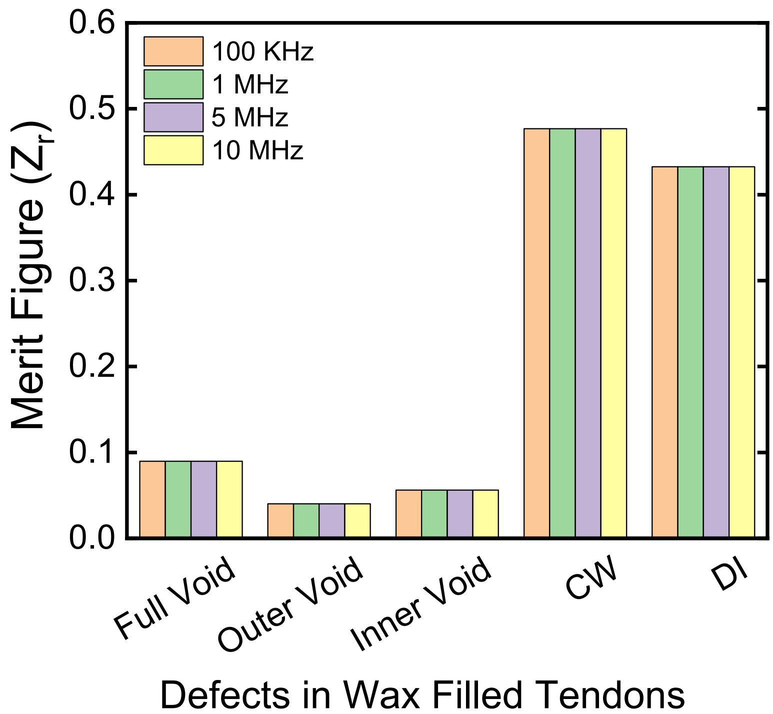

Figure 3-10. Graph showing the merit figure Zr (deficiency detection figure of merit) for different modelling cases.

3.2.4 Selection of optimal sensing plate size

Sensing plate size is another critical factor in determining the sensitivity of the TIU towards deficiencies. The size of the sensing plate, comparable to the size of the defect, produces better results. Various evaluations performed for the previous version of the TIU, for grout-filled tendons, led to the choice of 5 x 5 cm as the optimum size of the plate. The field conditions in the tendon's strands viz twisting and turns, positive and negative bending profile, environmental conditions etc., do not change on changing the filler material alone from grout to flexible fillers. Thus, the existence of similar sizes of defects in flexible filler filled tendons as in grout-filled tendons is assumed here on first approximation. The size of 5 x 5 cm was chosen provisionally as the optimal sensing plate size for the analysis.

In future unit configurations, an alternative method to the manual rotation configuration will be tested whereby multiple sensing plates are placed at various angular positions to minimize the need for rotation, thus, simplifying operation. To enable this capability, an alternative magnetic sensor configuration is proposed in which two coils are positioned in line, with a magnetic field established between them. The sensitivity of this arrangement to the location of the strands within the duct will be characterized in the next section according to model simulations.

3.3 Magnetic field simulations

As the impedance measurement between the sensing plate and the strands depends in part on the spacing between the two, it is important to account for this in the interpretation of the results to improve measurement accuracy and sensitivity. Similarly, both the shape and size of the strand envelope are equally important in the generation of a 2D color-coded cross-section image of the tendon. The challenge of determining the position and shape of the strand envelope in the previous version of TIU was met by using a magnetic force sensor in which the measured magnetic strength was calibrated to the distance of the strand bundle envelope. The technology used a permanent magnet of magnetic moment in the order of ~4 $A.m^2$ connected with a force measuring transducer assembly of the type used in electronic balances that rotates around the tendon and measures the force of attraction between the magnet and the ferromagnetic strand bundle. The data recorded by the force sensor is sent to the signal processing unit and finally to the laptop for post-processing to get the color-coded image. The basic design concept [49] is shown in Figure 3-11.

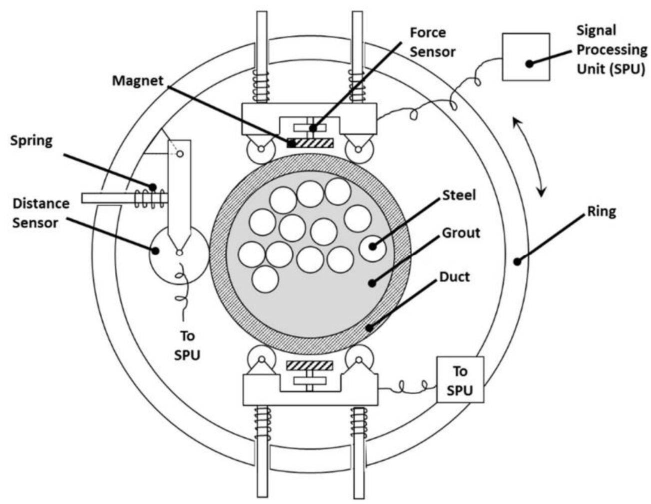

Figure 3-11. Schematic prototype of magnetic strands position detection technology [49].

Although this method provides a rapid, economical approach, it has its own limitations. The major limitation is the need to make a full manual rotation of the whole unit around the tendon. This manual rotation is not always steady while operating inside the enclosed box of segmental bridges with minimum clearance between the bunch of tendons, which results in uneven recording of data at different angular positions. Another constraint is the need to deduct the component of self-weight of magnet from the measured forces, depending upon its spatial position the inertial force caused due to rotation. Also, the presence of an active permanent magnet may sometimes pose counterproductive effects if proper care is not taken while operating near other electronic devices, such as laptop computers and smartphones.

To overcome some of the limitations of strand detection using a permanent magnet, a new electromagnetic approach was considered for further analysis. The new approach consisted of two coils positioned at a certain longitudinal distance from each other and the same transverse vertical distance from the strands. One of the coils (primary) is excited by passing an alternating current through it. The alternating magnetic field produces a changing magnetic flux through the ferromagnetic strands within the tendons. The changing magnetic flux passing through the strands excites the coil (secondary coil) in the pair. The EMF induced in the secondary coil was measured, and the signal strength was compared for different angular positions of the coil pair around the tendon. That signal is smaller or larger if the strand envelope is respectively farther or closer to the coil pair. If, instead of having only one pair, but rather multiple coil pairs placed at various regularly spaced angles around the tendon, a group of individual signal strengths from all those pairs would be obtained. That group information can then be used to recover in each case, the depth of the strand envelope from the outer surface. An image of that envelope can then be created, without needing to rotate the coil pairs, greatly facilitating image acquisition. The basic objectives of electromagnetic modelling are to determine the optimum number of sets of coils, optimum spacing between each set of two coils, number of turns in each coil, and optimum magnetic susceptance of core of each coil, to ultimately establish an equation that relates the changes in voltage in the secondary coil (coil 2) with the relative position of the strand and the coils.

3.3.1 Model description

A finite element model of the proposed magnetic approach was carried out in COMSOL Multiphysics Software Version 6.0. For simulations, the strands were modeled as ferromagnetic material. Also, primary and secondary coils of sizes that are commercially available were modelled. The entire system was enclosed by a finite spherical air domain. The dimensions for the different cases are listed in the the model inputs included the geometric configuration of the system, the conductive and magnetic properties of the materials. Primary and secondary coil domains were assigned the boundary conditions of circular coils. Also, a varying relative permeability values (500,1000,2000) were assigned for the inner core of coils. Table 3-2 consists of the input parameters for geometry construction and material properties.

The modeled domains included the surrounding air, coils with cores and the strands each with their electromagnetic properties. The frequency-dependent study simulations were performed using the 3D, AC/DC- Magnetic Fields Module in COMSOL Multiphysics, focusing on inductive and conductive effects.

The relation between the electric field and magnetic field is well established by Maxwell's equations. On passing the Alternating Current at a certain frequency through first coil, the governing equations are solved to calculate magnetic flux density (B) at each domains. Thus, calculated magnetic flux will lead to the desired electric coil voltage required to develop a distance to voltage relationship.

The model geometry as shown in Figure 3-12 for the electromagnetic modelling consists of the two coils (Primary and secondary coils) having 300 turns in each with a soft magnetic core. The electric current excitation was carried out in the primary coil, whereas the voltage excitation was measured in the secondary coil. The magnetic susceptance of the coil core was varied to check its effect. Similarly, the strands were modeled as simple circular cylinders and assigned the properties of ferromagnetic material. The polymer duct and flexible filler material were not defined because of their essentially non-conductive and non-inductive properties. A minimum distance equivalent to the thickness of the polymer duct always existed between the coils and the strands. The system was enclosed inside the air domain of 0.2 m diameter.

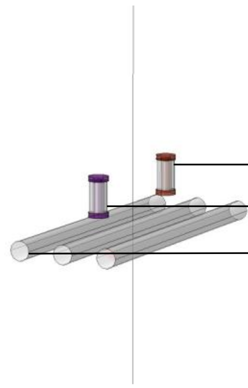

Figure 3-12. Image showing the geometry of electromagnetic model developed in COMSOL Multiphysics.

Table 3-2. Input parameters for electromagnetic modelling

Parameter	Symbol	Value	Units	Remarks
Diameter of air sphere	D_A	40	cm	
Length of steel strand	L_s	20	cm	
Diameter of the steel strand	D_S	1.27	cm	
Coil core diameter	C_D	0.58	cm	
Coil core height	C_H	2.02	cm	
Coil disc diameter	C_d	1.3	cm	
coil disc height	C_h	0.3	cm	
Distance between two coils	a	10	cm	
Distance between face of coils and strands	x	1,2,3,4,5	cm	
Number of turns in the coil	N	300		
Coil wire cross-section area	A	AWG 32		American Wire Gauge (Brown and Sharpe)
Coil wire conductivity	σ_{coil}	$6*10^7$	S/m	
Relative permeability of ferro metals	μ_r	500, 1000, 2000	-	
Frequency	f	100	Hz	Frequency of the domain

The physics-controlled FEM mesh configuration used tetrahedral elements, with default sizes of extremely fine, extra fine, fine, and normal depending upon the sizes of the domain. Care was taken to make the elements size smaller than the domain thickness in each case in order to minimize errors in meshing. The study was conducted for a coil excitation current frequency of 100 Hz. That relatively low frequency value is chosen to lessen the sort of complicated magnetic flux patterns that would have happened at higher frequencies, where current constriction due to the skin effect [50] would have been more severe.

3.3.2 Results

The results in Figure 3-13 show the dependence of the secondary coil signal on the distance between the face of the coil and the strands. The permeability value of the metals has no significant effect on secondary coil voltage response in the conditions tested. The dependence is in the direction expected, and quite strong. Therefore, these simulations clearly support the feasibility of the new approach. Trial experimental testing is in progress toward the adoption of the new approach, pending successful confirmation.

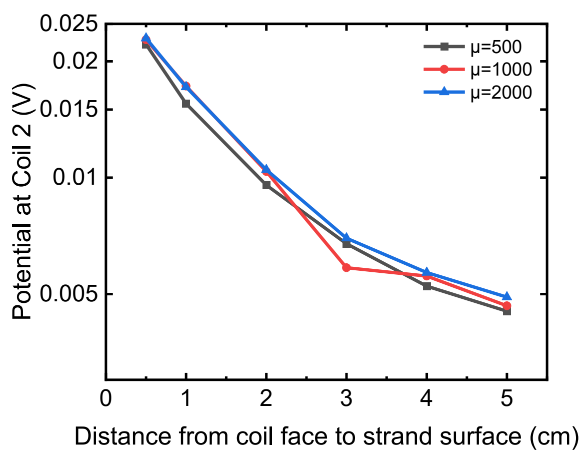

Figure 3-13. Graph plotted for potential in secondary coil in log scale versus distance from coil face to strand surface.

3.4 Summary

The sensitivity of the TIU decreases for wax-filled tendons compared to grout-filled tendons when detecting air voids, while the opposite trend is observed for water-filled voids. The results also demonstrate that sensitivity is largely independent of frequency. This behavior is attributed to the low dielectric constant of wax, which is close to that of air and remains relatively frequency-independent. Although the electrical conductivity of wax varies with frequency, its contribution to impedance is negligible compared to that of the dielectric constant. This is because wax behaves predominantly as a dielectric material with very low conductivity.

The overall sensitivity of the TIU is governed by the combined performance of the impedance sensor and the magnetic strand-position detection sensor. In grout-filled tendons, deficiency flagging relied primarily on impedance measurements due to stronger Zr responses. However, the results indicate that impedance measurements alone are unlikely to reliably detect very small voids (approximately 5 mm deep). To address this limitation, greater reliance must be placed on accurate strand-position determination. Integrating data from both impedance and magnetic sensors is expected to provide acceptable detection sensitivity. Consequently, limitations associated with impedance-based void detection in wax-filled tendons must be mitigated through a robust strand-position measurement system.

The proposed TIU configuration, therefore, incorporates both electromagnetic and impedance modules to collect the data required for cross-sectional imaging of external tendons. The optimized two-coil electromagnetic approach shows strong potential for future TIU designs that enable scanning capabilities. Modelling and analysis further indicate that variations in the electrical properties of flexible fillers due to temperature changes or wax type have a minor impact on defect detection sensitivity. As a result, no special provisions are required to account for variations in temperature or microcrystalline wax composition.

4 Unit fabrication (Task 2)

NOTICE: This section includes intellectual property material documented in U.S. Provisional Patent Application # 63/714,555 filed 10/31/2024, SYSTEM AND METHOD FOR IMAGING TENDON CROSS-SECTIONS FOR DETECTING VOIDS AND OTHER DEFICIENCIES IN EXTERNAL TENDONS WITH FLEXIBLE FILLERS. Disposition of this material is subject to the provisions of the Master Agreement covering research conducted by the University of South Florida under sponsorship of the Florida Department of Transportation.

The concept reported comprises a modified multiple sensor technology expected to minimize the need for unit rotation, increase speed of measurement, and facilitate more practical longitudinal tendon image scanning. The expected outcome by the end of the project period is a proof-of-concept unit intended for experimental use.

As a parallel objective to be reported in subsequent reporting periods, the software associated with the existing TIU intended for use on grout-filled external tendons will be modified to account for wax properties and improve sensor sensitivity according to an improved signal deconvolution algorithm. The intended outcome is a field deployable unit expected to have moderate sensitivity to deficiency detection in wax-filled tendons.

4.1 Introduction

This section presents the current state of development of a practical, operational tendon imaging unit (TIU) that will combine imaging of the strand bundle cross-section with imaging of deficiencies in the wax filler at that cross-section, to produce a near real-time view of the tendon cross-section at the place along the tendon chosen by the operator. The goal is to create a small and lightweight TIU that can be closed as a clamshell around the tendon place to be imaged and easily moved to sample other locations along the tendon. The TIU is to communicate via a cable (or wirelessly in possible future versions) with an ordinary laptop or tablet computer. The software created as part of this project will process the information provided by the TIU and display a tendon cross-section image color-coded to reveal the presence, position, and nature of wax deficiencies, if any. An additional goal for improved ease and speed of operation is to achieve imaging by simple positioning of the TIU at the desired place, without need to physically rotate the unit around the tendon, as was necessary in the previous generation TIU that was created for grout-filled tendons.

During the project period, the strand bundle imaging portion of the TIU was designed, developed, built, and tested as a successful proof of concept demonstration. As intended, imaging was achieved without the need for rotation of the TIU. Details of that progress are described in Section 4.2. Also, during this period conceptual design was completed and initial calculations were performed to implement the part of the TIU for imaging of filler deficiencies keyed to position of the strand bundle. Supplementing that activity, physical implementation of a system to produce impedance data without the need for rotation was conducted and experimentally demonstrated, as described in Section 4.3.

4.2 Strand bundle imaging concept and design

Strand bundle imaging was achieved using an electromagnetic steel strand sensor array. It consists of a pair of coil inductor ring arrays separated by about one or two tendon diameters, see Figure 4-1. Each coil in a ring is oriented as illustrated, with one end nearly in contact with the outer surface of the tendon. The coils are all identical, and each contains a ferromagnetic core. The coil rings are oriented so one of them is rotated with respect to the other by a fixed angle Θ. The principle of operation is summarized in Figure 4-2, which is an idealized lengthwise tendon section view. It is noted that Figure 4-1 and Figure 4-2 also include components for the filled deficiency imaging function, but those are addressed in Section 4.3.

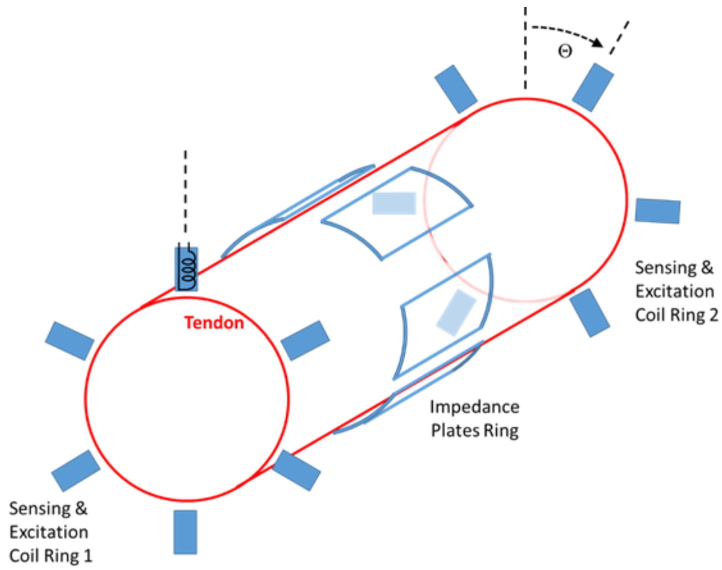

Figure 4-1. Physical arrangement of the sensor parts. Inductor coils winding is as illustrated in the detail. Coil ring 2 is placed rotated by an angle Θ with respect to ring 1. Patent pending.

In this method component, multiple partial measurements are conducted in rapid succession using multiplexing circuitry. In each partial measurement, one of the inductors (here in Coil ring 1) is operated in excitation mode, by circulating through the winding of the inductor an alternating current (AC) I_E. At the same time, another inductor (here in Coil ring 2) is operated in sensing mode. In that mode, the effective ac voltage V_S present between the inductor terminals, which is induced by the alternating flux originated by the excited inductor in ring 1, is measured and recorded. The figure exemplifies the simplest conceptual implementation, in which both coil ring orientations are the same (i.e., setting Θ=0), both coils in the pair are assumed to be in the same lengthwise position and orientation on a vertical plane, and an auxiliary ferromagnetic coupling bar has been added joining the backs of this and similar coil pairs. Therefore, the sketch in Figure 4-2 can be viewed as a simple elevation section of the tendon and sensors. Because the strands are under strong lengthwise tension, the strand distribution pattern on the tendon cross-section is nearly the same over the short length considered, and strand traces viewed on elevation are therefore nearly straight and horizontal. The coil-face to strand-surface distance $d=d_1 \sim d_2$ is thus a simple indicator of the position of the strand surface at the angular position of the coils considered.

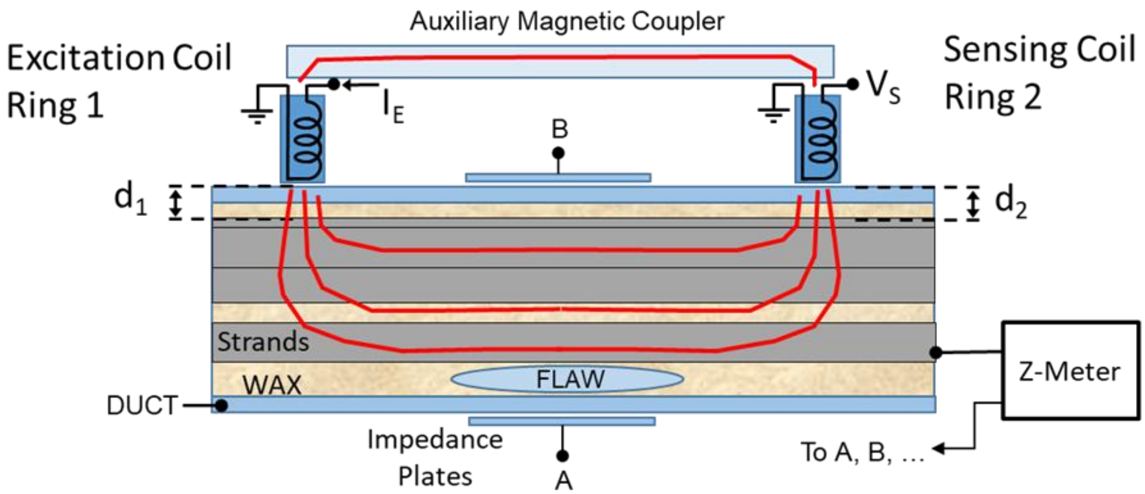

Figure 4-2. Illustration of principle of operation on a lengthwise section. The red lines represent notional magnetic flux lines. Magnetic coupler may be omitted. Patent pending.

Given the high magnetic permeability of the strands and the auxiliary magnetic coupler, the magnetic flux lines pattern follows a concentrated path, as illustrated by the red lines in Figure 4-2, establishing a strong coupling between the excitation and sensing coils. This situation resembles that present in typical reinforcing bar electromagnetic sensors. There, the induced AC voltage, $V_{S,}$ on the sensing coil tends to increase as d (which corresponds to gaps in the magnetic circuit) decreases. A single-valued mathematical function that roughly relates V_S to d or, rather V_S to d_E, the distance to the strand bundle envelope, which better accounts for the overall magnetic flux coupling, can be obtained empirically or by finite element modeling (FEM) following methodology analogous to that used for the development of previous TIU designs for grouted tendons.

In a basic strand envelope imaging procedure, measurements of V_S with the setting Θ=0 are obtained successively for each of the ring coil pairs around the tendon, using automatic multiplexing circuitry to transfer the excitation current (kept at a constant value) and voltage-sensing action to the next coil pair in the sequence. This results in a vector of sensing values V_{SV} = [V_{S1}, V_{S2}, …. V_{SN}], where N is the number of coils in either ring. The corresponding vector of estimated envelope-to-coil distance values d_{EV} = [d_{E1}, d_{E2}, … d_{EN}] is obtained using the previously determined approximate functional relationship between V_S and d_E. A graphic polar image of dE as a function of orientation angle with appropriate offset can then be made to provide an approximation of the shape and position of the strand envelope inside the tendon. Angular resolution (in radians) of the determinations on the order of $2\pi/N$. In this mode of operation, a value of N=6, chosen for the conceptual sketches in Figure 4-1 and Figure 4-2, is likely to be about the minimum necessary to provide useful information for the purposes of the TIU.

During the project, coil assemblies, driving electronics and software have been designed, created and operated to successfully demonstrate proof of concept for strand envelope imaging. Initial tests showed that the magnetic couplers can be discarded while still obtaining useful data. Operation without the coupler allows for greater compactness of the TIU and avoids false indications when the coil pair being sampled has a large d_E value. In such cases, the couplers over other nearby coil pairs may provide spurious short paths in the magnetic circuit, leading to potential interpretation of a smaller dE value than present.

The magnetic flux pattern without the coupler is greatly asymmetric compared to that in Figure 4-2, with a much smaller fraction of the flux that emerges from the excitation coil going through the sensing coil. However, both FEM simulations and preliminary experiments have shown that even with modest I_E values, the value of V_S is still large enough over typical noise levels to permit reliable determinations. The FEM simulations and experiments confirmed that in the configuration with Θ=0 there is strong differentiation of V_S upon d variations. V_S behaved in the expected inverse manner as d, and the differentiation was suitable for useful approximate strand envelope image reconstruction. Apparatus used during this reporting period for proof of concept implementation is shown in Figure 4-3.

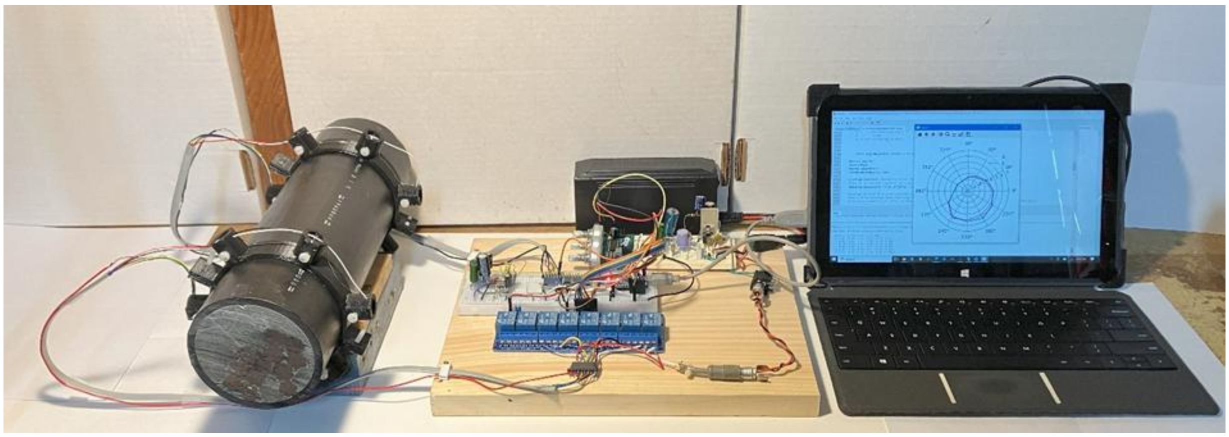

(a)

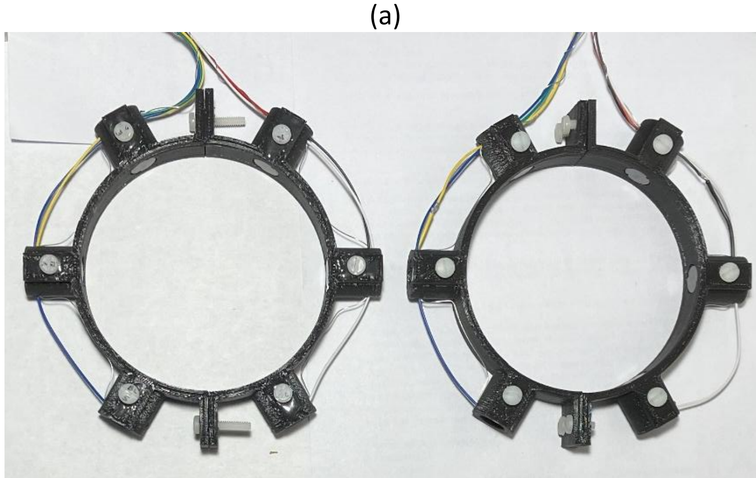

(b)

Figure 4-3. Physical proof of concept of TIU strand imaging function that does not require rotation around the tendon: (a) Tendon segment with coil assemblies, electronic excitation and sensing control circuits, laptop computer with Python code for operation, and on-screen display of as-measured strand envelope perimeter on tendon cross-section: (b) Twin coil assembly arrays for excitation and sensing respectively, that are fastened around tendon 180 mm apart, leaving intervening space for the impedance plates.

The tests used a grouted tendon segment from a prior project, with an HDPE duct 89 mm outer diameter, 5.5 mm wall thickness, ~300 mm long, 12 ½-inch strands, and a dummy un-grouted tendon segment of similar duct material dimensions but with 10, 0.6-inch strands. The coil arrays for excitation and sensing were identical and separated 180 mm on center along the tendon. Each array had six, 10 mHy commercially produced coils with ferrite cores, held in place by 3D-printed holders as shown in Figure 4-3 (b). The holders come apart in halves to allow positioning and reclosing on the tendon as shown in Figure 4-3 (a). In the TIU being developed, the holders will be articulated to accommodate a close fit on the surface of tendons that may be out-of-round or of variable size and hinged as part of a clamshell enclosure that allows rapid opening and closing on a selected tendon. That enclosure will also hold the impedance plates that will be in space between the two coil arrays, for a total TIU length of about 200 mm.

The electronic control for strand imaging consisted of an excitation coil driving and a sensing coil receiving train. The driving train had a 185 Hz ac signal generator, a power amplifier, and a relay bank multiplexer that sequentially powered the coils in the excitation array. The receiving train had an electronic multiplexer that, while each of the driving coils was energized, sequentially connected each of the sensing coils to the input of a signal amplifier.

An Arduino Nano–style (ANS) processor received commands from a Python program in the laptop computer. Per the program, the ANS digital outputs controlled the sequential excitation operation by the driving relay bank, and the synchronized sequential selection by the electronic multiplexer of the sensing signals to be amplified. The output of the signal amplifier was connected to a 10-bit resolution analog signal reading channel in the ANS. The Python code performed a real-time Fourier-transform analysis of the received signal and selected only the components that were within a ~ 20Hz band around the 185 Hz operating frequency, effectively eliminating spurious noise picked up by the coils. The result was a numeric value of the amplitude of the signal received by each of the six sensing coils, for each of the six driving coils. Those results were organized as a 6x6 numeric array, Vsp_{ij}.

The program then computed from the 6x6 array the averages Vs of the amplitude values obtained by each sensing coil when the various excitation coils were energized (S-organized data), and of the amplitudes obtained from all sensing coils when a given excitation coil is energized (E-organized data). Because the excitation and sensing coils are with matching orientations, S and E results are expected to be quite close to each other.

During this reporting period, a provisional method has been developed for approximate recovery of the strand envelope from the measured data and for its graphic presentation. To that end, the program makes a polar plot scaled version of Vs_S and Vs_E values. The plot includes the original values obtained at 60 ° intervals, as well as interpolated values for the intermediate 30 ° orientations. The 3rd power treatment is a provisional processing step emulating that used for the magnetic strand imaging of TIU developed under a prior FDOT project, for grout-filled tendons. The procedure creates, for each coil location, a point distant from the origin by a distance proportional to $Vs_{S,E}$. Since the signal is stronger the closer it gets to the coils in the perimeter of the tendon, the polar plot that joins the points is an approximate indication of the envelope of the strand bundle.

Once the program is launched and running, a polar plot with the results is ready for screen viewing ~5 seconds after the operator presses the keyboard button to request initiation of an image acquisition. Figure 4-4 shows the results for the two tendons tested, alongside photos of the actual strand arrangement in each case.

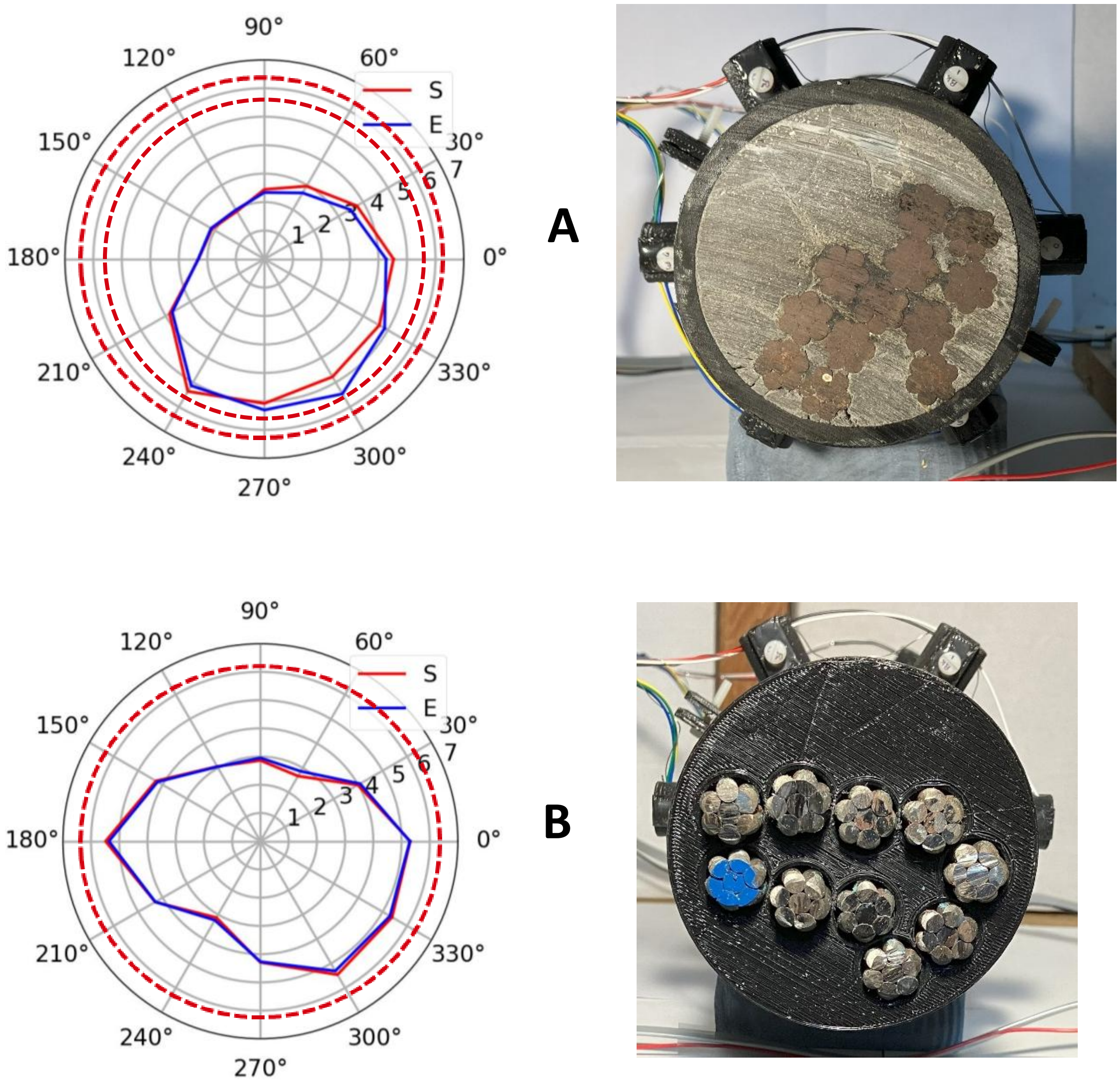

Figure 4-4. Results of strand envelope measurements using the provisional data processing and representation method (Left), together with picture of actual strand arrangements (Right) for a grout-filled actual tendon with twelve ½ inch strands (A) and for a tendon mock-up with ten 0.6-inch strands (B) The red and blue envelopes indicate the sensing and excitation coil measurements, respectively.

4.3 Impedance pattern concept and demonstration test

As indicated earlier, impedance values at a given angular position that are higher/lower than those expected from the corresponding magnetically determined strand envelope position are likely indicative of an air void/water presence, respectively, at that angular location. Thus, the determination of the impedance profile is an essential element of the TIU operation. To obtain that profile without need for TIU rotation, an impedance plate ring is placed in close contact with the outer perimeter of the duct, as it was shown in Figure 4-1. Electronic instrumentation sequentially measures the electric impedance between each plate and the strand bundle, at angular positions keyed to those sampled by the magnetic coil assembly described in the previous section.

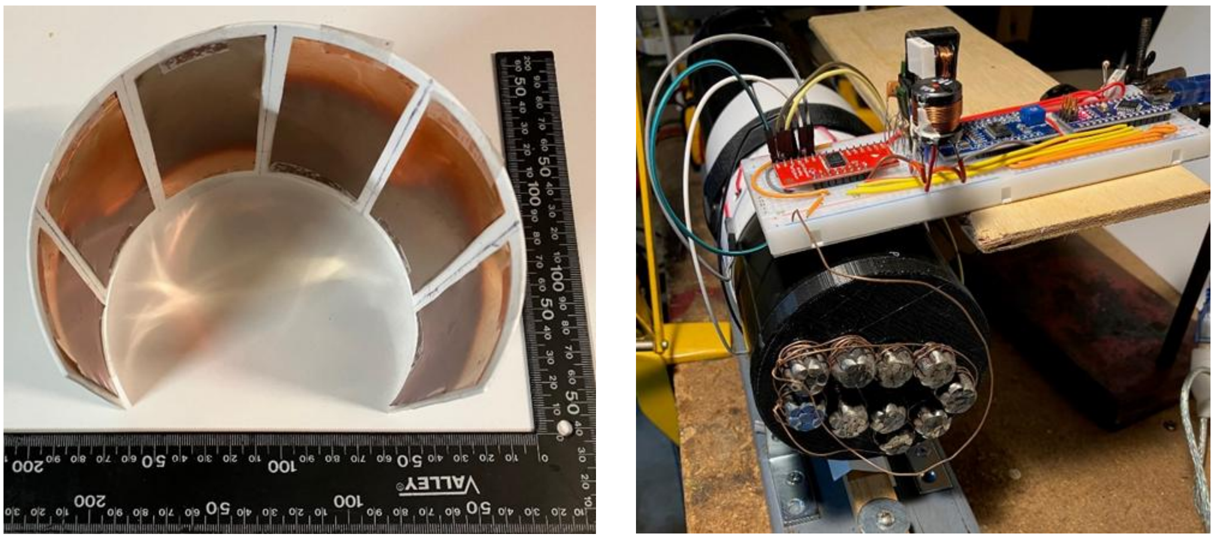

(a) (b)

Figure 4-5. Elements of the impedance profile measurement component: (a) impedance plate arrangement; (b) measurement setup.

For this concept demonstration, six thin copper plates, each about 40 mm by 100 mm, were bonded to a flexible plastic sheet that can be easily wrapped around the tendon duct and secured with a Velcro strip as shown in Figure 4-5 (a). Detachable thin connecting wires made a direct connection from each plate to a 74HC4067 multiplexing circuit placed with the other electronic components on a prototyping board, as shown in Figure 4-5 (b). Special provision was made to compensate for extra capacitance present at circuit input and outputs. The ground connection of the board was wired to the interconnected strand assembly. The board included an AD9850 ac generator, providing a ~1 MHz source that excited each plate sequentially. A rectifying discrete component circuit processed the plate potential signal and provided a dc value representative of the corresponding impedance modulus value. Multiplexer and generator are steered with an ANS, providing an automatic 6-value impedance result vector in seconds. The operation was controlled with a Python program that organized the output as polar plots.

The system was developed for initial optimization and tested by measuring the impedance pattern of a mock tendon segment of known configuration. The duct was uniformly air-filled, so the impedance pattern was expected to reflect the strand envelope configuration.

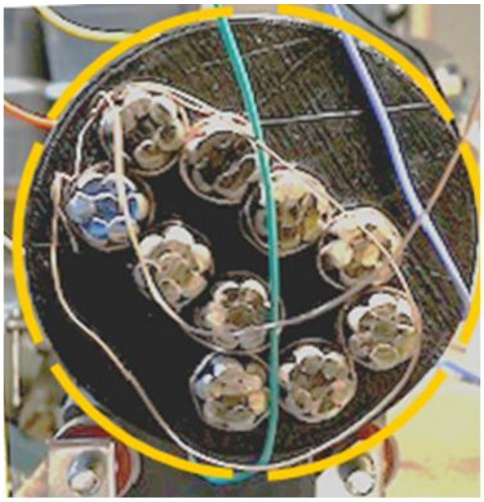

(a)

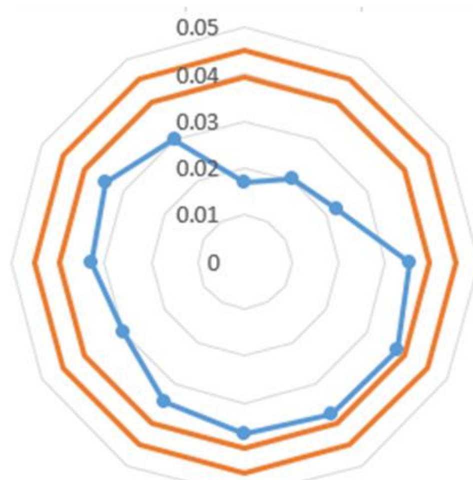

(b)

Figure 4-6. (a) Cross-section of an air-filled tendon mockup (same as in figure 4-4 b, rotated) with yellow lines marking the capacitor plate pattern; (b) Polar plot derived from the measured impedance vector, (blue) placed inside a geometric approximation of the inner and outer duct wall perimeter.

Initial results are shown in Figure 4-6: a) cross-section of an air-filled tendon mockup (same as in Figure 4-4. The polar plot was constructed from impedance measurements by a simplified treatment that assumed combined parallel-plate capacitor conditions. There, the local radial distance from the recovered strand envelope (blue line) to plate (on outer duct wall) was assigned a value proportional to the measured plate-strand impedance, with appropriate correction for the thickness and dielectric constant of the duct wall. The results were promising, as even with the simplifying assumptions used. The recovered strand envelope pattern captured both the general shape and the orientation of the strand bundle, clearly identifying the region of highest gap size between inner wall and strand.

The above test served as a convenient way to demonstrate the feasibility and promising performance of the automated impedance measurements, taking advantage of the knowledge of what behavior is to be expected for an air-filled duct. However, it should be recalled that the purpose of the impedance measurements is not to recover the strand envelope, but to discover fill deficiencies by determining how much the impedance pattern deviates from that expected from the strand envelope shape and a deficiency-free duct fill condition. An effort to further develop and improve magnetic-impedance pattern comparison methods for deficiency detection was conducted during the project period, via modeling and experiments.

4.4 Summary

Automatic methods and instrumentation were developed and successfully demonstrated to obtain angular profiles of strand envelope geometry and duct-fill electrical properties without physically rotating the sensing unit. These methods are well-suited for size reduction and can be conveniently integrated into a single unit, comparable to the current tendon imaging unit used for grouted tendons.

Future development of a rotation-free TIU will enable a rapid scanning modality that is more appropriate for large-scale field applications involving hundreds of feet of tendon. In the current point-by-point measurement approach, collecting data along approximately 700 ft of a single tendon at 20 ft intervals requires nearly four hours. With the proposed rapid-scanning mode, measurement time is estimated to be reduced by a factor of four, while also providing continuous spatial coverage rather than discrete measurement points, resulting in a more comprehensive tendon assessment.

5 Software modifications (Task 3)

NOTICE: This section includes intellectual property material documented in U.S. Provisional Patent Application # 63/714,555 filed 10/31/2024, SYSTEM AND METHOD FOR IMAGING TENDON CROSS-SECTIONS FOR DETECTING VOIDS AND OTHER DEFICIENCIES IN EXTERNAL TENDONS WITH FLEXIBLE FILLERS. Disposition of this material is subject to the provisions of the Master Agreement covering research conducted by the University of South Florida under sponsorship of the Florida Department of Transportation.

The previous section described efforts to develop a TIU concept that was fully redesigned for fast, uncomplicated operation, not requiring physical rotation of the shell around the tendon. That concept is ready for the next steps of miniaturization and practical construction, but those require further investment of time and resources. In this section, work is described on a parallel thrust to explore an intermediate approach that would take advantage of the availability of fully operational TIUs created under project BDV25-977-24 for deficiency detection in grouted tendons (Grout TIU). In this approach, the physical Grout TIU would be operated on a flexible filler tendon in the same manner as if it were a grouted tendon. However, the data analysis software was modified for increased sensitivity and discrimination to permit detection of deficiencies in the flexible fillers. Under this intermediate scheme, TIU operation would still require manual rotation. However, the optimized software served not only the immediate goal but was highly beneficial too for direct application in the next stages of development of the non-rotating TIU.

5.1 Problem statement

As noted in previous sections, detection of flexible filler deficiencies in the form of empty voids—the type most anticipated—is challenged by the relatively small factor of ~2 difference between the dielectric constants of wax and empty space. In equivalent circuit terms, the zone between the impedance plate and the strand envelope may be seen as the series combination of a fixed duct wall capacitance, and of the region between inner wall and the strand envelope. Given typical tendon and duct dimensions and wax properties, the overall capacitance (or its inversely proportional impedance) is likely to change only by about 30% or less between the cases where the inner space is filled with wax or completely void. With such small differences in the impedance response, it is difficult to distinguish between increases in impedance due to the presence of a wax void as opposed to those due to differences in the distance between the inner duct surface and the envelope of the strand bundle.

For comparison, the difference between the dielectric constant of grout and air could be as much as 50 depending on measurement frequency, resulting in a capacitance change between partially voided and nonvoided grout tendons of more than 100% in some cases. Such large variations in the impedance response can easily be dominant over the impedance changes that may be expected from variation in the distance between the inner duct wall and the strand bundle envelope. Therefore, the method of void detection for the grout TIU application was able to rely on an impedance threshold value to identify regions of voided grout. The threshold value was established mainly by experimental trials and informed only indirectly by considerations of the expected variation in the impedance response due to the distance to the strand bundle. That distance information was obtained according to a crude power-law approximation relating the measured magnetic force to the distance between the sensor and the strand bundle and used primarily to create the visual indication of where the grout deficiency was located with respect to the strand bundle. In summary, the simple threshold approach was adequate for the Grout TIU because even relatively small grout voids cause large impedance changes, making deficiency detection relatively easy.

The simple impedance threshold method would not provide adequate sensitivity to void detection in wax-filled tendon, due to the aforementioned limited variation in impedance between the voided and nonvoided cases. One approach to improve void detection sensitivity is to adopt a much more accurate way of determining the strand configuration from magnetic measurements. Provided with such a method, the strand configuration could then be used in the next computation step to inform the impedance profile expected for a nonvoided wax-filled tendon. Ideally, comparison of that profile to the actual measured response would reveal the presence of a deficiency. However, such a two-step approach would require detailed mathematical and measurement techniques that are presently impractical. Even if that were not the case, there would still be accuracy concerns in the predicted impedance pattern.

Due to those circumstances, a novel approach was formulated whereby the magnetic data pattern is directly transformed to a forecast impedance pattern expected to reflect the nonvoided condition, eliminating the need for an intermediate strand pattern determination step. In this task, the approach was developed and tested, yielding encouraging results. In the sections that follow, the magnetic transformation method is described and an example of how it works is provided, and a description of the next steps in completing the project objectives is provided.

5.2 Magnetic data transformation approach for impedance profile of nonvoided wax-filled tendons

The approach used involved the following provisions and steps, organized as a series of key points:

Using grout TIU on a wax tendon - processing data to detect wax voids.

- The Grout TIU produces measured values, as function of rotation angle α, of Magnetic force $F(\alpha)$ and Impedance Modulus $Z(\alpha)$.
- Key Point: The $F(\alpha)$ profile does not depend on presence of voids, but $Z(\alpha)$ does.
- Call $Z_0(\alpha)$ the Z profile that would be obtained if no void is present.
- To detect voids, the idea is to:
    - First use the $F(\alpha)$ profile data to estimate what $Z_0(\alpha)$ would be.
    - Then compare $Z_0(\alpha)$ and $Z(\alpha)$.
    - Presence of a void at a rotation angle αv will be manifested by $Z(\alpha v) > Z_0(\alpha v)$
    - If measured and/or estimated Z values are affected by an amount of uncertainty Zu, then void presence shall be flagged only if $Z(\alpha v) > Z_0(\alpha v) + Zu$.

How to get $Z_0(a)$ from F(a)?

- Estimation of $Z_0(a)$ from F(a) when the following info is known or reasonably estimated:
    - Tendon diameter
    - Duct wall thickness
    - Number and size of strands
    - Dielectric constants of Wax and Duct material
- Explored approach:

- Assume tentatively that transformation of $F(\alpha)$ into $Z_0(\alpha)$ results from convolution "*" of $F(\alpha)$ with a master kernel $K(\beta)$ <u>that is the same regardless of the geometric strand pattern within the duct.</u>
- With Z and F data as vectors Z1…i…n and F1…i…n (i indexed to a), convolution with K1…i…n means:

$$Z_0 i = (F*K) = \sum F_u K_{i-u+1}$$

Equation 5-1

Data processing and result

- Processing is facilitated by the convolution theorems in Equations 5-2 and 5-3 where (FT=Fourier Transform):

$$FT(F*K) = FT(F).FT(K)$$

Equation 5-2

with "." indicating term-by-term product.

$$FT(K) = FT(F*K)./FT(F)$$

Equation 5-3

with "./" for term-by-term division.

- If K is a master vector for all cases, then FT(K) can be determined by:
  - Taking one instance of strands' arrangement in a fully wax-filled tendon.
  - Measuring (or model-simulating) the resulting Z and F vectors.
  - Obtaining their FT's and then FT(K) per Equation 5-3
- Then, for any other instance of void-free tendon, the Z profile can be recovered from the magnetic F profile by doing FT(F) and performing inverse FT (IFT) per

$$Z_0(a) = IFT(FT(F).\ FT(K))$$

Equation 5-4

- Void detection could then proceed by simple comparison of the magnetic measurement – derived impedance values obtained per Equation 5-4 with the impedance values obtained from direct measurement.

Feasibility testing

The work performed under Task 5 then proceeded to provide answers to the following key questions:

- Is there a master K useful for all strand spatial combinations of a tendon family having a given size and dielectric constant properties?
- If such K exists, what is the sensitivity of the $Z_0(\alpha)$ recovered value to random or systematic errors in the $F(\alpha)$ data?

Action conducted to answer the above questions took place along the following steps:

- Perform Comsol simulation of F and Z response for multiple random strand combinations in a tendon family with otherwise fixed properties.
- For each instance, process the results to obtain FT(K) = FT(F*K)./ FT(F)
- Apply the FT(K) obtained for one instance (x) to the F outcome of another instance (y), thus obtaining $Zxy_0(\alpha)$ = IFT(FT(Fy).FT(Kx). Compare the extent to what $Zxy_0(\alpha)$ and $Zy_0(\alpha)$ match. Do that for all random combinations created. If results are favorable, obtain a "training set average kernel" by averaging all the kernels into a master kernel.
- Within a given recovery instance, add random error to the components of vector $F(\alpha)$ and determine to what extent the resulting $Zerr_0(\alpha)$ still matches the recovered $Z_0(\alpha)$. Perform for

various levels of applied error and establish a tolerable error level for the desired accuracy of Z outcome.

5.3 Results

Cases examined:

Figure 5-1 shows five cases examined by modeling. Case 1 (leftmost) reproduces the arrangement used for both modeling and experiment in the work described in Chapter 4 (pg. 35), while the other cases are randomized strand pattern configurations based on the same number and size of strands, with other properties of the tendon kept the same. Assignments of rotation angle α started as 0^o for 3:00 h and progressed clockwise

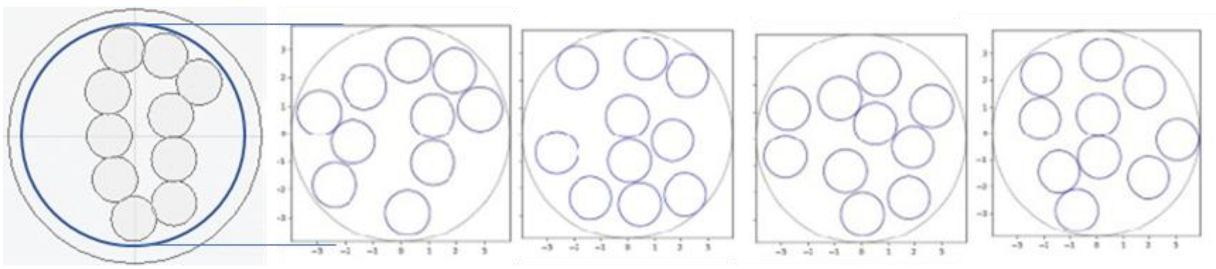

Figure 5-1. Randomized strand pattern Cases 1-5 left to right.

For each strand pattern case, simulations were made for a default condition where the tendon cross-section is completely filled with wax (“Full Wax’), and for a “Void” condition (exemplified for Case 2 in Figure 5-2) where wax fill is limited to one part of the cross-section, with the rest as an air void. Position of the void/sound wax demarcation boundary was the same for all five Cases.

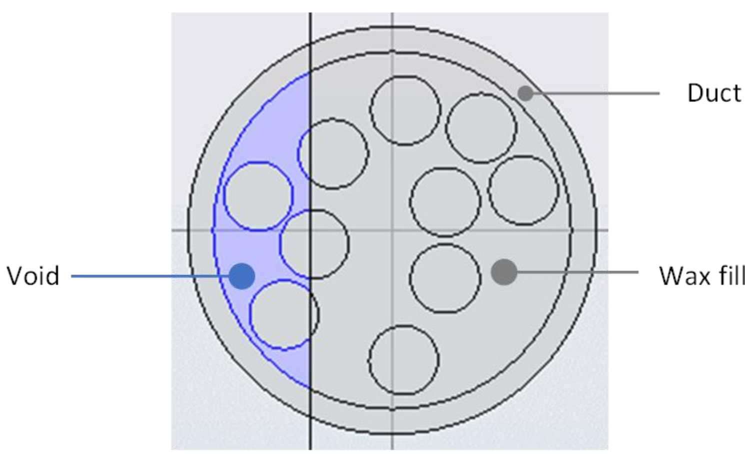

Figure 5-2. “Void” condition exemplified for Case 2. Device testing and implementation (Task 4).

Initial trials indicated that swapping kernels from different cases resulted in closely comparable outcomes, so the kernels specific for each of the cases were averaged into a master training set average kernel. The initial sets also indicated that the recovery of impedance patterns was improved by separate analyses for the zero and for all the higher angular frequency FT components. That procedure was adopted for all cases and proved to yield excellent recovery of the impedance simulated data from the magnetic simulated data. For ease of interpretation, all the impedance results have been represented by the equivalent circuit capacitance value. Because of use of symmetry reflection in the FEM calculations, the capacitance values reported should be multiplied by 2 to represent the full space system.

Typical results are exemplified in Figure 5-3 where the green line represents the simulated magnetic force data as calculated by the model for the Case strand arrangement. The corresponding values are displayed on the right ordinate axis. Blue dots are the recovered Full Wax capacitance pattern obtained using only: 1) the magnetic data, and 2) the training set average kernels for both baseline and higher angular frequency components. The yellow line is the "true" full-wax capacitance for the case as calculated by direct impedance modeling. Gray line is the "true" capacitance for the Void case, representing what would be expected from experiment. The red line is the error (Recovered Full minus True Full values), indicative of the uncertainty in the Full Wax evaluation.

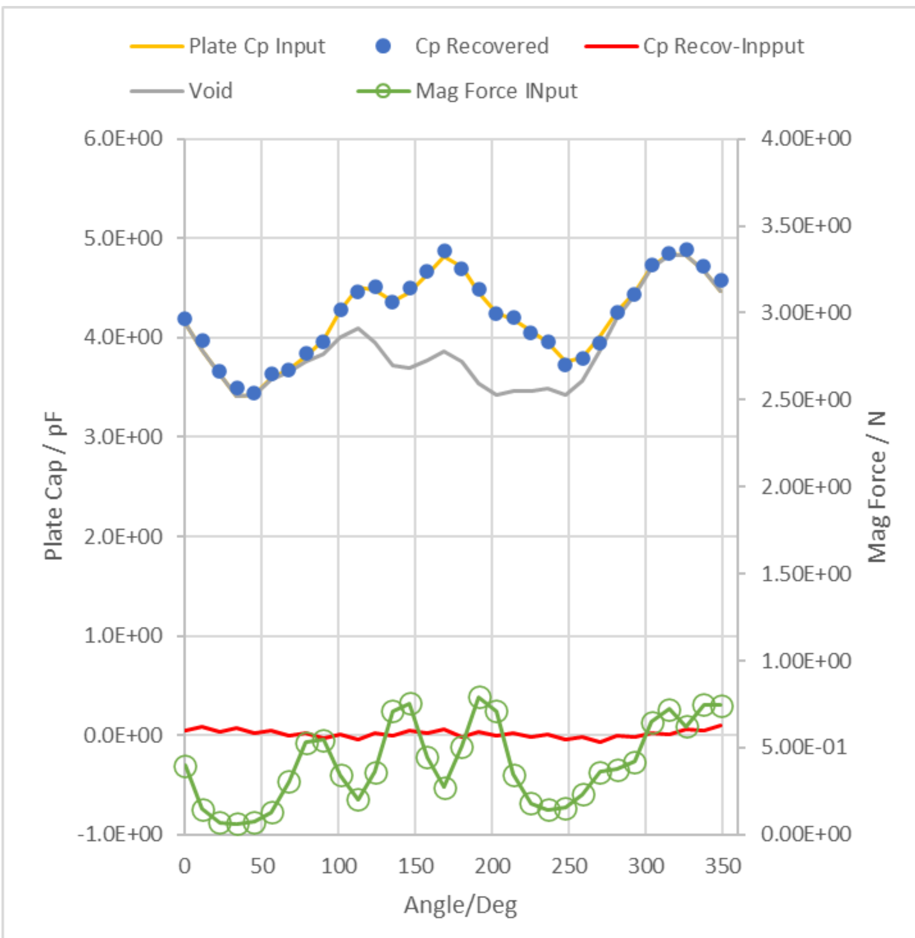

Figure 5-3. Example of results, Case 2.

The results exemplify excellent agreement between the directly modeled Full Wax capacitance values (from electrostatic FEM calculations based on capacitance plate and strand pattern geometry) and the values recovered by deconvolution from solely the simulated magnetic data (from magnetostatic FEM calculations based on magnet and strand pattern geometry). The agreement is evident in the direct visual overlap and by the small values in the red line, indicating the ability to recover within a small uncertainty percentage of the simulated data range examined. The agreement, therefore, is supportive of the concept that magnetic and electric behavior are related through a reasonably straightforward single-step convolution transformation, favoring a positive answer to the feasibility question posed earlier.

The result also showed that there is good potential for reliable detection of a void of comparable or larger size than that shown in Figure 5-2, since in the angular region affected by the void (from about 120 to 260 degrees), the gray line is below the Full Wax values by amounts often far exceeding the red line values.

Analysis of sensitivity of values recovered by deconvolution to random data errors has been limited so far to a few trial cases. Those results indicated that magnetic data random errors with standard deviations in the order of 11% resulted in appreciable degradation of the recovered capacitance, but that there was strong improvement when standard deviation was reduced to 5%.

5.4 Path forward

The concepts and calculations developed strongly support the feasibility of using software modification for successful use of the existing Grout TIUs to detect voids in flexible filler tendons. The modification could be readily implemented in the Matlab platform used by those TIUs by incorporating deconvolution kernels pre-calculated for each of the tendon types to be evaluated. Those previous calculations use Comsol software but need to be done only once for each of the tendon configurations to be tested (for example, for each of the most common strand and duct size combinations used by FDOT). As indicated earlier, the availability of this procedure is anticipated to facilitate the development of the non-rotating TIU in follow-up work.

6 Device testing and implementation

NOTICE: This section includes intellectual property material subject to the provisions of the Master Agreement covering research conducted by the University of South Florida under sponsorship of the Florida Department of Transportation.

The objective of this task was to provide experimental validation of the computer simulations presented in Chapter 5, which described a procedure to detect flaws in the flexible filler of external post-tensioned tendons. The procedure relies on a mathematical conversion of measured magnetic force data to an idealized flaw-free impedance response that can be compared to the measured impedance response. Any substantial deviation between the magnetic-signal-derived impedance and the measured impedance may be flagged as a fill deficiency.

Application of the procedure to TIU measurements on mock tendon assemblies is used to verify that the computer simulations can adequately capture the behavior in laboratory mockup tendon assemblies. The mockup tendons were assembled to consider the flaw-free condition as well as air voids and the presence of water pockets. To examine the extent to which the procedure may be extended to larger tendon sizes typical of field tendons, measurements were also taken on mockup assemblies used in a prior FDOT study from FAU (BDV27-977-10) [9]. In parallel with the above effort, the computerized data analysis procedure presented in the previous task was further improved to increase reliability over a broader range of conditions.

6.1 Mock tendon (MT) assemblies and measurement configurations

Four MT assemblies were constructed with dimensions approaching those used in the computer simulations presented in the previous task (Figure 5-1). They were constructed with an HDPE tube about 300 mm long, 89 mm external diameter, and 5.5 mm wall thickness, within which were placed ten ordinary 0.6-inch post-tensioning strands. The strand patterns used (designated A to D) and testing arrangement are shown in Figure 6-1 and Figure 6-2, respectively. The MT with the strands in place was oriented in a vertical position with filling conditions comprising (1) no-filler (only air), (2) filler only on the lower half, and (3) filler over the entire length. For selected conditions, the MT contained a mock void (MV) defect in the form of a 3-D printed shell with cross-section tailored to fill most or part of the space that existed between the strand envelope and the inner duct wall. In this case, the cross-section consisted of a segment of a circle with 76-mm external radius and 18-mm external depth, wall thickness 0.6 mm, and a 120-mm void length somewhat smaller than half of the MT length. The MV was attached to a stem that could be used to position the MV centered in either the upper or the lower half of the MT. Likewise, the TIU was supported so it could straddle and rotate around the tendon centered on either the upper or the lower half of the MT. The MV was tested in either the air-filled condition or containing 91.3 g of distilled water to a near-fill condition

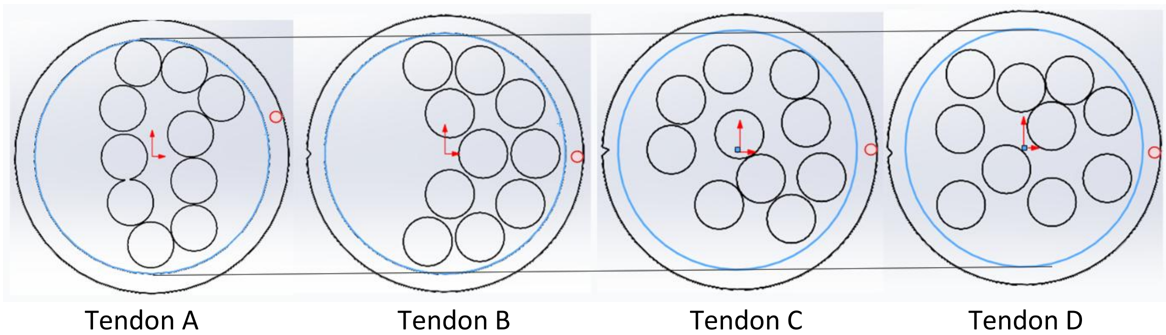

Figure 6-1. Strand patterns evaluated. Red dot indicates starting impedance plate position shown in Figure 6-4.

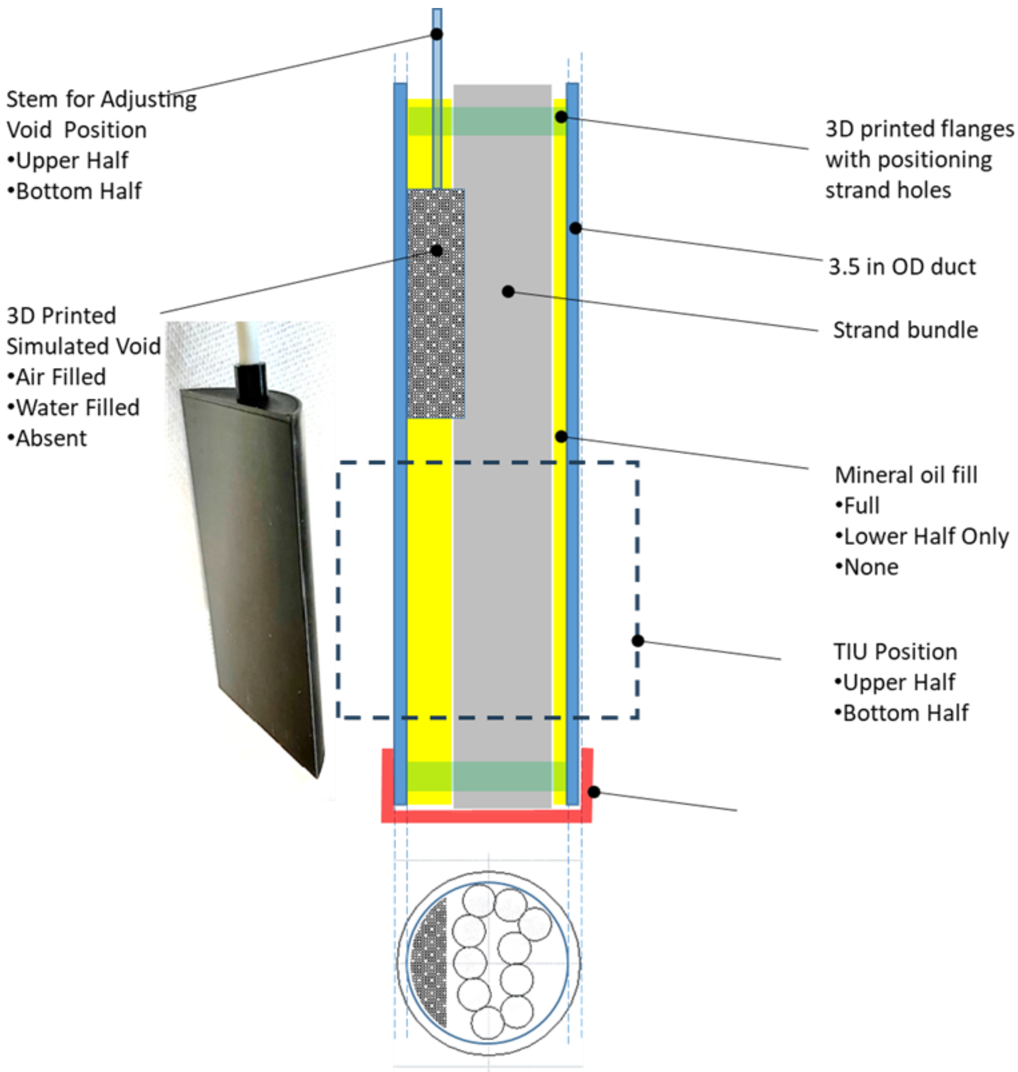

Figure 6-2. Testing arrangement and conditions evaluated.

Testing was performed for the most relevant combinations of tendon strand pattern, extent of oil fill, simulated void fill and TIU position. Figure 6-3 shows graphically some of the configurations tested and illustrates how they are designated. Four measurements were obtained considering combinations of top and bottom TIU and void placement conditions. The specific combinations are: Void Up TIU Up, Void Up TIU Down, Void Down TIU Up, and Void Down TIU Down. The same four configurations were also considered for the Half-oil Air Void and Full-Oil Water-Void conditions. Results for the principal cases of the MT with strand arrangement A (MTA) are representative of the overall findings and are presented in Figure 6-5 to Figure 6-10 in the form of profiles of impedance modulus |Z| as a function of angular position, as well as recovered cross-section representations. Figure 6-4 shows the orientation of the strands (seen from above the MT), angle θ of rotation convention, and position of the impedance plate at θ=0.

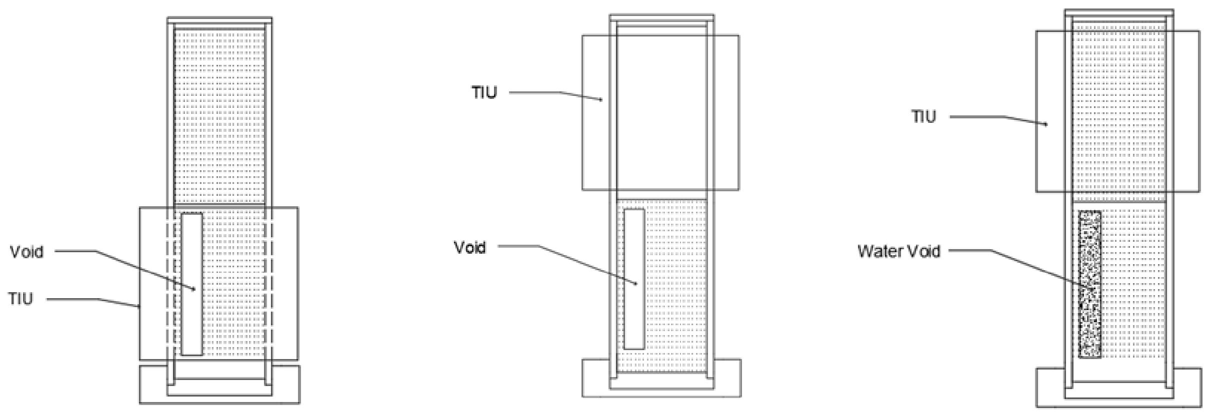

Figure 6-3. Illustration of condition descriptions. **Left:** Full Oil, Air Void, Void Down, TIU Down; **Center:** Half Oil, Air Void, Void Down, TIU Up; **Right:** Full Oil, Water Void, Void Down, TIU Up.

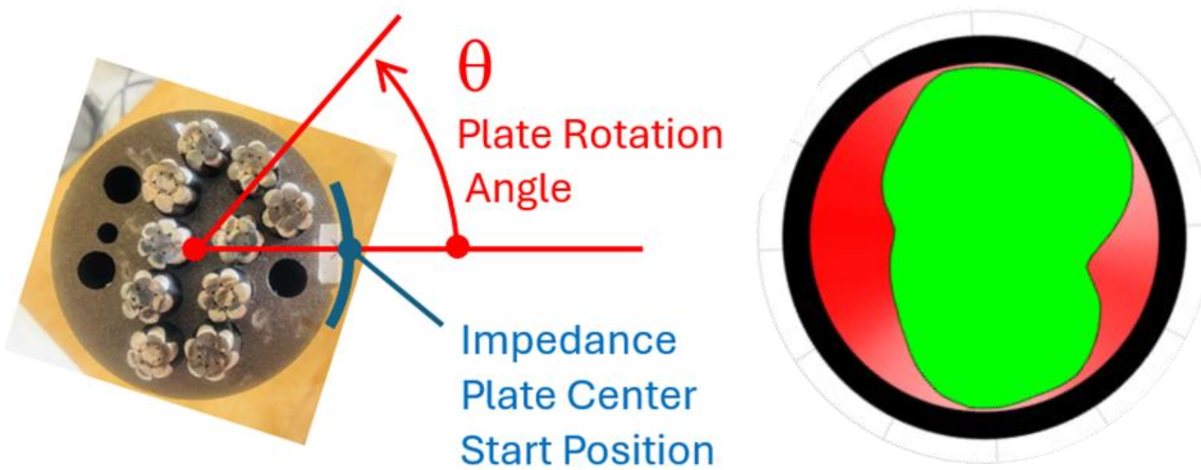

Figure 6-4. (a) Test orientation and angular coordinate, seen from above MTA; (b) Green field is typical on-screen image of the strand pattern in the MTA cross-section for all the conditions tested.

6.2 Development of cross-section image color representation

Tests were performed with a physical embodiment of MTA that closely approached that used for the tests described in 6.2.1. The tests were all performed in arrangements approaching the TIU Down position and the Air Void in both the Up and the Down positions. Several repeat tests were conducted with the Air Void Up, and the experimental magnetic force and impedance data were processed as described in the Task 3 report to obtain an experimental average Kernel FFT. Since the void was not present in the lower part of the MT, that kernel was representative of the flaw-free filling condition of the MT. Additional experiments with the Air Void in the Up and in the Down condition were then conducted, and the magnetic data of each were processed to recover, via an inverse FT (IFT) procedure, the nominal impedance profile that would have been observed in the absence of fill deficiencies. That recovered impedance was contrasted with the actual observed impedance, and the differences between both were used to color the strand-inner duct wall space with an intensity proportional to the difference. The coloring scheme was structured as follows:

The coloring scheme is aimed at cases where the only wax filling deficiencies anticipated are fully empty voids or fully water-filled voids.

Definitions:

- Ztrue = the measured impedance profile
- Zmag = the impedance profile that would have been observed in the case of no deficiency. Obtained as a recovery via IFT, using as inputs the measured magnetic force profile, and the previously determined convolution kernel prevalent in the conversion from force profile to impedance profile.
- deltaZ = Ztrue - Zmag
- deltaZrel = deltaZ / Zmag
- Sat[i] = color saturation at a given angular position [i]. Sat[i] =1 is full color. Sat[i] = 0 is white, linear blend for intermediate Sat[i] values.
- VT = Void threshold. Applies when deltaZ > 0. See significance below. Adopted VT = 1.14 based on experiment.
- WT = Water threshold. Applies when deltaZ ⩽ 0. See significance below. Adopted VT = 1.14 based on expectation.

Assignment:

- When deltaZrel [i] > 0 at a given angular position[i]:

  If deltaZrel [i] ⩾ VT - 1, a full void condition (air-filled gap extending from inner duct wall to strand envelope) is declared for that angular position, and Red color with Sat[i] = 1 is applied to the gap. If deltaZrel[i] < VT - 1, Sat[i] = deltaZrel[i] / (VT - 1)

- When deltaZrel [i] ⩽ 0:

  If - deltaZrel [i] ⩾ WT-1, a full water condition (water-filled gap extending from inner duct wall to strand envelope) is declared for that angular position, and blue color with Sat[i] = 1 is applied to the gap. If - deltaZrel[i] < WT - 1, Sat[i] = -deltaZrel[i] / (WT - 1).

An example of this is shown in Figure 6-13. For these tests, specimen orientation was rotated with respect to that used in the previous sections. The void, located on the left side of the tendon cross-section (centered at 180 deg), was successfully detected despite the minimal difference in impedance magnitude between the flaw-free case and the air void case. The void is indicated by the deep red color, signaling a high likelihood of a void being present. Notice that in one instance, there is also a light pink region on the right side of the tendon cross-section (0 deg) at a region where there is no flaw. Further improvement to the analysis procedure will help minimize the possibility of such false-positive indicators.

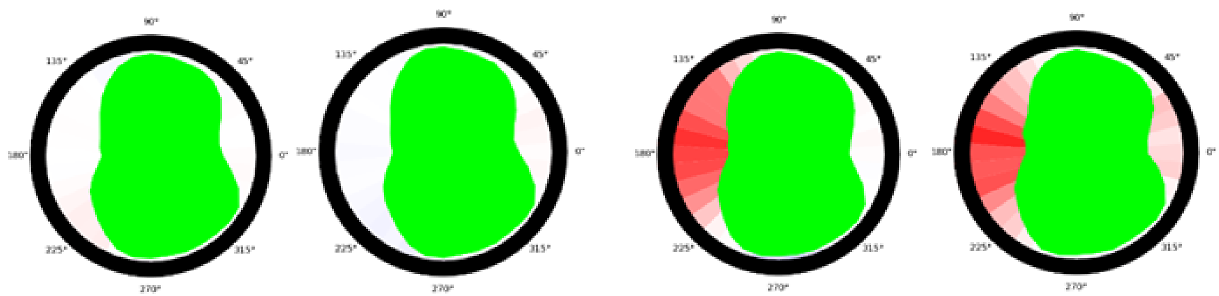

(a) (b)

Figure 6-5. Results of duplicate tests of condition with: (a) Full Oil-Air Void (Void Up TIU Down); (b) Full Oil-Air Void (Void Down TIU Down).

It is noted that these tests used a kernel derived from the conditions in MTA only, as opposed to a more demanding evaluation where a generic kernel would reflect the approximate conditions of an entire class of strand arrangements. Nevertheless, the results were highly encouraging in that the graphic display successfully captured the location of the void and provided a clear indication of the relative severity of the deficiency. This demonstration of the viability of the method will be followed by additional applications to the other deficiency conditions that have been newly implemented as described in the previous sections, and incorporation of results from MT with strand arrangements B-D (MTB, MTC, and MTD), as well as additional modeling cases, for a full evaluation of the procedure.

The data processing procedure presented in the Task 3 report was further improved by introducing a more general, analytical convolution kernel formulation to replace the empirical construction used before. It was found that in model calculations, a generalized gaussian convolution kernel, with only four adjustable parameters, successfully recovered the flaw-free filler impedance behavior of a test set of tendon profiles. Recovery was typically within ~5% of the target value, suggesting good prospects for reliable detection even of air voids like the ones considered in the previous sections.

6.3 Device testing results

The image recovery procedure was further validated by application to the experimental data obtained from measurements on MTA, MTB, MTC, and MTD. Detailed results are reported here for MTA, and the results of MTB, MTC, and MTD are provided in the Appendix.

The TIU was used to obtain measurements of the impedance magnitude as a function of rotation angle orientation, considering the tendon placement and fill configurations described in Figure 6-3. Results are presented here for the MTA strand configuration displayed in Figure 6-1, and those of MTB, MTC, and

MTD are reported in the Appendix. The results are used to showcase the sensitivity of the impedance response to fill configuration. Select cross-sectional image representations are reported for visual clarity. Also presented are the results of two of the FAU tendon assemblies that comprise unknown fill conditions with likely deficiencies. Measurements were performed at 3 locations to show possible variation in strand position and fill conditions along each tendon.

6.3.1 Mock tendon assemblies

MTA filled completely with oil is considered as a reference condition against which variations in the impedance profile due to fill deficiencies are to be contrasted. Figure 6-5 shows the influence of a simulated air void placed either within the top or bottom half of the vertically positioned MT. The conditions where there is uniform oil filling in the region between the impedance plate and the strand bundle (Void Up TIU Down, Void Down TIU Up) are representative of a properly wax-filled tendon. Essentially the same configuration and results are encountered for Half Oil-Air Void (Void Up TIU Down), Full Oil-Water Void (Void Down TIU Up, Void Up TIU Down), and Half Oil–Water Void (Void Up TIU Down). These conditions are the reference against which variations in the impedance profile due to fill deficiencies are to be contrasted. For this condition, there is uniform filling in the region between the impedance plate and the strand bundle, so the profile is expected to be ruled primarily by the system geometry, as there is no variation of dielectric material properties with θ. Thus there is a deep |Z| minimum at θ ~50 deg where 3 adjacent strands nearly contact the inner duct wall, a main maximum around θ ~180 deg where the strand bundle distance to the duct wall is greater over a wide angular range, a less marked minimum ~270 deg where two adjacent strands near the inner duct wall, and a secondary maximum at ~340 deg reflecting another, less pronounced, gap between the strand bundle and the inner wall.

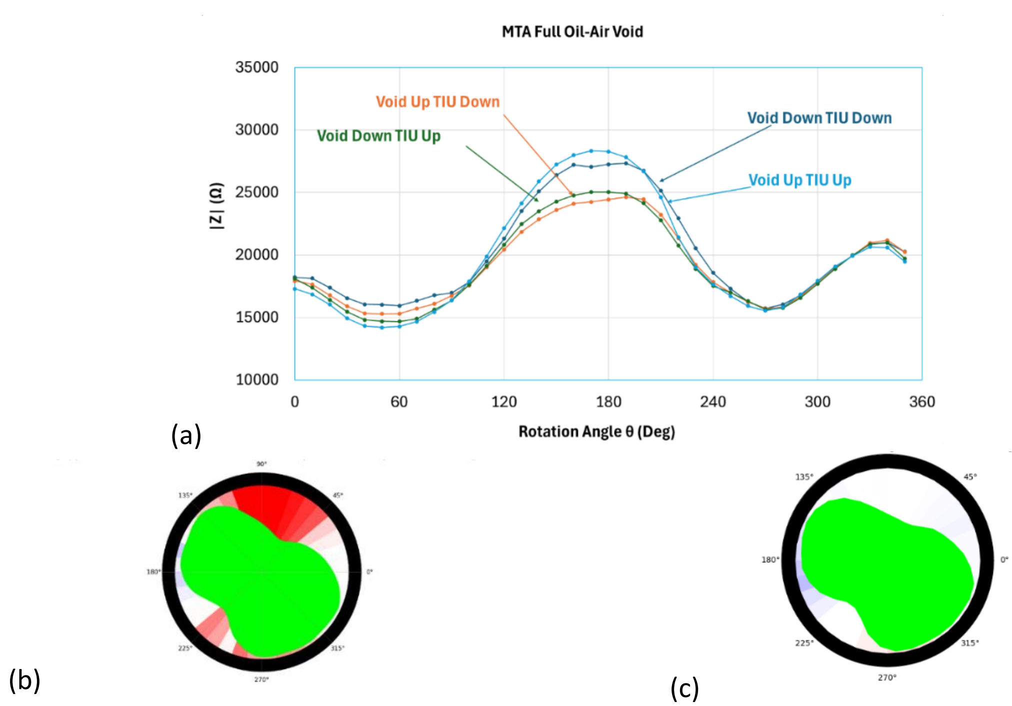

Figure 6-6. (a) Impedance magnitude as a function of rotation angle for the full-oil and air-void configurations. Schematic cross-sectional representations of the tendon and TIU orientation are shown for (b) the void-down/TIU-down configuration and (c) the void-down/TIU-up configuration.

The presence of the void in the test zone (Void Up TIU Up or Void Down TIU Down) is clearly manifested by an increase in the impedance in the angular region where the air void is present (~180 deg). The increase, however, is modest and only differs by about 12% from the reference condition there. Nevertheless, the image coloring scheme, as shown in the cross-section representation for the void and void-free case, was able to clearly identify the presence of a void.

The Half-Oil Air Void results, shown in Figure 6-6, permit direct comparison between the reference (no filling flaw) condition (Void Up TIU down) and 2 conditions of total absence of fill (Void Down TIU Up, Void Up TIU Up). The impedance profiles differ by as much as ~20% across the entire angular regime, but more notably where the strands are at some distance from the inner duct wall. Similar observations apply to the comparison of all the profiles in the No-Oil Air Void tests with their counterparts in the Full Oil-Air Void and the Half-Oil-Air Void tests. Thus, for the total absence of fill condition, detection of the flaw and evidence of its broad extent are clearly manifested.

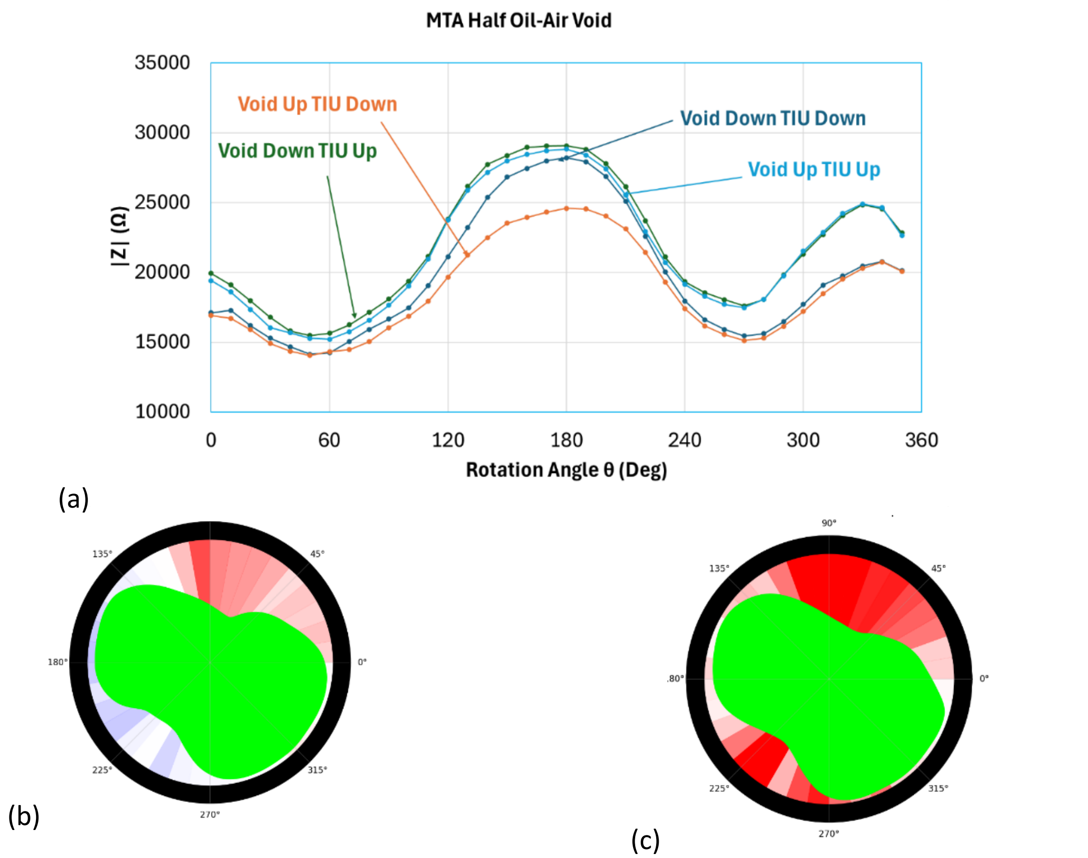

Figure 6-7. (a) Impedance magnitude as a function of rotation angle for the half-oil and air-void configurations. Schematic cross-sectional representations of the tendon and TIU orientation are shown for (b) the void-down/TIU-down configuration and (c) the void-down/ TIU-up configuration.

Cross-section color representations are shown for the Void down, TIU down (VDTD) case and the Void down TIU up (VDTU) case. The VDTD case presents a situation where there is a finite-sized void present in the wax fill. In this condition, the color representation does signal the presence of a void, but with less certainty than the full oil case shown in Figure 6-5. Additionally, there is a misidentification of water at the opposite end of the void location. The VDTU case represents a completely voided tendon duct, and the cross-section representation shows a high probability of void presence, indicated by the dark red at multiple angular positions of the cross-section.

The behavior in the Water(filled) Void tests, Figure 6-8, parallels that noted for the Air-filled Void tests, but in an inverted and much more strongly manifested fashion. The Full-Oil Water Void group shows in the reference condition (Void Down TIU UP or Void Up TIU Down) nearly the same results, as expected, as those for their equivalent tests in the Full-Oil Air Void group. The effect of the water void on the Water Void Down TIU Down and the equivalent Water Void Up TIU Up profiles is a striking reduction of more than 30% in the impedance value over the entire angular region spanning that of the void to nearly the impedance values observed with strands directly on the inner duct wall. Both the water void presence and angular position are unequivocally manifested. This strong effect results from the high dielectric constant of water, which may be more than 30 times that of oil and typical wax fill, effectively short-circuiting the conductive path between the inner duct wall and the strand assembly.

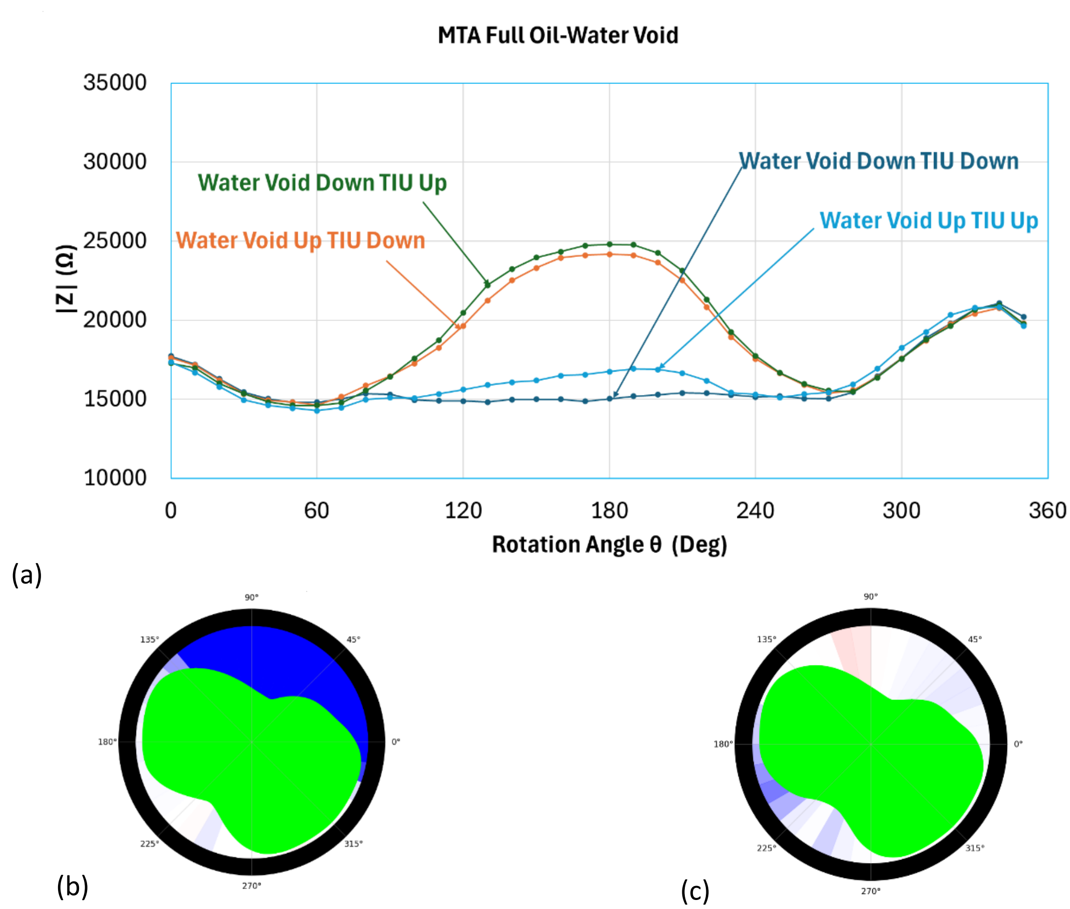

Figure 6-8. Impedance magnitude as a function of rotation angle for the full-oil and water-void configurations. Schematic cross-sectional representations of the tendon and TIU orientation as shown for (b) the void-down/TIU-down configuration and (c) the void-down/TIU-up configuration.

The corresponding cross-section representations show a clear indication of the water void (deep blue color) when placed in the same position as the TIU and only low probability indications of deficiencies (light blue or red) when the water void is placed in the opposite position as the TIU.

Corresponding effects consistent with the above behavior were observed in the Half Oil-Water Void and No-Oil-Water Void series, shown in Figure 6-9 and Figure 6-10. The manifestation was particularly strong in the latter case, with an approximately 40% impedance reduction. Such a reduction is to be expected since the behavior between no-fill (air) of the tendon and water-fill results from a dielectric constant ratio in the order of 80.

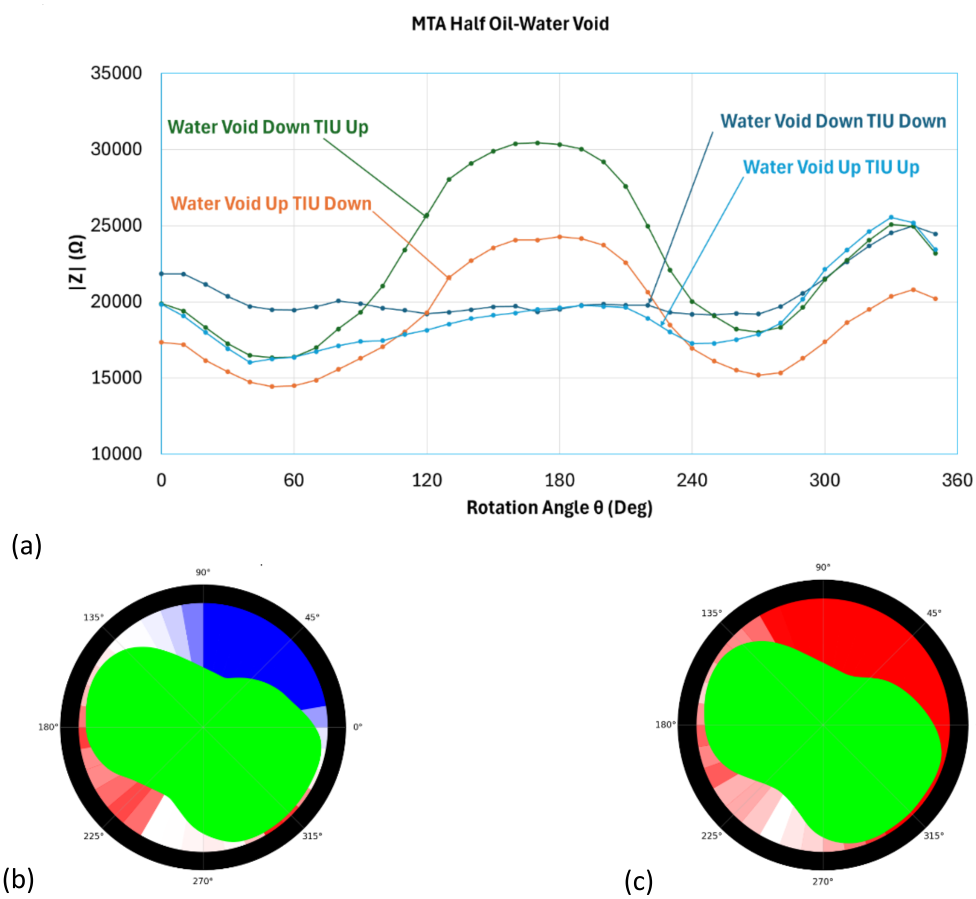

Figure 6-9. Impedance magnitude as a function of rotation angle for the half-oil and water-void configurations. Schematic cross-sectional representations of the tendon and TIU orientation as shown for (b) the void-down/TIU-down configuration and (c) the void-down/TIU-up configuration.

It is noted that in all these cases, the lower limit of the impedance that can be observed is dictated by the finite thickness and dielectric constant of the duct wall and the geometry of the impedance plate, resulting in a minimum value of about 16,000 Ω. Thus, while the impedance of the dielectric path between the strands and the inner wall can experience variations in the order of the dielectric constant ratios given above, the limit value acts as an added term to the denominator lowering the resulting variations to the order of the percentages noted earlier. In both cases, the presence of the water void in a voided region is indicated in the cross-section representation as a deep blue region and the voided region as deep red.

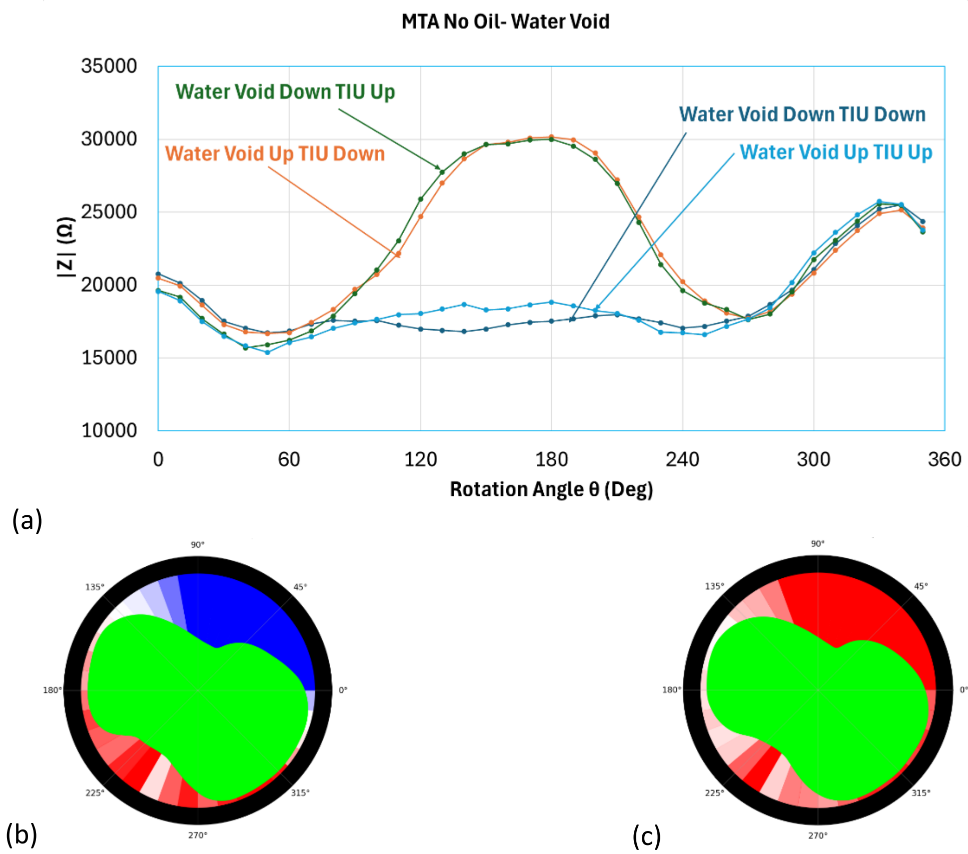

(a) (b) (c)

Figure 6-10. Impedance magnitude as a function of rotation angle for the no-oil and water-void configurations. Schematic cross-sectional representations of the tendon and TIU orientation as shown for (b) the void-down/TIU-down configuration and (c) the void-down/TIU-up configuration.

6.3.2 FAU tendon assemblies

The FAU tendon assemblies comprise 39 – 40 inch long, 4.5-inch outer diameter, wax-filled tendon segments cut out of large test pieces and used in the prior investigation at FAU under FDOT project BDV27-977-10. The tendons are assumed to contain 19 strands of 0.6-inch nominal diameter. The specimens were not individually identified so the tests conducted here were intended mainly to establish feasibility of data acquisition by the present method in an actual flexible-filler tendon case. Two segments (Tendon 1 and Tendon 2) were chosen for data acquisition at locations centered 6 inches from either end designated West or East, and at the segment mid-point. Results of the as-acquired data files are presented in Figure 6-11 and Figure 6-12.

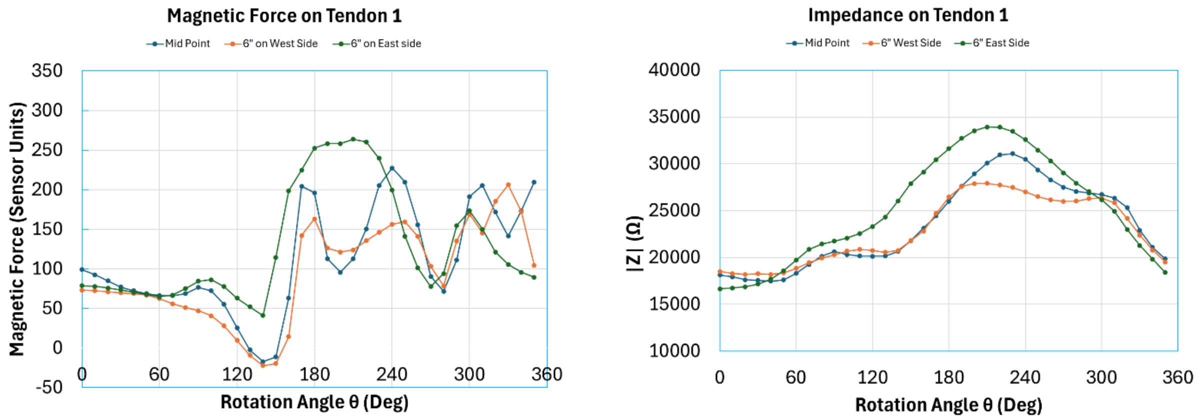

(a) (b)

Figure 6-11. FAU Tendon 1: (a) Magnetic force expressed as a function of rotation angle with TIU position as a parameter; (b) Magnitude of the impedance expressed as a function of rotation angle with TIU position as a parameter.

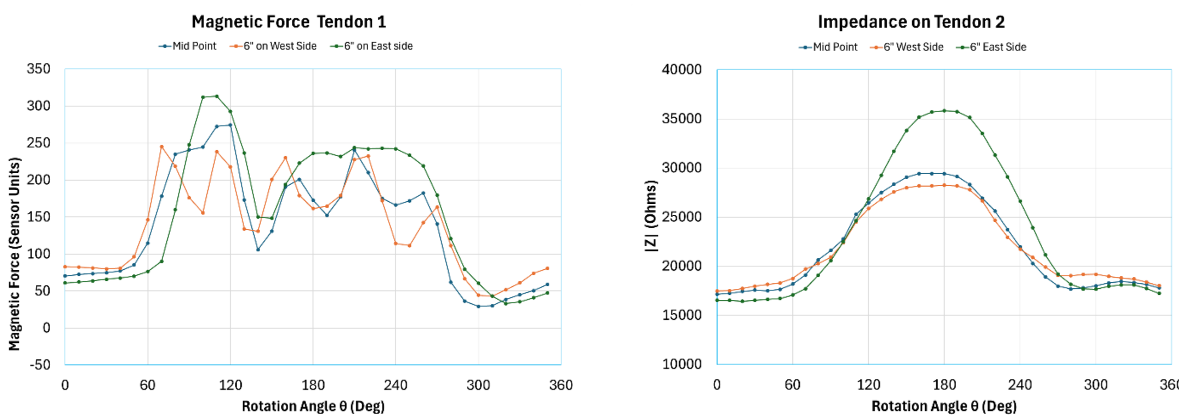

(a) (b)

Figure 6-12. FAU Tendon 2: (a) Magnetic force expressed as a function of rotation angle with TIU position as a parameter; (b) Magnitude of the impedance expressed as a function of rotation angle with TIU position as a parameter.

Data acquisition was completed successfully, and images of the internal strand arrangements were readily obtained as well as workable data files. The strand patterns in the cross-section images indicated that the strand alignment was approximately the same along each tendon end, so strands appear to be approximately parallel to the tendon segment axis. In agreement with that observation, within each tendon, the magnetic force angular dependence had general features similar in all three locations (for example, consistent force plateaus between 0 and 100 deg for Tendon 1). There was, however, some local variability in other regions.

The impedance behavior was more internally consistent. Minimum impedance values for both tendons were in the order of ~17 kΩ, consistent with the closest approach of contiguous strands in a typical tendon duct thickness case (as noted for the other experiments in this report). Both tendons showed general increase in impedance in the angular regions ~100 deg to ~300 deg suggesting clustering of the strands away from the inner duct wall in that region. Notably, both tendons showed increased impedance in that domain for the East end locations, to an extent comparable to that seen in the air void experiments detailed earlier, so the presence of a void in that region is considered likely. These data will be examined further including analysis correlating the magnetic and impedance response, and physical opening of the tendon ends to directly assess condition and validity of the interpretation of the TIU information.

6.4 Summary

The results of the simulated filler deficiency experiments have revealed that well defined but modest impedance variations are detectable for the case of an air void occupying about ¼ of the cross-sectional area of the tendon. The variations are consistently indicative of the fill deficiency presence and angular location. The results also indicated that complete absence of filler was more strongly manifested and detectable than the partial void. Manifestation of a water-filled void presence and angular position was strikingly stronger than for the air voids. This is a particularly encouraging finding as water presence is a high corrosion risk factor, and a known source of damage in tendons with deficient flexible filler. Thus, there is great promise in the use of the TIU to successfully detect water in wax-filled tendons, which is an important and favorable outcome of this work.

The initial FAU tendon tests established applicability of the TIU to acquire imaging data from a tendon size and strand configuration representative of actual structural practice, and to provide information interpretable for detection and location information of flexible filler deficiencies. Computerized processing for reliable filler flaw detection continued, producing a simplified procedure based on an analytical function with broader application than the method presented earlier.

7 Project outcomes

The project succeeded in its main objective of modifying the combined hardware and software of the Tendon Imaging Unit (TIU) to detect and display filler deficiencies in external wax-filled tendons. The work overcame several preexisting operational challenges and information shortages that sought to hinder appropriate design and implementation. The electric properties of various approved wax products needed to be fully characterized to facilitate sensor output analysis. Sensitivity to deficiency detection of the existing TIU designed for grout-filled tendons needed to be quantified to establish potential limitations when applied to wax-filled tendons. To optimize the TIU design for reduced measurement time that could facilitate large scale testing, an alternative design configuration was explored. Additionally, a novel sensor data interpretation method needed to be developed and demonstrated. Each of these challenges and how they were addressed is discussed in detail below.

7.1 Wax properties

While some information was available on the electric properties of paraffin or microcrystalline waxes, there was no such information on the specific waxes approved for Florida bridge tendons. Specifically, there was insufficient information on dielectric behavior, and its dependence on temperature and test frequency. Quantitative knowledge of the electric properties of the wax filler is essential for rational design of the TIU detection system as it relies on electrical impedance measurements to differentiate between adequate and deficient tendon fill. It was particularly necessary to determine to what extent if any the waxes deviated from ideal dielectric behavior, which is determined simply by the value of a dielectric constant. If such proved to be the case, it was also important to know how much the dielectric constant could vary with temperature. Such information would indicate whether the TIU ability to detect deficiencies may change with seasonal variations or be limited when trying to establish fill adequacy in a timely fashion when wax is still warm following injection and broader repair options may be still available.

Following a survey of the pertinent technical literature, dielectric property determinations were made using a specially constructed test cell that allowed impedance measurements of a space containing the wax to be assessed as a function of cell temperature in a range of 0℃ to 100℃. Measurements with a calibrated impedance analyzer were conducted with three of the flexible filler products specifiable by FDOT. All three products exhibited nearly ideal dielectric behavior, with flexible filler dielectric constant values ε_{FF} ~ 2, varying little over the temperature range examined. Moreover, ε_{FF} was found to vary relatively little as well as function of test frequency, in the range of interest of these tests in the order of 100 kHz to 30 MHz. Thus, the results indicated that relatively simple mathematical treatments of impedance behavior, with no important temperature dependence, could be implemented for the interpretation of test data to detect filler deficiencies that are manifested by deviations from the impedance behavior expected of a sound filler condition. Those deficiencies include the most important expected classes: simple absence of wax as in air filled voids, and the more severe condition of water being present instead of wax, due to water intrusion in voids or even insufficient flushing of preexisting moisture in the duct. Differentiation in impedance behavior from that of full wax presence exists in either case because air-void space has a dielectric constant ε_A ~1, while for water ε_W ~ 80.

7.2 Deficiency detection

It was necessary to determine the sensitivity to wax filler deficiencies of various expected types and degrees of importance that the TIU could achieve. Based on the findings of that effort, it was necessary to determine the hardware and software implementation strategies that would optimize deficiency detection.

The dielectric property results permitted assessment of the expected sensitivity of the test method when applied to the deficiency types of interest. In the existing TIU technology for grouted tendons, detection of air-filled voids is relatively easy, because at the operating test frequency (1 MHz) cementitious grout has a specific admittance about an order of magnitude greater than that of air. Consequently, after accounting for the intervening duct wall, the presence of a large void inside the cross-section results in a measured impedance value that may be twice that of sound grout condition. This effect is strong enough to provide a reasonable indication of the presence of a sizable air void with no need for detailed analysis of the data to establish a highly precise estimate of what the impedance behavior would have been in the absence of a deficiency.

For a wax-filled tendon, the presence of an air void is not as strongly manifested due to ε_{FF} being only about twice as large as ε_A. Multiphysics modeling of the system showed that after accounting for the presence of the intervening duct wall, the anticipated impedance increase due to an air void would not be much over 20% of that for a sound wax condition. Given the typical experimental scatter in TIU measurements (e.g, 10%), a reasonably confident detection of an air void in a wax-filled tendon would require being able to compare the measured behavior with a highly precise estimate of what the impedance would have been in the absence of a deficiency (baseline impedance). A method to obtain such a precise estimate was not available at the start of this investigation, and it was concluded that the development of such a procedure was needed.

In contrast to the above observations, detection of a water-filled void presented some degree of uncertainty for grout-filled tendons, since the impedance is quite low in a normal grout-filled tendon; further reduction by the presence of free water represented only a fractional effect. On the other hand, for wax-filled tendons, the presence of water, with ε_W almost two orders of magnitude greater than ε_W, creates an easily manifested strong impedance decrease. Thus, the application of the methodology that was to be developed to detect air voids in wax-filled tendons was anticipated to be amply sufficient for water detection as well.

7.3 Alternative design exploration

Additional knowledge was required to select an appropriate physical TIU design and operating methodology. Specifically, it was necessary to evaluate the feasibility, advantages, and limitations of alternative TIU configurations suitable for the application. One option involved a substantial modification of the TIU approach previously developed for grout-filled tendons. This concept combined non-rotating electrical impedance and magnetic attraction sensor arrays to simplify operation and increase testing speed. The second option retained the physical configuration and rotational scanning approach of the existing TIU used for grouted tendons but incorporated an advanced signal-processing framework specifically developed for wax-filled tendons.

The more innovative of the two TIU configurations examined comprised an array of six impedance measuring plates wrapped around the circumference of the tendon duct, and a corresponding array of six magnetic reluctance measuring coil pairs. Multiplexing circuitry sequentially interrogated those arrays. The results were the patterns of plate-to-strand bundle impedance, as well as the coil-to-strand magnetic coupling. Those patterns were electronically obtained as a function of angle of rotation around the tendon, but without need for physically rotating the sensing arrays. The patterns were then combined by software to construct an image of the cross-section, including the strand bundle and color-coded mapping of the condition of the wax filler. The electric and the magnetic parts of the system were independently developed, and their respective operation was experimentally demonstrated. Because of ease and reliability of operation (no need for physical rotation, magnetic information obtained by robust electronic means), this product of the investigation was deemed to be the most promising for TIU implementation in future work.

To focus directly on resolving the project challenges, development of the advanced physical design was deferred to a future research and development effort aimed at producing practical field-deployable units. Instead, to achieve the objectives of the current project, the existing TIU was utilized because of its ability to acquire angular impedance and magnetic attraction force data. The unit was operated on wax-filled tendons using the same scanning methodology previously developed for grouted tendons. However, the resulting data were processed using a novel imaging concept and software framework developed under this task specifically for the characterization of wax-filled tendons.

As indicated earlier, reliable detection of deficiencies in wax-filled tendons requires a precise estimate of the baseline angular impedance pattern. In this new method, that estimate is obtained by mathematical analysis of the angular magnetic pattern. The method is based on the results of Multiphysics modeling of wax-filled tendon configurations. The simulations revealed that the baseline angular impedance pattern is closely approached by a convolution operation of the measured magnetic force pattern (which is not affected by filler deficiencies) with a kernel function. The kernel is specific to the tendon and duct dimensions, and number and size of strands, but it is otherwise generic and practically independent of the actual strand pattern. Thus, given a tendon design, the generic kernel is obtained by modeling with the design specifications as input. The generic kernel can then be used in a deconvolution procedure to recover the baseline impedance pattern from the magnetic data at individual locations within tendons of the same design. Comparison of the measured impedance with the recovered baseline provides an indication of internal anomalies. Specifically, angular positions where the measured impedance exceeds the baseline are indicative of air-filled voids, whereas positions where the measured impedance falls below the baseline suggest the presence of water.

7.4 Analysis demonstration

The selected methodology, encompassing both hardware and software components, was developed into a functional proof of concept. This effort included experimental validation and successful laboratory operation of the system, establishing its readiness for further optimization and eventual implementation as a production unit.

The impedance deconvolution method was calibrated and verified first by application to a population of simulated random strand arrangements on a fixed tendon design. The method was then applied by taking TIU data of a quadruplicate set of laboratory mockup tendons, differing only in strand pattern, filled with a mineral oil fluid of dielectric constant closely approaching ε_{FF}. The mockups incorporated hollow inserts of various shapes and sizes that, when left empty or filled with water, simulated air-filled and water-filled voids, respectively. These simulated deficiencies could be positioned at different locations along the length of the mockup, enabling direct comparison between sound and deficient conditions. Additional tests were conducted to evaluate the response associated with the complete absence of filler material.

Software implementing the deconvolution methodology was developed and optimized. Application of the method successfully identified the various deficiency conditions, as well as the absence of deficiencies. The software generated a color-coded cross-sectional map, with the color type and intensity corresponding to the identified condition and the associated level of confidence. Overall, the experimental results validated both the inspection methodology and its laboratory implementation, demonstrating the feasibility of the approach and providing the foundation for development of a field-deployable unit for bridge applications.

8 Recommendations for widespread implementation and standardization

8.1 Development of scanning mode device

Current bridge tendon inspections using the manually rotated TIU involve discrete measurement locations that require installation of the TIU, connection to a computer, manual rotation to perform a circumferential scan, and subsequent removal and relocation of the device to the next inspection location. The time required for a single measurement, including setup, data collection, and relocation, can be several minutes and typically requires at least two personnel. Recent field testing has shown that measurements can only be performed at approximately 30 locations over a five-hour period. While effective for targeted investigations, this process limits inspection speed and practicality for bridges containing thousands of feet of external tendons. Further advancement of the scanning capability would facilitate rapid screening of large tendon inventories, significantly reducing inspection time while providing more comprehensive coverage of tendon condition.

An additional limitation of the manual rotation device is the added complications in inspecting tendon ducts with non-circular geometries, such as the elliptical cross-sections commonly encountered near diabolo transitions. Because the sensor response is highly sensitive to the distance between the sensor and the prestressing strand and the impedance plate presses on the duct surface through the aid of springs, variations in duct geometry can introduce measurement variability during manual rotation. Any deviation from duct roundness can result in changes in sensor-to-strand spacing around the circumference, potentially influencing the measured response and increasing uncertainty in the inspection results.

Ideally, the TIU would be capable of rapidly scanning along the full length of each tendon immediately following tendon fill placement to provide a direct assessment of fill completeness without the need for circumferential rotation. Such a capability would allow contractors and owners to identify voids or other anomalies before the structure is placed into service, reducing the likelihood of long-term durability issues. The establishment of baseline condition immediately after construction would also provide a valuable reference for future condition assessments.

A proof-of-concept non-rotating Tendon Imaging Unit (TIU) that eliminates the need to manually rotate the inspection device around external post-tensioned tendons has been successfully developed during the current project. The prototype demonstrated that an array of multiplexed magnetic and impedance sensors can recover tendon strand geometry without rotation, establishing the technical feasibility of a next-generation inspection platform. Also, without the need to rotation the device, tendon ellipticity may no longer be an issue. However, the current prototype remains a laboratory-scale system requiring separate magnetic and impedance measurement configurations and is not yet capable of continuous longitudinal scanning of bridge tendons.

Further work is required to miniaturize the unit and integrate the magnetic and impedance sensor arrays into a single compact device. In addition, software development is needed to create continuous scanning algorithms capable of reconstructing tendon cross-sectional images while the device is in motion and generating longitudinal condition maps that identify and geolocate grout voids, water intrusion, and other anomalies.

A key challenge for continuous scanning applications will be data acquisition and communication. The current system relies on a direct USB connection to a computer, which limits mobility and is not well suited for rapid field deployment. The incorporation of wireless data transmission, such as Bluetooth communication, has been explored as a means of eliminating the physical connection between the TIU and the data acquisition computer. This capability would increase operator mobility, simplify field operations, and facilitate the development of a practical continuous-scanning platform capable of collecting and transmitting data in real time as the device traverses the tendon. The integration of wireless communication and automated data processing will be essential for transitioning the technology from a laboratory prototype to a field-ready inspection system suitable for routine deployment on large bridge inventories.

8.2 Implementation and standardization

For widespread adoption, the technology should be standardized as a quality assurance and condition assessment tool for external post-tensioned tendons. Standards should define inspection procedures, reporting requirements, and equipment performance specifications to ensure consistent, comparable results across operators, bridge owners, and manufacturers. A practical implementation framework would apply TIU inspections throughout the tendon life cycle. Initial inspections should be performed immediately after tendon fill placement to verify complete filling and detect voids before construction is finalized. Subsequent inspections can be integrated into routine bridge inspection programs, particularly for structures with durability concerns or a history of tendon corrosion. Baseline measurements collected after construction would provide a reference for detecting future changes associated with water ingress.

Achieving repeatable results will require standardized inspection protocols covering scanning speed, sensor calibration, data acquisition density, tendon access requirements, and quality control procedures. Operator training and certification should be established to ensure proper equipment use and data interpretation. Automated processing and defect classification will reduce subjectivity and improve consistency. Inspection results should include cross-sectional and longitudinal condition imagery, along with quantitative confidence metrics for defect identification. Integration with bridge and asset management systems would enable condition tracking, deterioration analysis, and repair prioritization across bridge inventories.

Equipment standards should define minimum detection capabilities for voids and free water and be supported by validation testing on representative tendon specimens with known defects. Probability-of-detection metrics and accuracy assessments would provide the basis for performance-based specifications and technology qualification independent of hardware configuration.

References

[1] D. Dukeman, "Device for Imaging Cross-Section of Post-Tensioned Structural Tendons in the Field," M.S. Thesis, Department of Mechanical Engineering, University of South Florida, Ann Arbor, MI, USA, 2019.

[2] H. Freif, D. Dukeman, A. A. Sagüés, and C. L. Alexander, "Development of Tendon Imaging Sensor" University of South Florida, Department of Civil and Environmental Engineering, BDV25-977-24, August 1 2019. [Online]. Available: https://rosap.ntl.bts.gov/view/dot/54549

[3] FDOT Research Showcase. "Flexible Fillers Bring Increased Corrosion Protection to Post-Tensioned Bridges." https://fdotresearch.com/2017/07/05/flexible-fillers-bring-increased-corrosion-protection-to-post-tensioned-bridges/ (accessed.

[4] T. S. Theryo, "Design Guidelines and Detailing Update Related to Post-Tensioning and Segmental Bridges," in *FDOT Transportation Symposium*, 2019.

[5] ACI-ASCE Committee 423, "Report on Corrosion and Repair of Unbonded Single Strand Tendons," Farmington Hills, MI, USA, ACI 423.4R-14, 1998.

[6] D. A. Canonico, J. C. Griess, and G. C. Robinson, "Final Report on PCRV Thermal Cylinder Axial Tendon Failures," Oak Ridge National Laboratory, Oak Ridge, TN, January 1976.

[7] C. F. Castaneda, "Flexible Filler Corrosion Protection of Unbonded Post-Tension Tendons," Master of Science M.S.Thesis, Florida Atlantic University, 2017.

[8] D. J. Naus, C. B. Oland, and J. F. Costello, "An investigation of tendon corrosion-inhibitor leak into concrete," presented at the International Conference on Life Prediction and Aging Management of Concrete Structures,, Bratislava, Slovakia, , July 5-7, 1999.

[9] F. J. Presuel-Moreno, C. Castaneda, I. Santillan, A. Kazemi, and F. Tang, "Corrosion Prevention of Bridge Tendons Using Flexible Filler Materials," Florida Atlantic University, Center for Marine Materials, BDV27-977-10, November 1, 2018. [Online]. Available: https://rosap.ntl.bts.gov/view/dot/63238/dot_63238_DS1.pdf

[10] A. B. M. Abdullah, J. A. Rice, R. Bhatia, N. R. Brenkus, and H. R. Hamilton, "Unbonded Tendons as an Alternative for Bonded Tendons in Post-Tensioned Bridges:Constructability, Structural Performance, and Monitoring," *Structures Congress,* pp. 506-516, 2017, doi: https://ascelibrary.org/doi/10.1061/9780784480403.043.

[11] B. N.R., R. Bhatia, W. A. Potter, and H. R. Hamilton III, "Flexible filler mock-up injections of bridge post-tensioning tendons," *PCI Journal,* vol. 63, no. 3, pp. 65-76, May-June, 2018.

[12] *Standard Specification for Road and Bridge Construction, FY 2019-20*, Tallahassee, FL, USA, 2019. [Online]. Available: https://www.fdot.gov/specifications/standard-specification-library

[13] *Standard Specifications for Road and Bridge Construction, FY 2023-24*, Tallahassee, Florida, June, 2023. [Online]. Available: https://www.fdot.gov/specifications/standard-specification-library

[14] S. Arnold and J. Petrozzino-Roche, "PT System and Approval Process," in *FDOT Transportation Symposium, 2019*, 2019.

[15] B. J. Musser and P. K. Kilpatrick, "Molecular Characterization of Wax Isolated from a Variety of Crude Oils," *Energy & Fuels,* vol. 12, no. 4, pp. 715-725, 1998, doi: 10.1021/ef970206u.

[16] D. L. Dorset, "Crystallography of Real Waxes: Branched Chain Packing in Microcrystalline Petroleum Wax Studied by Electron Diffraction," *Energy & Fuels,* vol. 14, no. 3, pp. 685-691, 2000, doi: 10.1021/ef9902350.

[17] H. P. Roenningsen, B. Bjoerndal, A. B. Hansen, and W. B. Pedersen, "Wax precipitation from North Sea crude oils: 1. Crystallization and dissolution temperatures, and Newtonian and non-Newtonian flow properties," *Energy & Fuels,* vol. 5, no. 6, pp. 895-908, 2002, doi: 10.1021/ef00030a019.

[18] J. Taheri-Shakib, M. Rajabi-Kochi, E. Kazemzadeh, H. Naderi, and A. Shekarifard, "A comprehensive study of the impact of wax compositions on the wax appearance temperature (WAT) of some Iranian crude oils: An experimental investigation," *Journal of Petroleum Science and Engineering,* vol. 165, pp. 67-80, 2018, doi: 10.1016/j.petrol.2018.02.002.

[19] D. D. Robertson, A. J. Van Reenen, and H. Duveskog, "A comprehensive investigation into the structure-property relationship of wax and how it influences the properties of hot melt adhesives," *International Journal of Adhesion and Adhesives,* vol. 99, p. 102559, June 2020, doi: 10.1016/j.ijadhadh.2020.102559.

[20] M. Kurniawan, S. Subramanian, J. Norrman, and K. Paso, "Influence of Microcrystalline Wax on the Properties of Model Wax-Oil Gels," *Energy & Fuels,* vol. 32, no. 5, pp. 5857-5867, 2018, doi: 10.1021/acs.energyfuels.8b00774.

[21] J. P. Fuzier, H. R. Ganz, and P. Matt, "Durability of Post tensioning tendons," Lausanne, Switzerland, fib Buletin No.33, 2006.

[22] Post-Tensioning Institute, "Selection of Filler Material for Multistrand PT tendons," Post-Tensioning Institute, Farmington Hills, MI, USA, PTI Technical Note No.19, August, 2015.

[23] A. B. M. Abdullah, J. A. Rice, R. Bhatia, N. R. Brenkus, and H. R. Hamilton, "A thermal analysis of flexible filler injection for unbonded post-tensioning tendons," *Construction and Building Materials,* vol. 126, pp. 599-608, 2016, doi: https://doi.org/10.1016/j.conbuildmat.2016.09.083.

[24] N. R. Brenkus, A. B. M. Abdullah, R. Bhatia, D. Skelton, J. A. Rice, and H. R. Hamilton, "Replaceable Unbonded Tendons for PostTensioned Bridges," Florida Department of Transportation, Gainesville, Florida, BDV31-977-15, 2017.

[25] Agilent Technologies, "Basics of Measuring the Dielectric Properties of Materials," June 26, 2006.

[26] V. Komarov, S. Wang, and J. Tang, "Permittivity and measurement," *Encyclopedia of RF and Microwave Engineering,* pp. 3693-3711, 01/01 2005, doi: https://doi.org/10.1002/0471654507.eme308.

[27] W. Jackson, "The Mechanism of Dielectric Loss in Paraffin Wax Solutions at High Radio Frequencies," *Proceedings of the Royal Society of London. Series A. Mathematical and Physical Sciences,* vol. 150, no. 869, pp. 197-220, 1935, doi: https://doi.org/10.1098/rspa.1935.0096.

[28] R. W. Sillars, "The behaviour of polar molecules in solid paraffin wax," *Proceedings of the Royal Society of London. Series A., Mathematical and Physical Sciences,* vol. 169, no. 936, pp. 66-83, 1938, doi: 10.1098/rspa.1938.0195.

[29] D. R. Pelmore, "Dielectric loss due to polar molecules in solid paraffin," *Proceedings of the Royal Society of London. Series A, Mathematical and Physical Sciences,* vol. 172, no. 951, pp. 502-517, 1939, doi: 10.1098/rspa.1939.0195.

[30] T. D. Callinan and A. M. Parks, "The Dielectric Constants and Loss Factors of Some Natural Waxes," presented at the 1959 Conference on Electrical Insulation, 1959.

[31] T. D. Callinan and A. M. Parks, "The Electrical Properties of Some Natural Waxes," *Journal of The Electrochemical Society,* vol. 107, no. 10, 1960, doi: 10.1149/1.2427516.

[32] A. M. Hassan, R. M. A. Shahba, M. A. Youssif, A. M. Mazrouaa, and M. A. E. Youssif, "Preparation of some dielectric greases from different types of polymers," *Journal of Applied Polymer Science,* vol. 119, no. 2, pp. 1026-1033, 2010, doi: 10.1002/app.32385.

[33] A. M. Hassan, M. A. Youssif, A. M. Mazrouaa, R. M. Abou Shahba, and M. A. E. Youssif, "Evaluation of the dielectric properties of grease containing copolymers and ester," *Journal of Applied Polymer Science,* vol. 125, no. 2, pp. 1439-1447, 2012, doi: 10.1002/app.35619.

[34] L. Prava, "A Study on Physical Properties of Some Waxes," PhD Thesis, Jawaharlal Nehru Technological University, 2010.

[35] S. P. Chakyar *et al.*, "Measurement of Dielectric Constant of Waxes at Different Temperatures using Split Ring Resonator Structure," presented at the 2016 IEEE MTT-S International Microwave and RF Conference (IMaRC), 2016.

[36] H. Xu *et al.*, "Tunable dielectric properties of mesoporous carbon hollow microspheres via textural properties," *Nanotechnology,* vol. 29, no. 18, p. 184003, 2018, doi: 10.1088/1361-6528/aaaf25.

[37] B. Kuang *et al.*, "Chemical reduction dependent dielectric properties and dielectric loss mechanism of reduced graphene oxide," *Carbon,* vol. 127, pp. 209-217, 2018, doi: 10.1016/j.carbon.2017.10.092.

[38] C. C. Dey, A. Mallick, A. S. Mahapatra, M. Dalal, and P. K. Chakrabarti, "Electromagnetic-wave shielding promulgation of cluster like FZ@MWCNT composite incorporated in GO matrices by

polarization relaxation and potential degradation," *Materials Characterization,* vol. 172, p. 110884, 2021, doi: 10.1016/j.matchar.2021.110884.

[39] C. Wang, X. Han, P. Xu, X. Wang, X. Li, and H. Zhao, "Magnetic and dielectric properties of barium titanate-coated barium ferrite," *Journal of Alloys and Compounds,* vol. 476, no. 1-2, pp. 560-565, 2009, doi: 10.1016/j.jallcom.2008.09.092.

[40] J. Hongxia, L. Qiaoling, Y. Yun, G. Zhiwu, and Y. Xiaofeng, "Preparation and microwave adsorption properties of core–shell structured barium titanate/polyaniline composite," *Journal of Magnetism and Magnetic Materials,* vol. 332, pp. 10-14, 2013, doi: 10.1016/j.jmmm.2012.11.010.

[41] H. Freij, D. Dukeman, C. L. Alexander, and A. A. Sagüés, "Practical Cross-Section Imaging of External Tendons to Reveal Grout Deficiencies Relative to Strand Pattern," *Journal of Bridge Engineering,* vol. 25, no. 11, 2020, doi: 10.1061/(asce)be.1943-5592.0001636.

[42] M. E. Orazem and B. Tribollet, "Electrochemical impedance spectroscopy," *New Jersey,* vol. 1, no. 906, pp. 383-389, 2008.

[43] R. C. Weast, *Handbook of chemistry and physics 53rd edition*. Cleveland, OH, USA: Chemical Rubber Pub., 1972.

[44] L. Solymar, *Lectures on electromagnetic theory: A short course for engineers*. Oxford, U.K.: Oxford University Press, 1976.

[45] C. L. Alexander and M. E. Orazem, "Indirect impedance for corrosion detection of external post-tensioned tendons: 2. multiple steel strands," *Corrosion Science,* vol. 164, p. 108330, 2020.

[46] C. L. Alexander and M. E. Orazem, "Indirect electrochemical impedance spectroscopy for corrosion detection in external post-tensioned tendons: 1. Proof of concept," *Corrosion Science,* vol. 164, p. 108331, 2020, doi: https://doi.org/10.1016/j.corsci.2019.108330.

[47] A. Dizon and M. E. Orazem, "On the impedance response of interdigitated electrodes," *Electrochimica Acta,* vol. 327, p. 135000, 2019, doi: https://doi.org/10.1016/j.electacta.2019.135000.

[48] J. R. Reitz, F. J. Milford, R. W. Christy, S. Kunde, and S. Hermiston, *Foundations of electromagnetic theory*. Reading, MA, USA: Addison-Wesley Pub. Co, 1967.

[49] A. A. Sagüés, "Systems and methods for determining strand position in a post-tensioned tendon," Patent US 9,651,357 B1, May 16, 2017, 2017.

[50] G. E. H. Reuter and E. H. Sondheimer, "The theory of the anomalous skin effect in metals," *Proceedings of the Royal Society of London. Series A. Mathematical and Physical Sciences,* vol. 195, no. 1042, pp. 336-364, 1948, doi: 10.1098/rspa.1948.0123.

Appendix A: Cross-section representations of MTB, MTC, and MTD for experimental verification of TIU Capability in void detection:

The images shown in Figure A 1-3 are cross-sectional representations of mock tendons B, C, and D, respectively. The results help confirm the level of capability in detecting both water and air void fill deficiencies.

TIU in position of void	TIU not in position of void

(a)

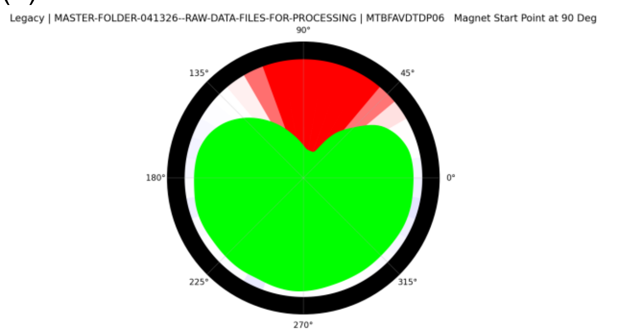

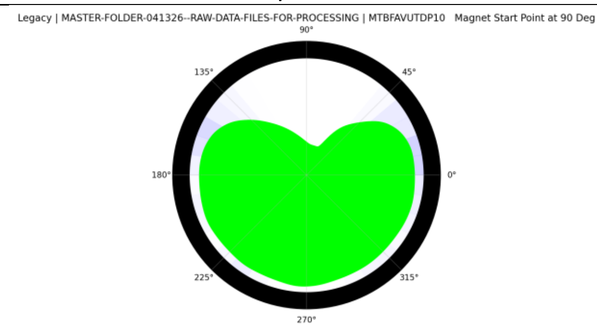

(b)

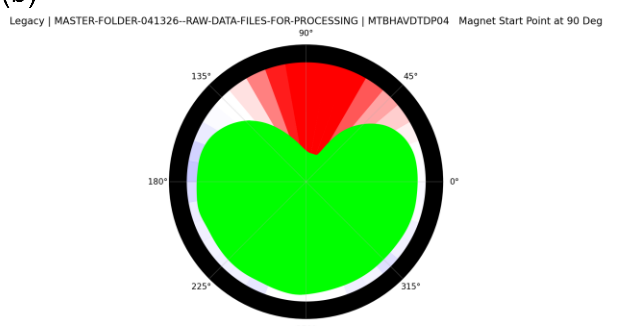

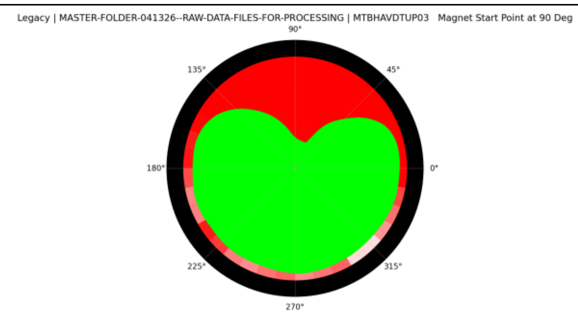

(c)

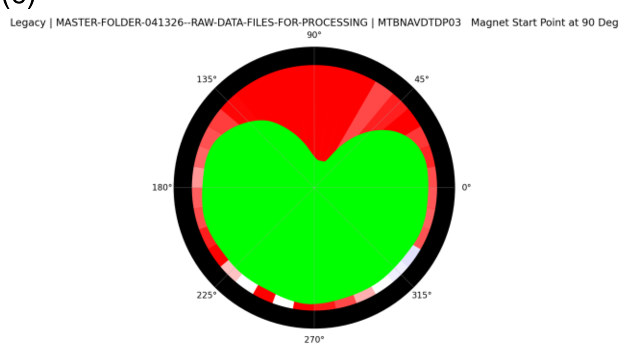

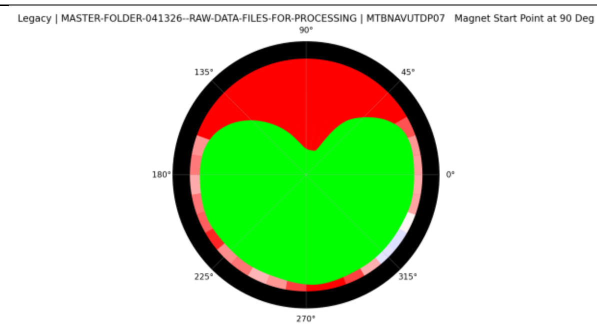

Figure A-1. Cross-section images of MTB with different air void cases: (a) Full Oil, Air Void; (b) Half Oil, Air Void; (C) No Oil, Air Void; (d) Full Oil, Water Void; (e) Half Oil, Water Void; No Oil, Water Void

<table>
<tr><th>TIU in position of void</th><th>TIU not in position of void</th></tr>
<tr><td>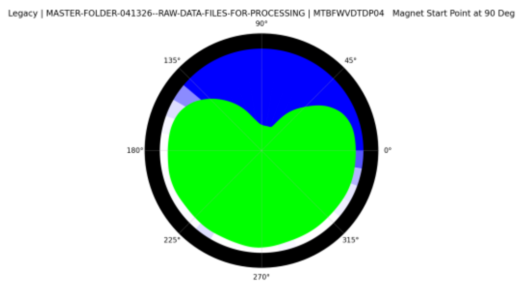
(d)</td><td>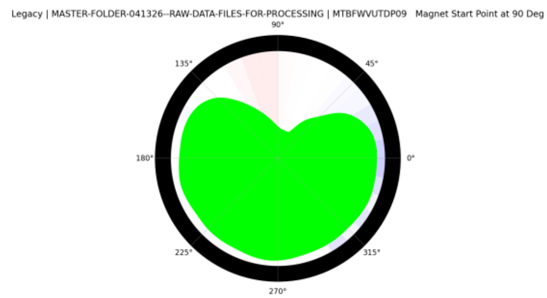</td></tr>
<tr><td>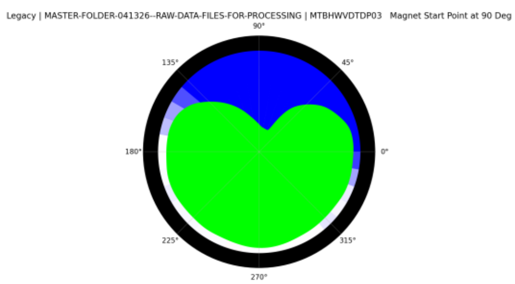
(e)</td><td>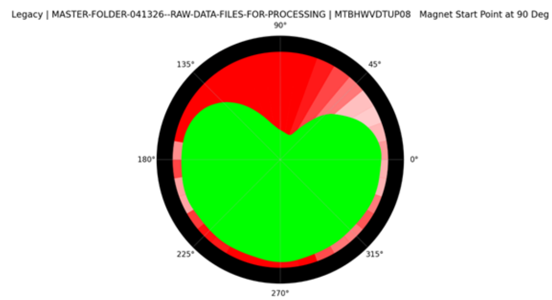</td></tr>
<tr><td>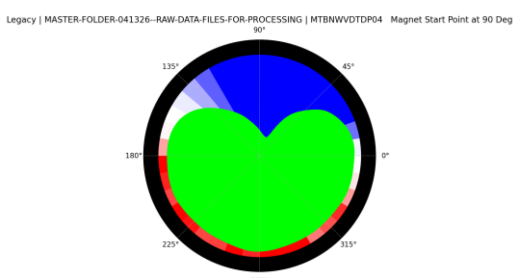
(f)</td><td>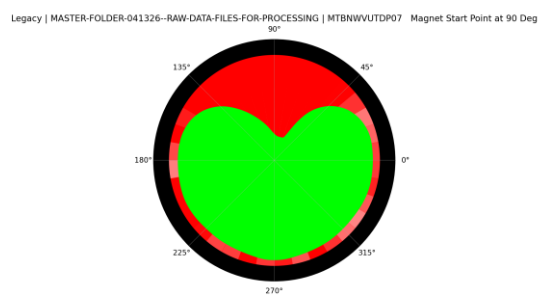</td></tr>
</table>

Figure A-1. (Continued) Cross-section images of MTB with different air void cases: (a) Full Oil, Air Void; (b) Half Oil, Air Void; (C) No Oil, Air Void; (d) Full Oil, Water Void; (e) Half Oil, Water Void; No Oil, Water Void

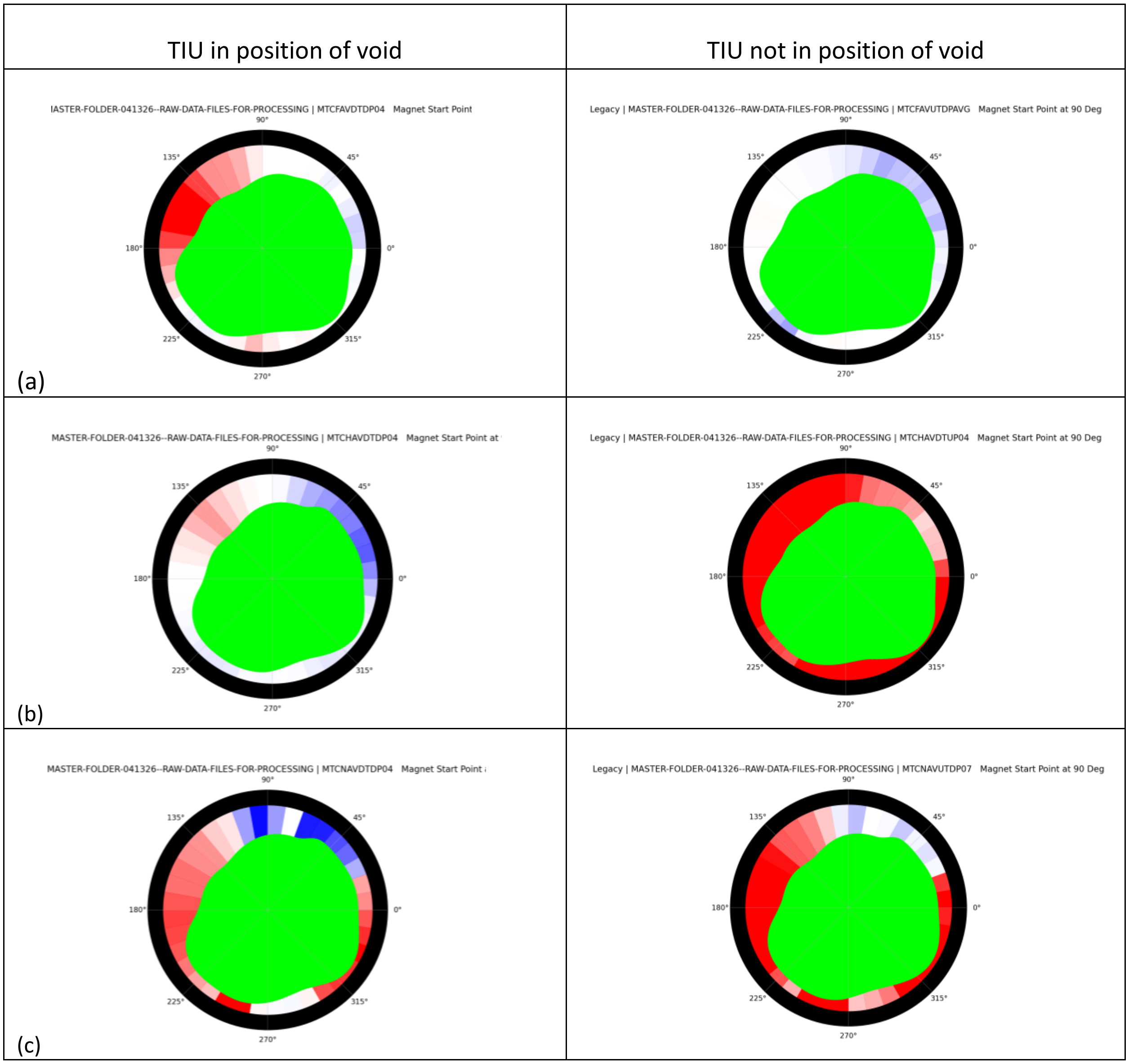

Figure A-2. Cross-section images of MTC with different air void cases: (a) Full Oil, Air Void; (b) Half Oil, Air Void; (C) No Oil, Air Void; (d) Full Oil, Water Void; (e) Half Oil, Water Void; No Oil, Water Void

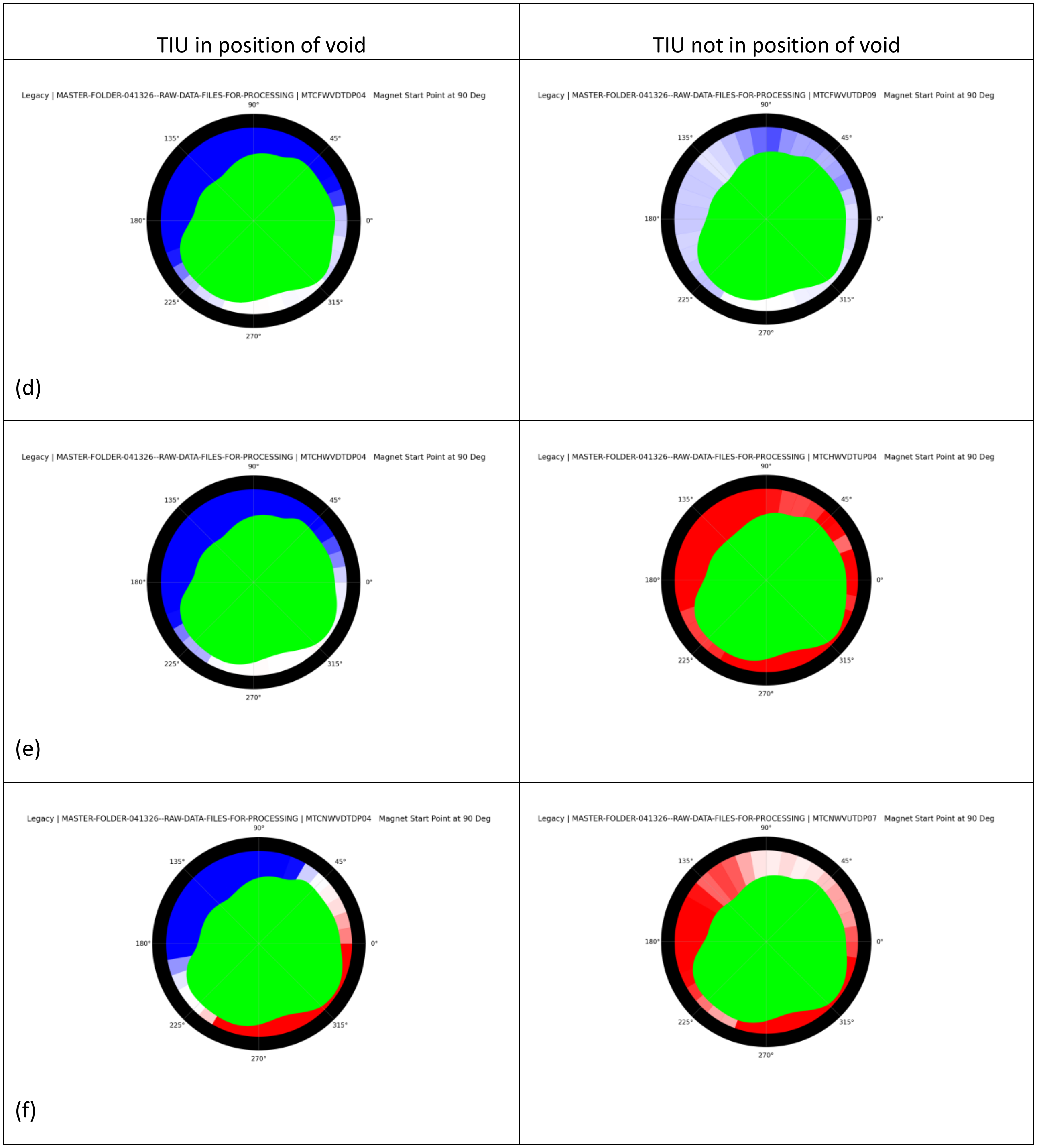

Figure A-2. (Continued) Cross-section images of MTC with different air void cases: (a) Full Oil, Air Void; (b) Half Oil, Air Void; (C) No Oil, Air Void; (d) Full Oil, Water Void; (e) Half Oil, Water Void; No Oil, Water Void

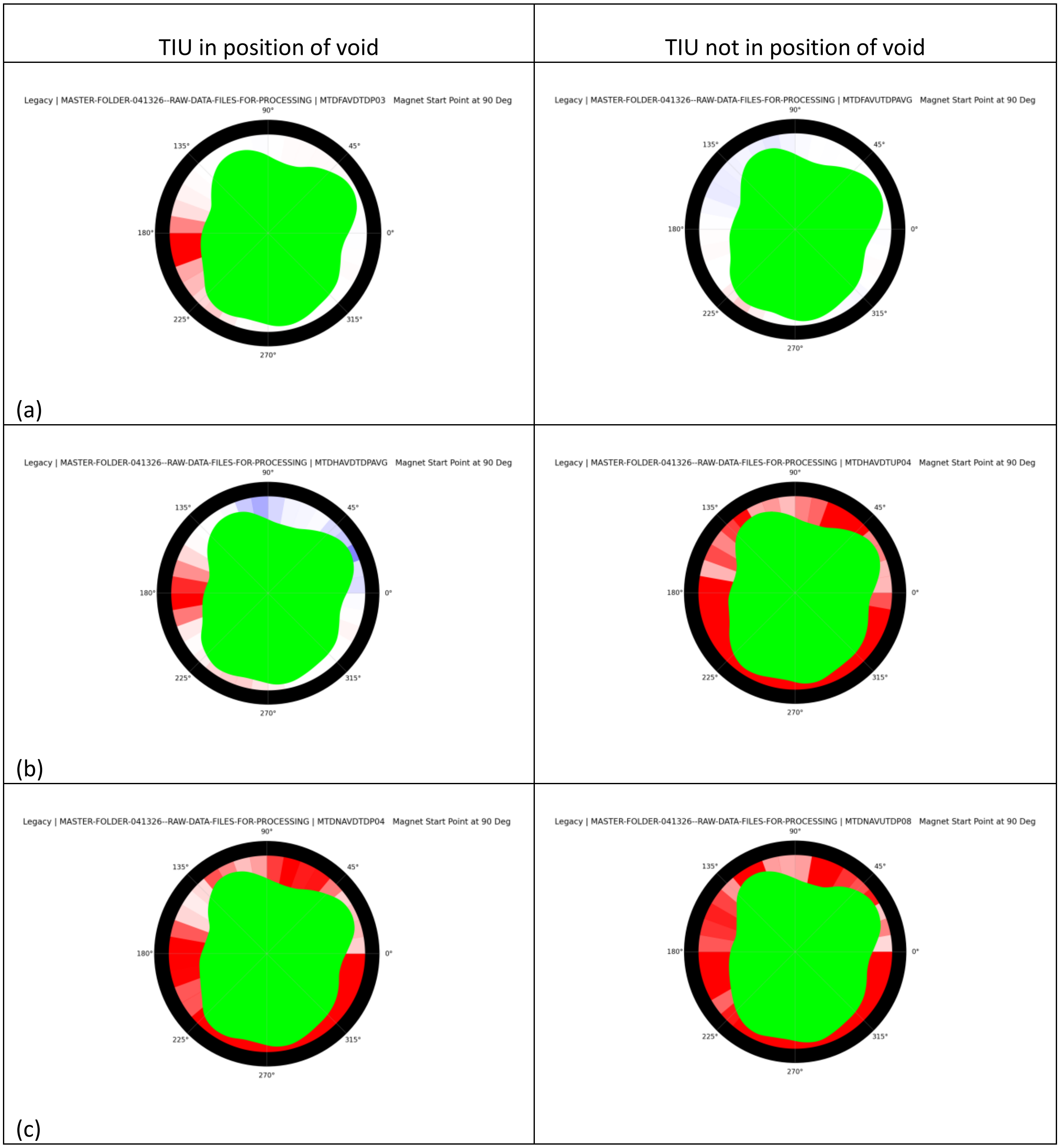

Figure A-3. Cross-section images of MTD with different air void cases: (a) Full Oil, Air Void; (b) Half Oil, Air Void; (C) No Oil, Air Void; (d) Full Oil, Water Void; (e) Half Oil, Water Void; No Oil, Water Void

TIU in position of void	TIU not in position of void

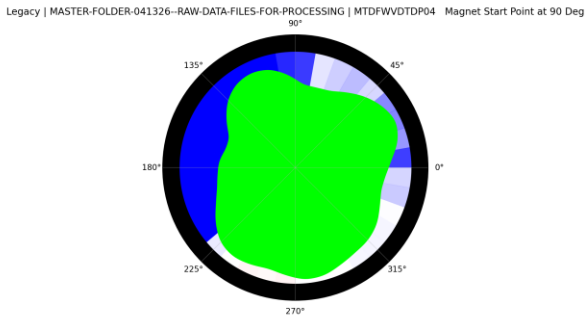

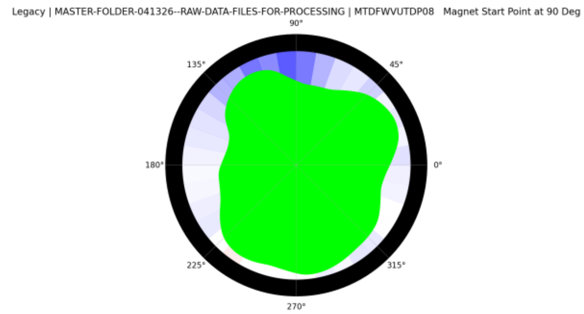

(d)

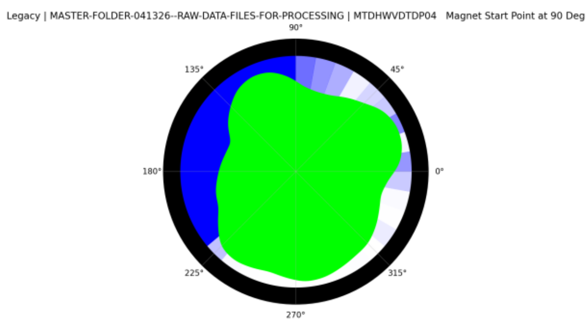

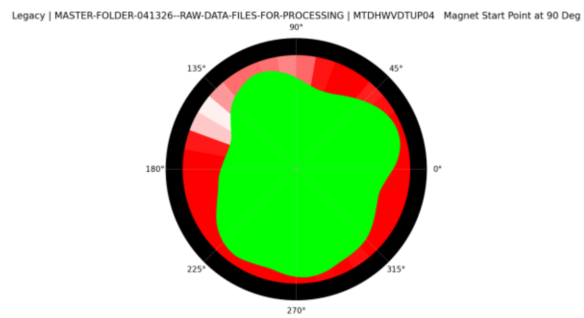

(e)

(f)

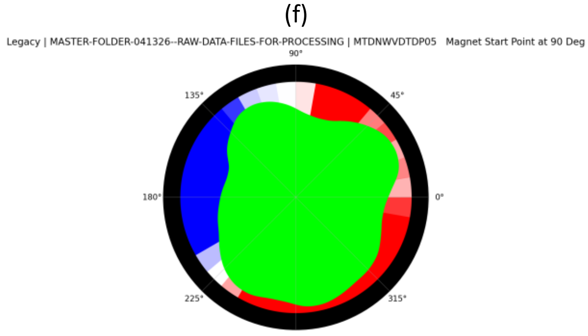

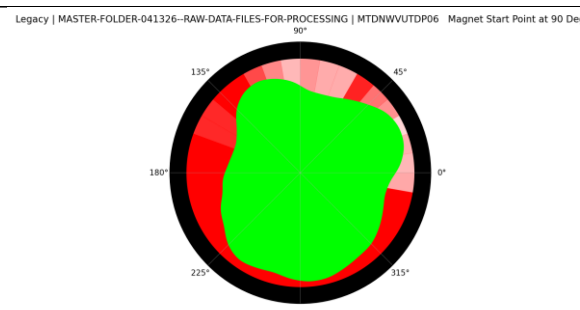

Figure A-3. (Continued) Cross-section images of MTD with different air void cases: (a) Full Oil, Air Void; (b) Half Oil, Air Void; (C) No Oil, Air Void; (d) Full Oil, Water Void; (e) Half Oil, Water Void; No Oil, Water Void